CHANNEL MODELLING AND CHARACTERIZATION FOR VISIBLE LIGHT COMMUNICATIONS

A Thesis

by

Elham Sarbazi

Submitted to the
Graduate School of Sciences and Engineering
In Partial Fulfillment of the Requirements for
the Degree of

Master of Science

in the
Department of Electrical and Electronics Engineering

Özyeğin University
August 2014

CHANNEL MODELLING AND CHARACTERIZATION FOR VISIBLE LIGHT COMMUNICATIONS

Approved by:

Professor Murat Uysal, Advisor
Department of Electrical and Electronics Engineering
Özyeğin University

Professor Cenk Demiroğlu
Department of Electrical and Electronics Engineering
Özyeğin University

Dr. Sultan Aldirmaz
Department of Electronics and Communication Engineering
Kocaeli University

Date Approved: 1 August 2014

To my grand parents who wished to see me complete my study,

and my family for all the love and support.

List of My Publications

[1] E. Sarbazi, M. Uysal, M. Abdallah, and K. Qaraqe, "Indoor Channel Modelling and Characterization for Visible Light Communications," in *16th International Conference on Transparent Optical Networks (ICTON)*, Jul. 2014.

[2] E. Sarbazi, M. Uysal, M. Abdallah, and K. Qaraqe, "Ray Tracing Based Channel Modeling for Visible Light Communications," in *IEEE 22nd Signal Processing and Communications Applications Conference (SIU)*, pp. 702–705, Apr. 2014.

[3] E. Sarbazi and M. Uysal, "PHY Layer Performance Evaluation of the IEEE 802.15.7 Visible Light Communication Standard," in *IEEE 2nd International Workshop on Optical Wireless Communications (IWOW)*, pp. 35–39, Oct. 2013.

ABSTRACT

Visible light communications (VLC) involve the dual use of illumination infrastructure (i.e., LEDs) for wireless communication purposes. Despite the growing academic and industrial interest, there is a lack of realistic VLC channel models. In the current literature, the models developed for infrared channels in the past are used for the performance evaluation of VLC systems without a solid justication. However, it is known that visible light and infrared bands exhibit different characteristics and this necessitates the development of realistic VLC channel models. In an effort to address this research gap, we present a comprehensive framework for VLC channel modeling and characterization in this thesis.

Our channel modeling is based on the ray tracing approach. The simulation environment is created in the Zemax software and enables us to specify the geometry of the environment, the objects inside, the reflection characteristics of the surface materials as well as the specifications of the light sources and receivers. The received optical power and the delay of direct/indirect rays are computed for the specified indoor environment and the corresponding channel impulse response (CIR) is obtained through proper normalizations. Following this methodology, we present CIRs for a number of indoor environments and quantify channel gain and time dispersion parameters for each environment. We further develop statistical models for characterization of indoor VLC channels through examination of a large set of CIRs collected from thousands of test points in an empty room. Finally, we use the obtained CIRs in the error rate performance evaluation of various operation modes in the IEEE 802.15.7 VLC standard.

ÖZETÇE

Görülebilir ışık haberleşmesi (GIH) aydınlatma altyapılarının kablosuz haberleşme amacıyla çift amaçlı kullanılmasını kapsamaktadır. Bu alana hem akademik hem de endüstriyel ilginin artmış olmasına rağmen literatürde gerçekçi GIH kanal modelleri bulunmamaktadır. Mevcut litetatürde geçmişte kızılötesi kanallar için geliştirilen modeller yeterli gerekçelendirmeler yapılmadan GIH sistemlerinin değerlendirilmesi için de kullanılmaktadır. Ancak görülebilir ışık ve kızılötesi bantların farklı karakteristik özelliklerinin olduğu bilinmektedir. Bu durum gerçekçi GIH kanal modellemesi yapılmasını gerektirmektedir. Literatürdeki bu açığı gidermek adına bu tez, GIH kanal modellemesi ve karakterizasyonu için kapsamlı bir çerçeve sunmaktadır.

Tezde sunulan kanal modellemesi ışın izi takip metoduna dayanmaktadır. Simülasyon ortamı Zemax adlı yazılımda oluşturulup ortam geometrisi, içindeki objeler, yüzey malzemeleri yansıma karakteristiği ve ışık kaynakları ile alıcılarının özellikleri girdi olarak verilmektedir. Vericide toplanan optik güç ve dolaylı/dolaysız ışın gecikmeleri özellikleri verilen kapalı alanlar için hesaplanmakta ve bunlara ilişkin kanal dürtü cevabı (KDC) uygun normalleştirmeler ile elde edilmektedir. Bu yöntem izlenerek bu tezde farklı kapalı alanlar için KDCler sunulmakta ve her ortam için kanal kazançları ve zaman dağılım parametreleri hesaplanmaktadır. Ayrıca, boş bir odada binlerce test noktasından toplanan geniş bir KDC kümesi kullanılarak GIH kanalları için istatiksel modeller de geliştirilmiştir. Son olarak, elde edilen KDCler kullanılarak IEEE 802.15.7 GIH standardındaki farklı çalışma modları için hata başarım değerlendirmesi yapılmıştır.

ACKNOWLEDGEMENTS

It is my pleasure to acknowledge all the people who have contributed to this research and my overall experience at OzU.

First and foremost, I would like to take this opportunity to offer my sincere gratitude to my research advisor, Prof. Murat Uysal, for his persistent support, continuous guidance, and invaluable advice during this program. I attribute the level of my Master's degree to his encouragement and effort.

Special thanks go to all my friends especially my lab mates, who provided a perfect environment for my studies and research.

Last but not least, I would like to express my deepest gratitude to my parents. Thanks for their generous and endless love to me. They are always with me whenever I go through tough situations and provide encouragement and support. Without their support, this research work would not happen. My most heartfull appreciation goes to them by dedicating this thesis to them.

Thanks are also due to TUBITAK Research Grant 111E143 for providing financial support during the course of this research.

TABLE OF CONTENTS

LIST OF TABLES

LIST OF FIGURES

CHAPTER I

INTRODUCTION

New generation of light emitting diodes (LED) has more advantages than existing fluorescent and incandescent lighting such as long life expectancy, high tolerance to humidity, low-power consumption, and minimal heat generation. It is expected that LEDs will be omni present in the near future with government plans worldwide to phase out conventional lighting in favour of LEDs. Since the human eye perceives only the average intensity when light changes fast enough, it is possible to transmit data using LEDs without a noticeable effect on the lighting output and the human eyes. Simultaneous use of LEDs for both lighting and communications purposes is a sustainable and energy-efficient approach that has the potential to revolutionize how we use light [1–5]. This makes possible the so-called visible light communication (VLC).

In this chapter, we first provide a brief overview of the emerging VLC technology along with its advantages and possible challenges. We will introduce some of its potential applications and describe the basic properties and components of a VLC system. Finally, the main contributions and the organization of this thesis will be stated.

1.1 Visible Light Communications

The expected wide-scale availability of LEDs in the near future opens the door for VLC technology. It is predicted that LEDs will gradually replace both incandescent and fluorescent lights and be the ultimate light source in the near future [6]. Compared with traditional light sources, LEDs have the advantages of longer life expectancy, high lighting efficacy, no out-of-visible band optical spectrum (unlike incandescent lamps with huge infrared spectrum light and fluorescent lamps with additional ultraviolet spectrum), easy maintenance, and environmental friendliness [7].

White LEDs can be pulsed at hundreds of megahertz, making it possible to transmit data at high speeds without noticeable effect on lighting output and human eye. Besides the energy efficiency as a result of dual use, VLC offers several other inherent advantages over radio frequency (RF) based counterparts, such as immunity to electromagnetic interference, operation on unlicensed bands, additional physical security, and high degree of spatial confinement allowing a high reuse factor.

VLC also provides some advantages over the infrared (IR) communications. It is required that a certain limit for the transmission power of the infrared light sources is set in order to guarantee human skin safety for people residing in the infrared communication area. In comparison, no transmission power limit is set for the visible light LED sources because no potential hazard is introduced by the visible light to the human body. Meanwhile, because the VLC system is usually piggybacked on an illumination or signaling system, a minimum transmitted optical power is usually required to maintain a certain illumination level. This could result in a high SNR at the receiver, an advantage that can be taken to boost the communication data rate and improve the communication system performance [7]. A comparison of these three technologies is provided in Table 1 [8,9].

Similar to conventional IR communications, the indoor VLC link configurations can be classified into four basic types, according to the existence of obstacles in light path and the directionality of the transmitter to the receiver and the field of view of the receiver, as shown in Fig. 1 [10,11].

As depicted in Fig. 1, an optical wireless link can be either line-of-sight (LOS) or non-line-of-sight (NLOS). In a LOS link, transmitter is within the receiver field of view (FOV). The second type, which is NLOS link, relies generally upon the reflection of the light from the ceiling or some other diffusely reflecting surfaces. Compared to

Table 1: Comparison of VLC, IR and RF communication technologies [9]

Property	**VLC**	**IR**	**RF**
Bandwidth	Unlimited 400-700 nm	Unlimited 800-1600 nm	Regulated and limited
Electromagnetic Interference	No	No	Yes
Line of Sight	Yes	Yes	No
Distance Range	Short	Short to long (outdoor)	Short to long (outdoor)
Services	Illumination and Communications	Communications	Communications
Noise Resources	Sun light and other ambient lights	Sun light and other ambient lights	All electrical/electronic appliances
Power Consumption	Relatively low	Relatively low	Medium
Mobility	Limited	Limited	Good
Coverage	Narrow and wide	Narrow and wide	Mostly wide
Security	Good	Good	Poor

the LOS link, the path loss of the NLOS link is generally much larger, while link robustness and ease of use increase, allowing the link to operate even when obstacles, such as people or objects, stand between the transmitter and receiver.

The directed link design adopts narrow beam angle transmitters and small FOV receivers, maximizing the power efficiency by minimizing the path loss and reception of ambient light noise. On the other hand, the non-directed link design adopts wide beam angle transmitters and large FOV receivers, alleviating a need for accurate pointing as in the directed link, while at the expense of large path loss.

In a VLC system, the link is basically non-directed (diffusive) LOS due to the nature of illumination system in an indoor environment. Hence, from now on, we concentrate on indoor applications of VLC and non-directed LOS links.

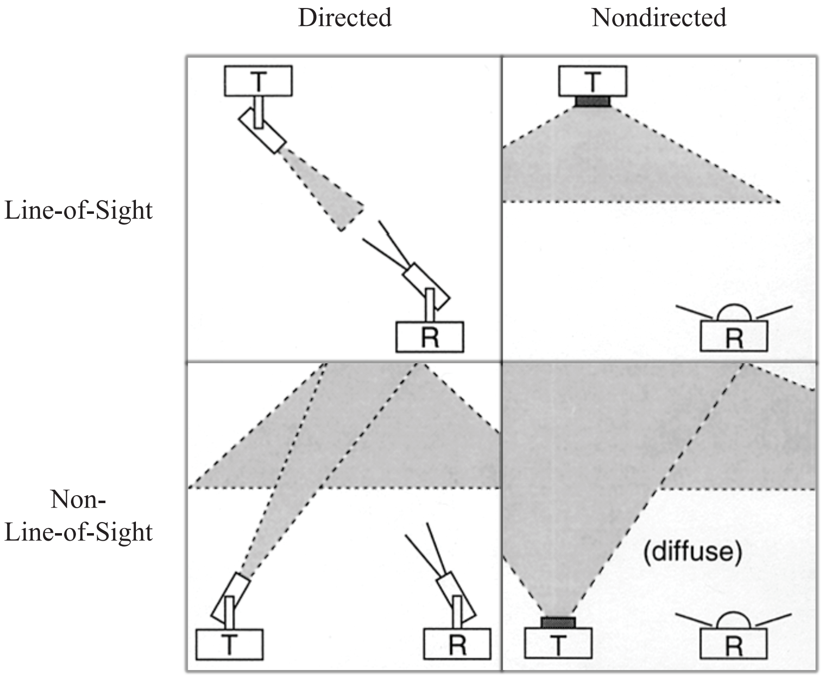

Figure 1: VLC link configurations

1.2 VLC Applications

It is envisioned that VLC systems and products will be an essential part of technology portfolio of leading telecommunication companies in near future. VLC can serve as a major enabling technology for a wide range of applications and services including, but not limited to,

- Wireless access in RF-restricted or prohibited areas such as hospitals, airplanes and hazardous environments (power plants, mines),
- Indoor navigation, e.g., each LED light is assigned a unique identity that can provide location information,
- Indoor broadband wireless access through the combination of VLC and power-line communications/fiber-to-the-home as an alternative or complementary to existing radio-frequency WLANs,
- Contents-sharing or data transferring between two handheld or portable devices, e.g., file, photo, video sharing between two cell phones,

- File transfers between a handheld/portable device and a fixed device like TV, printer, projector, computer etc.,
- Communication and networking among the computing devices and peripherals,
- E-commerce, e.g., payment through a mobile device,
- E-content vending machine, e.g., downloading e-book/music/video from vending machines to be located in public places,
- Broadcasting from outdoor signs and displays,
- Information or guidance service, e.g., audio guide at museums, art galleries or exhibits,
- Intelligent transportation systems including vehicle-to-vehicle communication (via the use of headlights/taillights) and vehicle-to-infrastructure (e.g., traffic lights) communication.

1.3 Basic VLC System Properties

VLC uses intensity modulation and direct detection (IM/DD) for data transmission. Figure 2 displays a block diagram of an intensity modulated direct detection system [12]. The instantaneous optical intensity, $x(t)$, is modulated proportional to the input electrical current $m(t)$. This method of modulation is termed as intensity modulation. After data modulation, the intensity signal is transmitted through the channel. At the receiver, a photodiode is used to detect the received intensity. This method of detection is termed as direct detection.

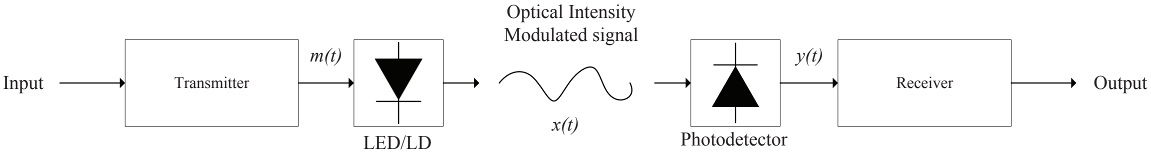

Figure 2: Block diagram of an IM/DD channel

1.3.1 VLC Transmitters

LEDs are the most likely optical sources for a dual-use lighting and communication application, and thus form the central component of the VLC system transmitter. They are preferred over other lighting sources, such as incandescent and fluorescent sources, since they can respond to faster modulations and support higher data-rates. LEDs are preferred over laser diodes (LDs) due to safety regulations, as LDs in the visible range can be harmful to the eyes [8].

An LED is a semiconductor light source. Two important lighting factors of LEDs are color rendering index and luminous efficacy. The color rendering index is a measure of the ability of the LED to produce color in comparison with an ideal light source. The luminous efficacy on the other hand, is the measure of the efficacy with which the source produces visible light from electricity. It is equal to the ratio of luminous flux, to the total electric power consumed by the source. Therefore it has the units of lumen per watt (lm/W) [13]. The LEDs produce white light suitable for illumination and data modulation. There are two popular methods to produce white light.

Phosphor-Based LEDs

This method involves coating a blue LED with a yellow emitting phosphor as shown in Fig. 3. The resulting LEDs are termed as phosphor-based white LEDs. Phosphor-based LEDs have a lower luminous efficacy compared to RGB LEDs due to phosphor-related degradation issues. However, the majority of white LEDs that are currently in use on the market are manufactured using this technology. Apart from the advantage of requiring only a single color source, these types of LEDs are easier to design and are less expensive than complex RGB LEDs. Furthermore, the available modulation bandwidth of such LEDs can be enhanced by at least an order of magnitude using blue filtering. Due to the long decaying time of the phosphor, the modulation bandwidth of the white emission is limited to ~ 2 MHz. However, the blue component has a

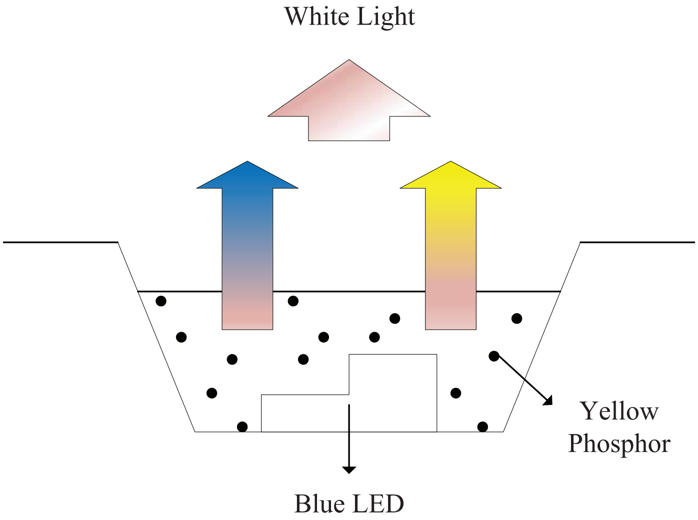

Figure 3: The structure of phosphor-based white LEDs

larger modulation bandwidth ∼ 20 MHz. As a result, to achieve a higher modulation bandwidth and therefore higher data rates, a common method is to only detect the blue part of the spectrum at the receiver termed as blue filtering [13].

RGB LEDs

A simple way to form white light is to mix red, green and blue (RGB) colors with appropriate portions as shown in Fig. 4 [6]. The LEDs produced in this way are often referred to as RGB LEDs. RGB LEDs have the flexibility of mixing different colors and possess higher luminous efficacy compared to phosphor-based LEDs discussed in previous section. However, they are seldom used in practice to produce white light. Other than requiring different color optical sources, RGB LEDs suffer from instability in the produced color. The RGB LED's performance degrades with rising temperature hence leads to a considerable change in the produced color [13].

1.3.2 VLC Receivers

Typical receivers used in a VLC system are photodiodes. Photodiodes are solid-state devices that are used to perform the optical to electrical conversion. They produce an output electrical current, $y(t)$, proportional to the received intensity signal. The

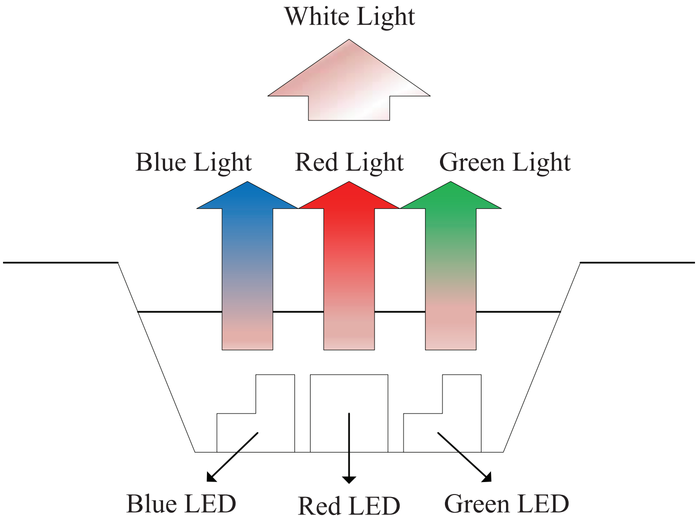

Figure 4: The structure of RGB white LEDs

received current is then processed to extract the transmitted information. The key parameter in photodiodes is the responsivity defined as,

$$r = \frac{I_p}{P_p} \tag{1}$$

where I_p is the average photocurrent generated and P_p is the incident optical power. The photodiode responsivity depends on the physical structure of the photodiode and has the units of ampere per watt (A/W). Two common photodiodes that are currently used in practice are p-i-n photodiodes and avalanche photodiodes. The first type has lower cost but lower modulation bandwidth [12]. The received power of the photodiode, P_p, is proportional to its effective light collection area. Thus, the photodiode effective area must be large enough to collect the transmitted signal. In general, photodiodes must be selected such that the cost, performance and safety requirements are satisfied.

1.4 Thesis Organization

The remainder of this thesis is organized as follows.

In Chapter 2, we first provide a brief review of the indoor IR channel models available in the literature along with the reasons which prove the need for developing a specific channel model for VLC. Then we propose two methods for obtaining the impulse response of a VLC channel and compare them in case of accuracy and computational time. Finally we provide impulse response results for a number of indoor environments.

In Chapter 3, we develop statistical models for characterization of indoor VLC channels through examination of a large set of channel impulse responses. The model development is made possible by the method introduced in chapter 2. This method allows fast and accurate computation of thousands of impulse responses which are not limited to only two or three reflection orders. We analyze the collected channel gains and delay spreads to determine general trends and find statistical distributions to fit them.

In Chapter 4, we first provide a detailed description of physical layers of IEEE 802.15.7 standard. Then we present signal and channel models and implement the IEEE 802.15.7 PHY layers I, II and III in MATLAB and provide Monte Carlo simulation results over a typical indoor VLC channel.

Finally, Chapter 5 provides our conclusions and identifies potential points for the future research.

CHAPTER II

VLC CHANNEL MODELLING

As the analysis of channel characteristics is essential for all the telecommunication systems, much work has been done on channel characteristics for indoor infrared (IR) communication links [14–21]. Visible Light Communication technology based on white LEDs has attracted so much attention from the research community in the recent years [22–26]. Despite the growing literature on VLC, there is a lack of proper channel models. In the current literature, the channel models developed for IR in the past [10, 27] are used for the performance evaluation of VLC systems without a solid justification. However, it is known that visible light and IR bands exhibit different characteristics [22]. Therefore, characterization of indoor VLC channels is of vital importance.

In this chapter, we first provide a brief review of the indoor IR channel models available in the literature along with the reasons which prove the need for developing a specific channel model for VLC. Then we propose two methods for obtaining the impulse response of a VLC channel and compare them in case of accuracy and computational time. Finally we provide impulse response results for a number of environments.

2.1 Review of Indoor IR channel Models

Gfeller and Bapst [14], presented the very first method for determining the power distribution throughout a room for a given geometry in an IR communication system. They studied various channel parameters, such as the reflection properties of several materials, indoor channel response, overall system bandwidth, and ambient noise interference. They were the first to suggest that the reflections from surfaces can be modeled as Lambertian. In their paper, a method for calculating the power for a given geometry of the channel was presented, although no specific algorithm was described. A study on link properties and infrared receivers were also presented.

After nearly 15 years, Barry *et al.* [15], in their paper discretized the room into small cells. Calculations were done to find the impulse response of the channel for as many multiple reflections as required. This method is by far the most popular and is termed as the “recursive model”. In order to find the response due to the kth reflection, one need to know information about the $(k-1)$th reflection and also the LOS response. This method is very attractive, but has the disadvantage of having very long simulation times and very demanding requirements on the processing power. This technique has been widely used in academia and industry, and is the standard model for calculating impulse response of the indoor channels.

In 1997 [19], a different approach was taken by Carruthers and Kahn who developed the ceiling bounce model, based on the claim that realistic multipath infrared channels can be characterized by just two parameters; the optical path loss and the root mean square (RMS) delay spread. This model does not account for the presence of obstructions and multiple reflections and is not expected to be accurate. However, this method presented a way to characterize the infrared channel in terms of the multipath power penalty and delay spread. In other word, it can be used to analyze the effects of multipath dispersion and also the power distribution profile in indoor IR systems.

In the same year, Lopez-Hernandez *et al.* proposed a method called the “DUSTIN algorithm” for faster computation of impulse response on indoor IR channels. Here the calculation is done in three stages: (i) initialization, (ii) wall processing, and (iii) the calculation of photodiode response. This method has the advantage of simulating any number of reflections [28].

Perez-Jimenez suggested a statistical model for calculating impulse response of the channel based on several experiments. They came up with a closed-form expression for the RMS delay spread. Hence this is a fast approach for modeling the indoor IR channel. However, this method is not preferred by most of the researchers as the simulation results are not very accurate for all trans-receiver configurations [16].

Lopez-Hernandez *et al.* [17] also developed a computationally efficient algorithm based on Monte Carlo analysis to arrive at the impulse response of the indoor channel. In a later work [18], they used the Phong's model for reflecting surfaces in the Monte Carlo simulations, which they called as the “Modified Monte Carlo simulation” [29].

Carruthers *et al.* [30] developed an iterative site based method for the estimation of impulse response of the IR channels. This method can include any number of reflections and can account for all types of obstructions and shadowing effects. This is computationally more effective than the recursive method used by Barry *et al.* [15].

In 2011, Barry extended the use of his 90's infrared channel model to indoor VLC systems [22], this model is still the only channel model for VLC so far. To date, the efficient and specialized characterization of VLC channels, including sophisticated reflections, has not yet been studied. For convenience, researchers have used some of the mentioned IR channel models as the base for characterizing VLC systems.

Despite the similarity between channels of these two communication systems, differences still exist for the infrared and visible spectrum. This mainly comes from the different operating wavelength ranges and wavelength dependent devices (visible LED, silicon photodetector, materials, etc), and the fact that the VLC has the dual nature of communication and illumination. Moreover, in practice, most of the IR models are time-consuming, crude, and have some constraints in impulse response analysis, and are unable to accurately depict the illuminance function analysis of VLC systems. All these necessitate the development of VLC channel models.

In order to evaluate the impulse response for indoor VLC channels, we first extend the basic idea of Barry's algorithm [15] and combine it with the Lopez-Hernandez's

Monte Carlo ray-tracing algorithm [17], and obtain a propagation model for the VLC channel which allows us to consider

- Large number of reflections
- Any arbitrary environment regardless of its geometric shape and size
- Furnished environments with any number or any shape of objects inside
- Any type of transmitter or receiver with different gain functions
- Multiple transmitters and/or receivers
- The wideband nature and power distribution of the visible light source and wavelength-dependent nature of the reflectors.

This method provides significantly increased accuracy in evaluation of VLC channel, but still requires very high simulation times and/or the deployment of super computers. Thereupon, to eliminate the time-consuming recursive calculations of this method, we use a commercial optical software named Zemax® [31] for channel characterization. In the next two sections we introduce the mentioned methods and compare them in case of accuracy and computational time.

2.2 Modified Ray Tracing Approach based on Barry's Model

As in IR systems, VLC uses intensity modulation and direct detection (IM/DD). In general, optical wireless channels are modeled by a transmitter and receiver placed inside an environment with reflective surfaces, as depicted in Fig. 5. The transmitter or source S is a laser diode (LD) or a light-emitting diode (LED) transmitting a signal $X(t)$ using intensity modulation (IM). There may be a collection of receivers, each consisting of a photodiode which uses direct detection (DD). Indoor VLC systems normally use multiple LED lighting fixtures, because there are more than two lightings in homes and offices. Moreover, LED lamps consist of clusters of white LED chips. This is one of the differences compared with the IR transmitters [22].

The source S which emits a unit impulse of optical intensity at time zero, is

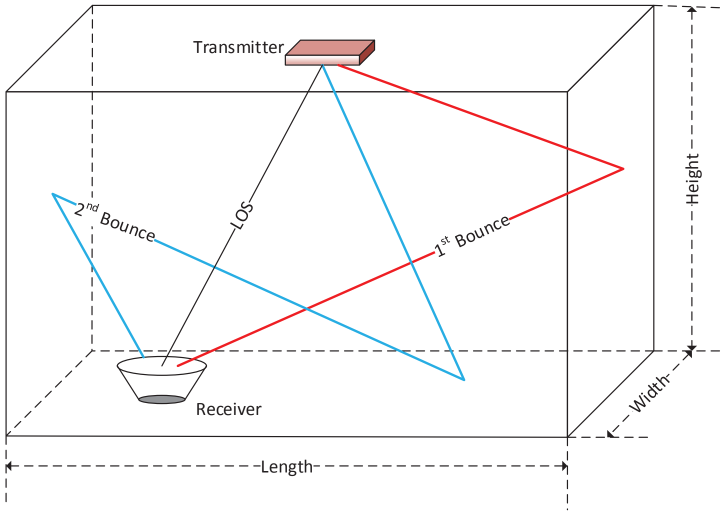

Figure 5: Geometry of the environment with transmitter and receiver

denoted by

$$S = \{\boldsymbol{r}_S, \boldsymbol{n}_S, R_S(n, \phi, \lambda)\} \tag{2}$$

where $\boldsymbol{r}_S$, $\boldsymbol{n}_S$ and $R_S(n, \phi, \lambda)$ are its position vector, orientation vector and the radiant intensity pattern, respectively. In general, source is modeled using a generalized Lambertian pattern for each wavelength. We assume that the radiant intensity pattern has axial symmetry about the normal axis, for simplicity. The radiation pattern for general Lambertian source, having uniaxial pattern (independent of θ) is given by [14]

$$R_S(n, \phi, \lambda) = \frac{n+1}{2\pi} P_S(\lambda) \cos^n(\phi), \quad \text{for } \phi \in \left[-\frac{\pi}{2}, \frac{\pi}{2}\right] \tag{3}$$

where n is the mode number of the radiation lobe which specifies the directionality of the source [15]. $P_S(\lambda)$ is the power emitted by the source in wavelength λ. Integrating $P_S(\lambda)$ over the source wavelength interval gives the nominal power generated by the source. Similarly, the receiver R is described by a five-tuple [15]

$$R = \{\boldsymbol{r}_R, \boldsymbol{n}_R, A_R, g(\theta), FOV\} \tag{4}$$

Here, $\boldsymbol{r}_R$, $\boldsymbol{n}_R$, A_R and FOV represent receiver position vector, orientation vector, physical area and field of view (semi-angle from the surface normal) of the receiver, respectively. $g(\theta)$ is the receiver optical gain function which is modeled as axial symmetric. This allows for a very general description of the receiver optical system. A typical model for a simple photodiode is $g(\theta) = cos(\theta)$. The cosine dependence models the decline in effective area for light incident on planar detectors at non-normal incidence. The effective area of the receiver at incident angle θ is given by [32]

$$A_{\mathit{eff}}\left(\theta\right) = A_{R_g}\left(\theta\right) \mathrm{rect}\left(\frac{\theta}{FOV}\right) \tag{5}$$

where $rect(x)$ is the rectangular function, whose value is 1 for $|x| \leq 1$ and 0 for $|x| \geq 1$.

The environment E is a room with any arbitrary shape such as rectangular, cylindrical or hexagonal room. Each wall is modeled as a diffuse reflective surface (Lambertian) of spectral reflectance of $\rho(\lambda)$.

When source S is transmitting, the signal received by receiver R is given by

$$Y(t) = X(t) * h(t) + N(t) \tag{6}$$

where "$*$" denotes convolution, $h(t)$ is the impulse response of the channel between source S and receiver R, and $N(t)$ is noise at the receiver R.

The impulse response $h(t)$, is fixed for a given set of source, receiver and environment, and for a special wavelength, (S, R, E, λ). Hence from now on, we write $h(t)$ more specifically as $h_E\left(t; S, R, \lambda\right)$. This definition also allows us to consider multiple transmitters and receivers at a time.

Considering the source S and receiver R, the multi-wavelength impulse response can be expressed as

$$h_E\left(t; S, R, \lambda\right) = h_E^{(0)}\left(t; S, R, \lambda\right) + \sum_{k=1}^{\infty} h_E^{(k)}\left(t; S, R, \lambda\right) \tag{7}$$

where $h_E^{(0)}\left(t; S, R, \lambda\right)$ is the LOS impulse response and $h_E^{(k)}\left(t; S, R, \lambda\right)$ is the impulse response of the light undergoing exactly k reflections, i.e., the multiple-bounce impulse response at time t and wavelength λ .

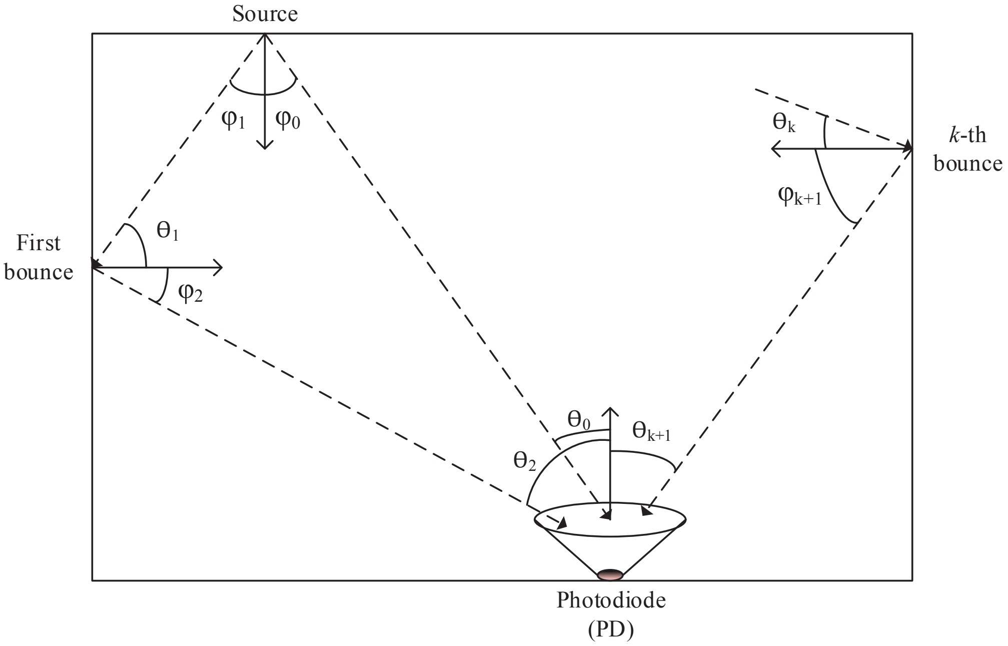

Figure 6: Geometry of source and receiver and reflected rays

Given the distance $d_{R,S} = |\boldsymbol{r}_R - \boldsymbol{r}_S|$ between source and receiver, we can decompose the LOS impulse response $h_E^{(0)}(t; S, R, \lambda)$ as [15]

$$h_E^{(0)}(t; S, R, \lambda) = L(\boldsymbol{r}_S, \boldsymbol{r}_R, E) \frac{A_{eff}(\theta)}{(d_{R,S})^2} R_S(n, \phi, \lambda) \, \delta\left(t - \frac{d_{R,S}}{c}\right) \tag{8}$$

where $L(\boldsymbol{r}_S, \boldsymbol{r}_R, E)$ is the LOS function and is equal to 1 if there is a LOS path between the source S and receiver R in environment E and is zero otherwise.

Light radiated from the source can reach the receiver after any number of reflections (see Fig. 6). In Monte Carlo ray-tracing algorithm, it is assumed that many rays are generated by the source with a probability distribution equal to its radiation pattern $R_S(n, \phi, \lambda)$. If $N(\lambda)$ is the number of rays with wavelength λ, the power of each ray can be estimated as $P_S(\lambda)/N(\lambda)$. It can be assumed that when a ray impinges on a surface, the reflection point is converted into a new optical source, thus a new ray is generated with a probability distribution provided by the reflection pattern of that surface [33]. After each reflection, the power of the ray is reduced by the reflection coefficient of the surface $\rho(\lambda)$. For each wavelength, the power and time instant of the mth ray generated by source $(1 \leqslant m \leqslant N(\lambda))$ after k reflections can be expressed by

$$P_{m,k}\left(S,R,\lambda\right)=\frac{A_{\mathit{eff}}\left(\theta_{\varepsilon_k,R}\right)}{\left(d_{\varepsilon_k,R}\right)^2}R_{\varepsilon_k}\left(\phi_{\varepsilon_k,R},\lambda\right) \tag{9}$$

$$t_{m,k}=\frac{d_{S,\varepsilon_1}}{c}+\left(\sum_{r=2}^{k}\frac{d_{\varepsilon_{r-1},\varepsilon_r}}{c}\right)+\frac{d_{\varepsilon_k,R}}{c} \tag{10}$$

where c is the speed of light. According to Lambert's model [21], $R_{\varepsilon_k}\left(\phi_{\varepsilon_k,R},\lambda\right)$, the reflection pattern of the diffusive surface is given by

$$R_{\varepsilon_k}\left(\phi_{\varepsilon_k,R},\lambda\right)=\frac{1}{\pi}\rho_k\left(\lambda\right)P_{m,k-1}\left(S,R,\lambda\right)\cos\left(\phi_{\varepsilon_k,R}\right) \tag{11}$$

Here, $P_{m,k-1}\left(S,R,\lambda\right)$ is the power of the mth ray before undergoing the kth reflection, which is given by

$$P_{m,k-1}\left(S,R,\lambda\right)=\frac{P_S\left(\lambda\right)}{N\left(\lambda\right)}\prod_{r=1}^{k-1}\rho_r\left(\lambda\right) \tag{12}$$

In the above equations, ε_k signifies an element of the diffusive surface where the kth reflection occurs. This element, with position vector, $\boldsymbol{r}_{\varepsilon_k}$, and orientation vector, $\boldsymbol{n}_{\varepsilon_k}$, plays the role of both an elemental receiver and an elemental source.

$\theta_{\varepsilon_k,R}$ is the angle between $\boldsymbol{n}_R$ and $\left(\boldsymbol{r}_{\varepsilon_k}-\boldsymbol{r}_R\right)$

$$\cos\left(\theta_{\varepsilon_k,R}\right)=\boldsymbol{n}_R.\frac{\left(\boldsymbol{r}_{\varepsilon_k}-\boldsymbol{r}_R\right)}{d_{\varepsilon_k,R}} \tag{13}$$

$\phi_{\varepsilon_k,R}$ is the angle between $\boldsymbol{n}_{\varepsilon_k}$ and $\left(\boldsymbol{r}_{\varepsilon_k}-\boldsymbol{r}_R\right)$

$$\cos\left(\phi_{\varepsilon_k,R}\right)=\boldsymbol{n}_{\varepsilon_k}.\frac{\left(\boldsymbol{r}_{\varepsilon_k}-\boldsymbol{r}_R\right)}{d_{\varepsilon_k,R}} \tag{14}$$

The multiple-bounce impulse response can be obtained by summing the power $P_{m,k}\left(S,R,\lambda\right)$ in (9) for the total number $N\left(\lambda\right)$ of rays, each undergoing a maximum of K reflections. By using the Dirac delta function

$$\begin{aligned}\sum_{k=1}^{\infty}h_E^{(k)}\left(t;S,R,\lambda\right)&=\sum_{m=1}^{N(\lambda)}\sum_{k=1}^{K}P_{m,k}\left(S,R,\lambda\right)\delta\left(t-t_{m,k}\right)\\&=\sum_{m=1}^{N(\lambda)}\sum_{k=1}^{K}\frac{A_{\mathit{eff}}\left(\theta_{\varepsilon_k,R}\right)}{\left(d_{\varepsilon_k,R}\right)^2}R_{\varepsilon_k}\left(\phi_{\varepsilon_k,R},\lambda\right)\delta\left(t-\left(\frac{d_{S,\varepsilon_1}}{c}+\left(\sum_{r=2}^{k}\frac{d_{\varepsilon_{r-1},\varepsilon_r}}{c}\right)+\frac{d_{\varepsilon_k,R}}{c}\right)\right)\end{aligned} \tag{15}$$

Substituting equations (8) and (15) in (7), the total channel impulse is expressed as

$$h_E\left(t;S,R,\lambda\right)=L\left(\boldsymbol{r}_S,\boldsymbol{r}_R,E\right)\frac{A_{\mathit{eff}}\left(\theta\right)}{\left(d_{S,R}\right)^2}R_S\left(n,\phi,\lambda\right)\delta\left(t-\frac{d_{S,R}}{c}\right)$$
$$+\sum_{m=1}^{N(\lambda)}\sum_{k=1}^{K}\frac{A_{\mathit{eff}}\left(\theta_{\varepsilon_k,R}\right)}{\left(d_{\varepsilon_k,R}\right)^2}R_{\varepsilon_k}\left(\phi_{\varepsilon_k,R},\lambda\right)\delta\left(t-\left(\frac{d_{S,\varepsilon_1}}{c}+\left(\sum_{r=2}^{k}\frac{d_{\varepsilon_{r-1},\varepsilon_r}}{c}\right)+\frac{d_{\varepsilon_k,R}}{c}\right)\right) \tag{16}$$

Finally, by integrating over λ, the total channel impulse response of the VLC channel for the wide spectrum of the visible light can be obtained as

$$h_E\left(t;S,R\right)=\int\limits_{\lambda}h_E\left(t;S,R,\lambda\right)d\lambda \tag{17}$$

The channel impulse response results based on this approach will be later provided in section 2.4.

2.3 Zemax®-based Non-sequential Ray Tracing

In this section, we characterize VLC channels through Zemax®13 software [31]. Zemax® is an optical and illumination design software with sequential and non-sequential ray-tracing capabilities. It allows an accurate description of the interaction of rays emitted from the LEDs for a user-defined indoor environment. In non-sequential ray-tracing, rays are traced along a physically realizable path until they intercept an object. The LOS response is straightforward to obtain and depends upon the LOS distance. Besides the LOS component, there is a large number of reflections between ceiling, walls, and floor as well as any other objects within the environment. The rays of light hit the other walls and are reflected towards the receiver. The receiver can only detect the rays entering its field of view. Those rays which are not directed towards the receiver, hit against the walls, ceiling and the floor and some of them are reflected towards receiver again for the other bounces. Rays may strike any group of objects in any order, or may strike the same object repeatedly; depending upon the geometry and properties of the objects. As an example, Fig. 6 illustrates the LOS and reflected rays within a cubic empty room.

The main difference of this method comparing to the previous one is its strength in calculating CIR for any scenario, especially environments with complicated geometries or sophisticated reflection patterns. Although the according to (16) and (17), the first method also has the potential to calculate the CIR for any scenario, its implementation in MATLAB is very complicated, if not impossible and it is necessary to make some assumptions (eg. empty rooms, cubic rooms, rectangular reflector surfaces and fixed value reflection coefficient) to reduce the complexity.

2.3.1 Methodology

We create a three dimensional indoor environment with specified dimensions in Zemax® and specify the geometry of the environment, the objects inside, the reflection characteristics of the surface materials as well as the specifications of the sources (i.e., LEDs) and receivers (i.e., photodiodes). The received optical power and the delay of direct/indirect rays are computed for the specified indoor environment and the corresponding channel impulse response (CIR) is obtained through proper normalizations. This information is then imported into MATLAB® and the corresponding CIR for that environment is obtained through proper normalizations.

In our work, we consider different configurations where we assume empty rectangular rooms with different sizes, LED numbers, transmitter/receiver locations and wall materials (i.e., brick, wood, black plaster), empty rooms with different shapes (i.e., L-shaped, circular) and furnished rooms. All related simulation parameters are summarized in Table 2.

As listed in Table 2, for all configurations except configuration 7, only one LED is used as the transmitter and it is placed at the center of the ceiling of the room. In configuration 7, assuming that the ceiling is divided into four quarters, 4 LEDs are located at the center of each quarter. Unlike an IR source that can be approximated

Table 2: Simulation parameters

Config.	Specifications	Room size (m^3)	Position of transmitter (m)	Position of receiver (m)	Reflectivity
1	empty room	1×1×3	(0, 0, 3)	(0, 0, 0) (0.3, 0.3, 0)	0.8
2	empty room	3×3×3	(0, 0, 3)	(0, 0, 0) (1.3, 1.3, 0)	0.8
3	empty room	5×5×3	(0, 0, 3)	(0, 0, 0) (2.3, 2.3, 0)	0.8
4	empty room	7×7×3	(0, 0, 3)	(2.3, 2.3, 0)	0.8
5	empty room	9×9×3	(0, 0, 3)	(2.3, 2.3, 0)	0.8
6	empty room	13×13×5	(0, 0, 5)	(2.3, 2.3, 0)	0.8
7	empty room	5×5×3	(1.25, 1.25, 3) (1.25, -1.25, 3) (-1.25, 1.25, 3) (-1.25, -1.25, 3)	(0, 0, 0) (2.3, 2.3, 0)	0.8
8	empty room	5×5×3	(0, 0, 3)	(2.3, 2.3, 0)	Bare red brick
9	empty room	5×5×3	(0, 0, 3)	(2.3, 2.3, 0)	Pine wood
10	empty room	5×5×3	(0, 0, 3)	(2.3, 2.3, 0)	Black gloss paint
11	L-shaped room	See Fig. 9	(0, 0, 3)	(2.3, 2.3, 0)	0.8
12	circular room	See Fig. 10	(0, 0, 3)	(2.3, 2.3, 0)	0.8
13	hotel room	5×5×3	(0, 0, 3)	(2.3, 2.3, 0)	0.8

as a monochromatic emitter, a white light LED source is inherently wideband (380-780 nm). This calls for the inclusion of wavelength-dependent channel in VLC channel modeling. In our simulations, we use the specifications of Cree Xlamp® MC-E Color (RGBW) LED with Lambertian distribution and a viewing angle of 110° [34]. It provides high brightness and efficient color mixing from a single, compact package that enables a wide range of lighting applications. This source model is available at Radiant Zemax® online source library [31]. Figure 7 depicts relative power distribution of this LED within its working wavelength range.

In all the configurations under consideration, the photodetector (PDs) is located either at the center or the corner of the floor pointing upward. The corresponding coordinates of PDs are listed in Table 2. PDs are basically modelled as rectangular detector surfaces. In addition, the FOV and area of PDs are assumed to be 90° and 1 cm^2, respectively.

In our channel modeling study, we assume the Lambertian reflection property for

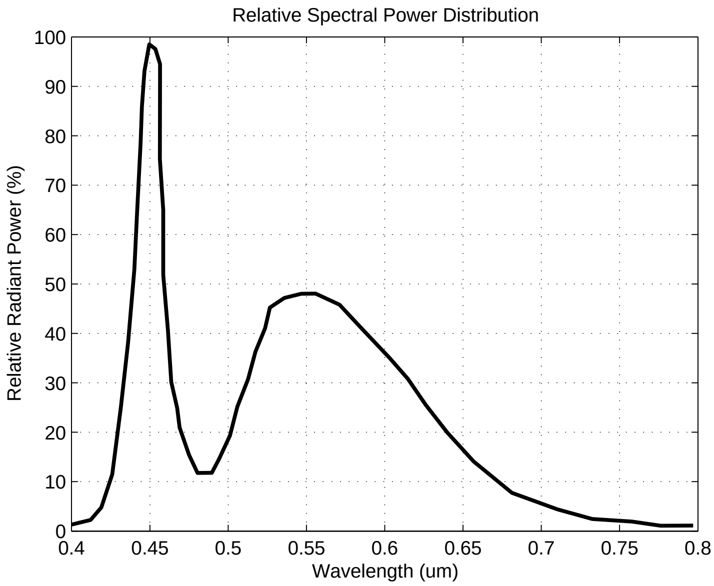

Figure 7: Relative spectral power distribution of Cree Xlamp® MC-E Color (RGBW) LED

the reflectance parameter of walls for interference effect and reflectance in order to provide a more realistic scene. It is known that the reflection pattern of most surfaces can correctly be approximated using the Lambert or the Phong models [21, 35]. If there are strong specular components in the reflection pattern of the surfaces, the Phong model approximates those patterns well unlike that of the Lambert model. Therefore, because the reflection patterns are diffuse, they can correctly be approximated using the Lambertian reflection model. Furthermore, as the reflectance characteristics of indoor materials are wavelength dependent, they should not be assumed to have a constant value. In order to account for the wideband nature of VLC links, the reflectance of materials in the visible spectrum should be taken into consideration. We use the spectral reflectance of three types of materials for the walls of the rooms. These values are adopted from [36] and are shown in Fig. 8.

As listed in Table 2, for configurations 1 to 6, empty rectangular rooms with different dimensions are considered. The reflection coefficient of walls for all these rooms is assumed to be a constant value of 0.8, which is the reflectance of typical plaster materials used in indoor environments [14]. Configurations 8, 9 and 10 are

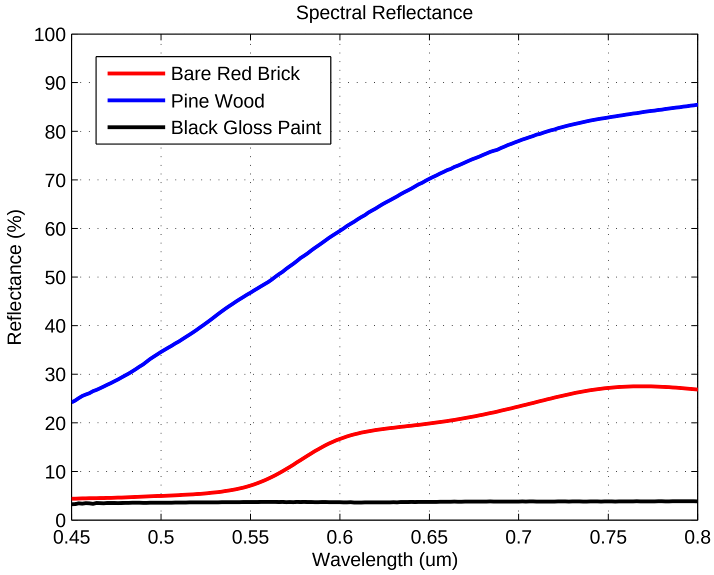

Figure 8: Spectral reflectance of materials used for walls

the same as configuration 3, except that walls are coated with special materials (bare red brick, pine wood and black gloss paint). In contrast to previous configurations which were all rectangular rooms, configurations 11 and 12 represent environments with irregular shapes, see Fig. 9 and 10. Configuration 13, see Fig. 11, is a rectangular furnished hotel room with dimensions the same as configuration 3 and modeled using CAD objects available at [37].

2.3.2 Channel Characterization

The Zemax® non-sequential ray-tracing tool generates an output file, which includes all the data about rays such as the detected power and path lengths for each ray. We import the data from Zemax® output file to MATLAB® and using these information, we express the CIR as

$$h(t) = \sum_{i=1}^{N_r} P_i \delta(t - \tau_i) \tag{18}$$

where P_i is the power of the ith ray, τ_i is the propagation time of the ith ray, $\delta(t)$ is the Dirac delta function and N_r is the number of rays received at the detector. Based on the obtained CIRs, we can further quantify fundamental channel characteristics. Channel DC gain (H_0) is one of the most important features of a VLC channel, as it

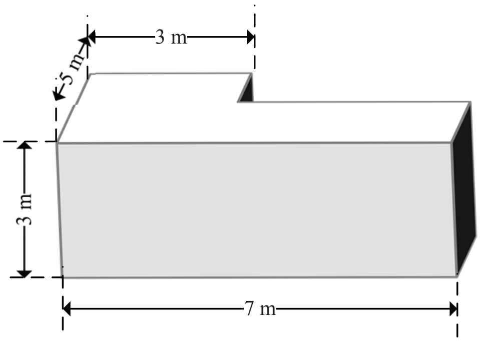

Figure 9: Geometry of configuration 11, L-shaped room

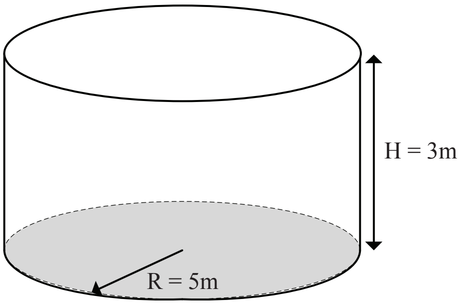

Figure 10: Geometry of configuration 12, circular room

Figure 11: Geometry of configuration 13, hotel room

determines the achievable signal-to-noise ratio for fixed transmitter power. The delay profile is composed of dominant multiple LOS links and a less number of NLOS delay taps. The temporal dispersion of a power delay profile can be expressed by the mean excess delay (τ_0) and the channel root mean square (RMS) delay spread (τ_{RMS}) [22]. These parameters are given by

$$\tau_0 = \frac{\int_0^\infty t \times h(t)dt}{\int_0^\infty h(t)dt} \tag{19}$$

$$\tau_{RMS} = \sqrt{\frac{\int_0^\infty (t-\tau_0)^2 h(t)dt}{\int_0^\infty h(t)dt}} \tag{20}$$

On the other hand, the channel DC gain (H_0) is calculated as

$$H_0 = \int_{-\infty}^{\infty} h(t)dt \tag{21}$$

2.4 Simulation Results

2.4.1 Comparison of Methods

In this section, we first compare the two proposed methods in terms of accuracy and computational time. Recall that, the first method is the extension of Barry's algorithm for VLC channels which is simulated in MATLAB (see Section 2.2) and the second one is non-sequential ray-tracing in Zemax® (see Section 2.3).

For both cases, an empty 5.0×5.0×3.0 m^3 rectangular room is considered with a first order Lambertian source at (0, 0, 3) and a detector located at (1.5, 1.5, 0) with OV of 90° and area of 1 cm^2. In order to use the first method, each wall of the room is divided into 100 pixels, and only one reflection is considered, while Zemax® can trace rays up to 30 reflections.

Figure 12 shows obtained CIRs using these two methods. It takes 90.34 seconds for MATLAB and 47.734 seconds for Zemax® to generate these results. Zemax® can keep track of rays with higher order reflections with lower amount of time, hence, providing significantly increased accuracy in the CIR results. It can also be seen that the power of diffuse part of the CIR is higher in Fig. 12 (b) compared to Fig. 12 (a) and the reason is that MATLAB has ignored rays with more than one bounce.

Figure 13 shows the distribution of received power at the floor of the room using the two methods. It takes 8559 seconds for MATLAB and 47.734 seconds for Zemax® to generate these results, which is 180 times faster than MATLAB. Here MATLAB needs to calculate the received power for all the pixels of the floor surface and this has considerably increased the computational time while Zemax® does this by default.

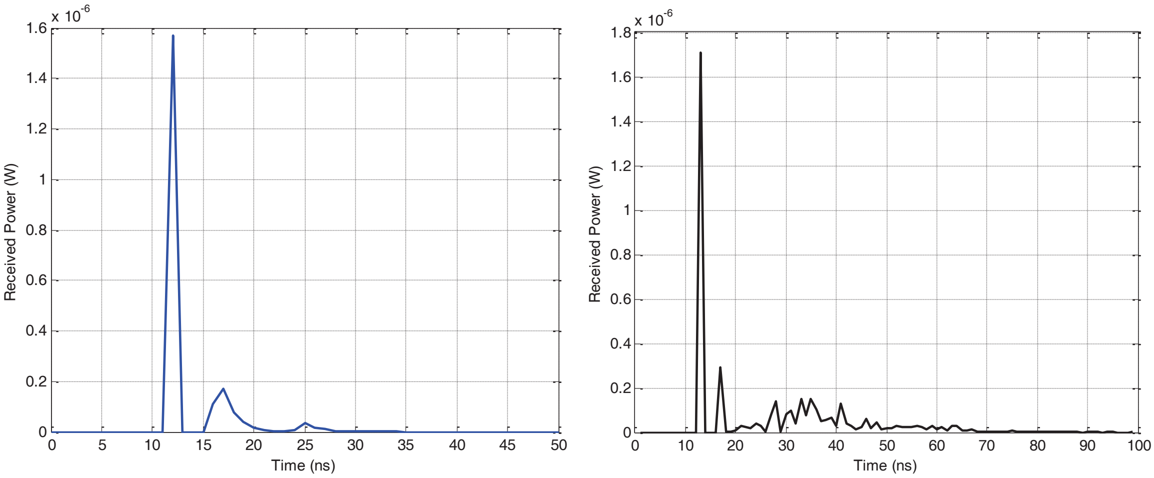

(a) (b)

Figure 12: CIRs obtained by (a) MATLAB and (b) Zemax

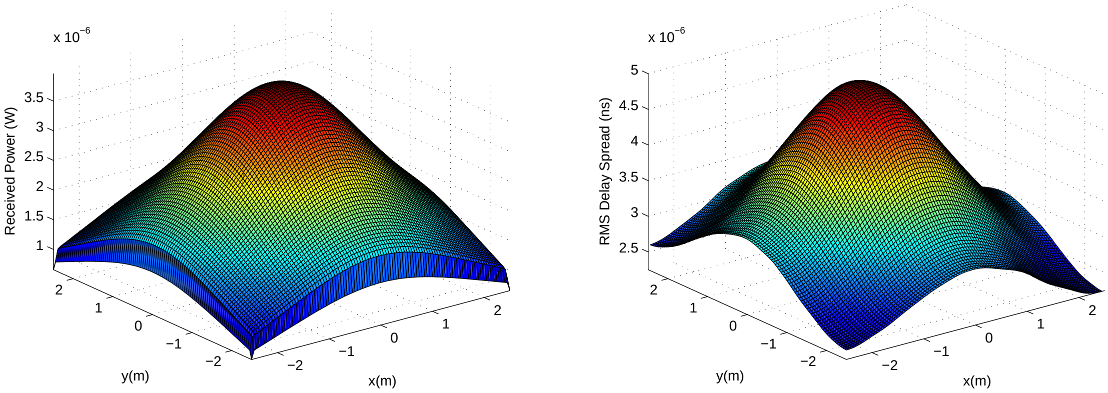

(a) (b)

Figure 13: Distribution of received power obtained by (a) MATLAB and (b) Zemax

Again, it can be noticed that the received power is greater in Fig. 13 (b) due to considering up to 30 reflections.

Figure 14 and 15 show the distribution of mean excess delay and RMS delay spread, at the floor of the room, respectively. It takes 9349 seconds for MATLAB and 47.734 seconds for Zemax® to generate these results, which is 200 times faster than MATLAB. According to these figures, MATLAB results for mean excess delay and RMS delay spread are stepwise and discretized while results of Zemax® are smooth and continuous. This is because of dividing the surfaces into some pixels. The more the number of pixels is, the smoother the distributions of dispersion parameters become.

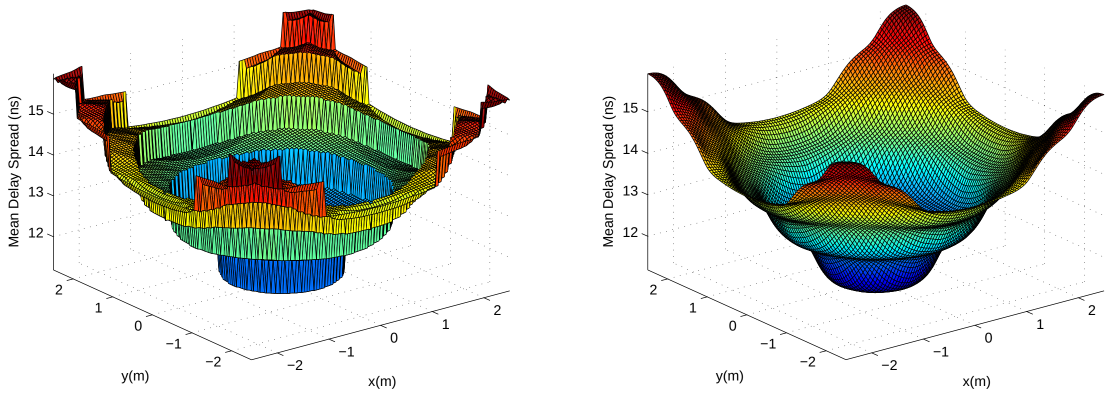

(a) (b)

Figure 14: Distribution of mean excess delay obtained by (a) MATLAB and (b) Zemax

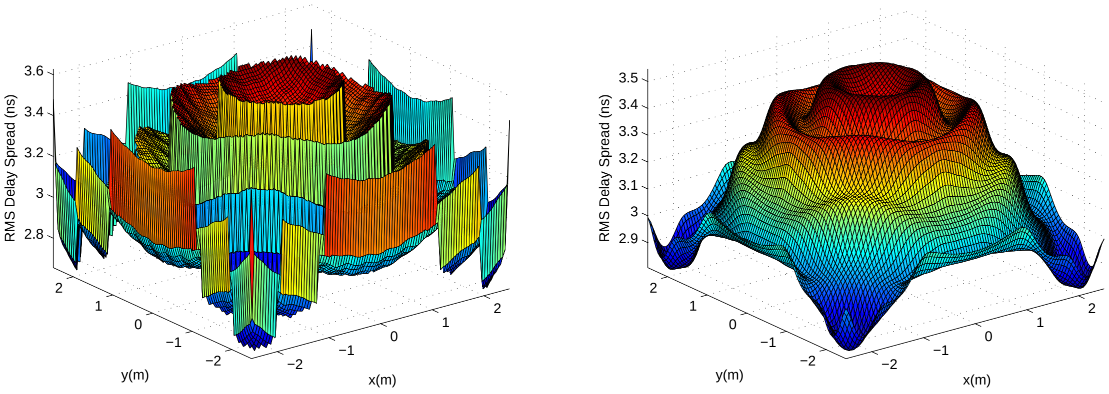

(a) (b)

Figure 15: Distribution of RMS delay spread obtained by (a) MATLAB and (b) Zemax

In the remaining parts of this thesis, Zemax® is used for characterizing the VLC channels. Because it can produce more accurate results in lower amount of time.

2.4.2 CIRs and Channel Parameters

The CIRs for configurations 1 to 13 are provided in Fig. 16-23

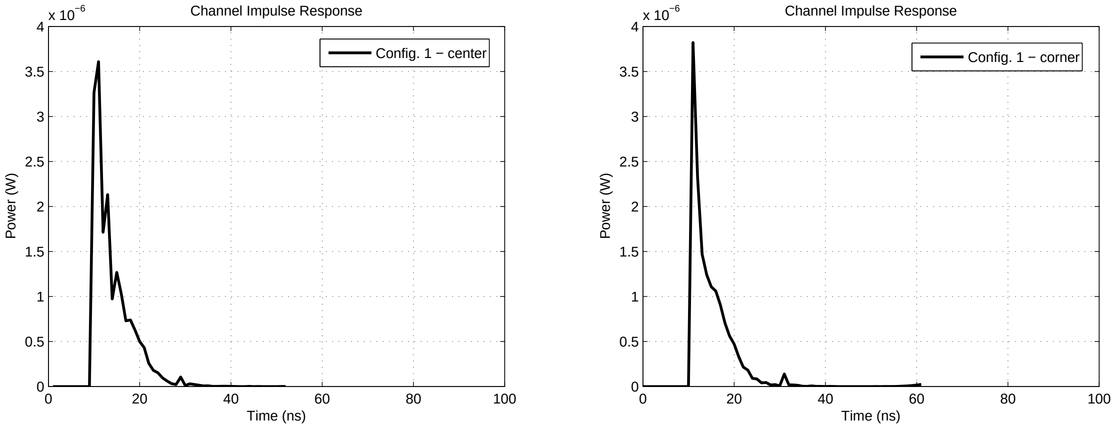

(a) (b)

Figure 16: CIRs for Config. 1, detector at (a) center and (b) corner of the floor

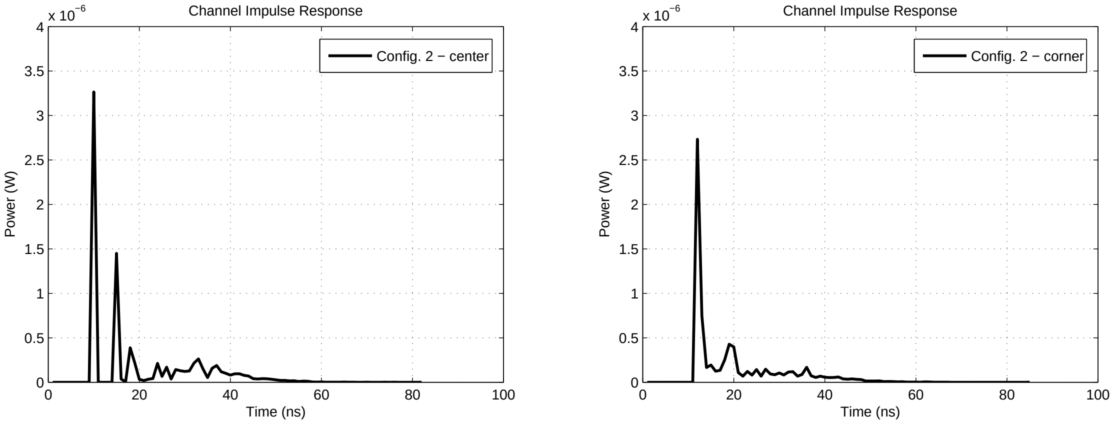

(a) (b)

Figure 17: CIRs for Config. 2, detector at (a) center and (b) corner of the floor

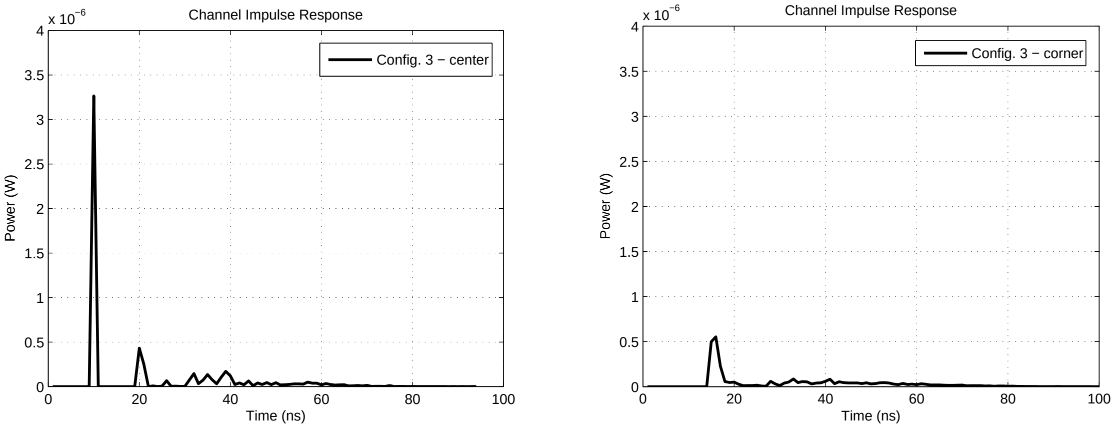

(a) (b)

Figure 18: CIRs for Config. 3, detector at (a) center and (b) corner of the floor

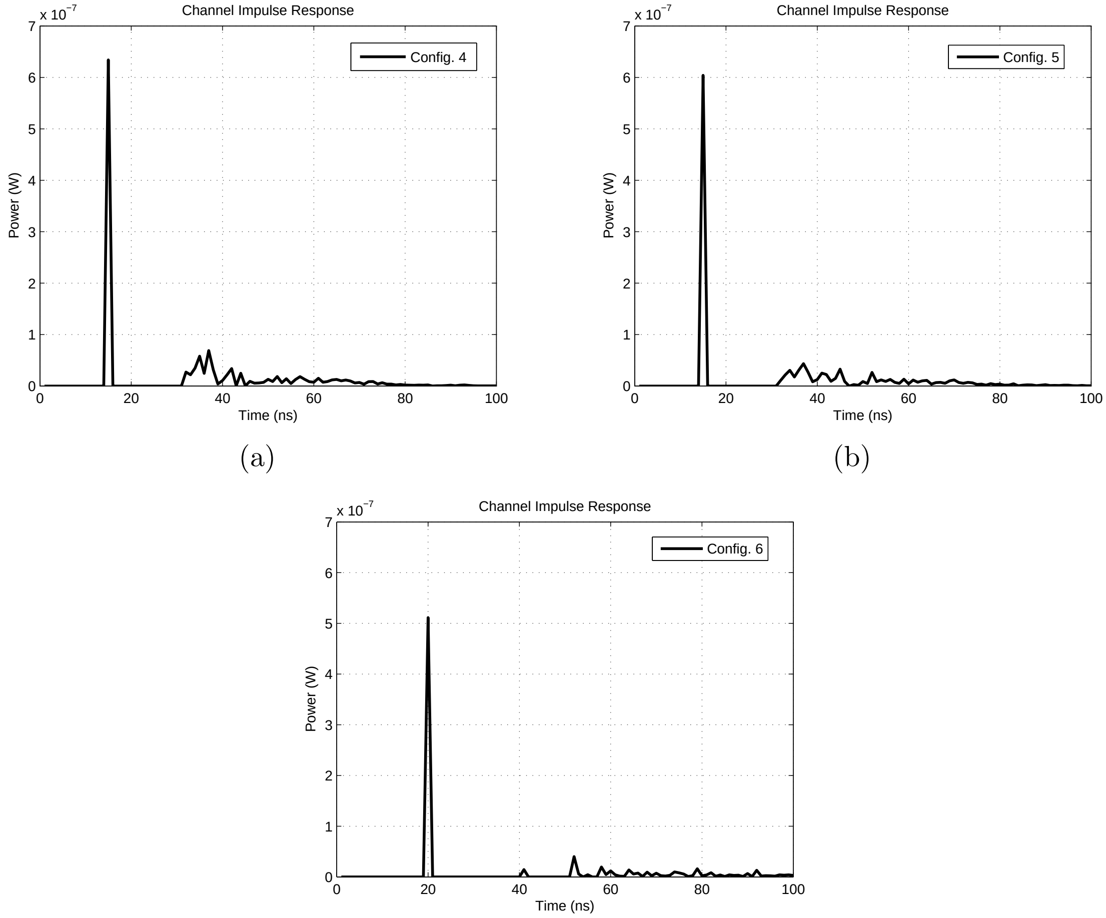

(a)

(b)

(c)

Figure 19: CIRs for (a) Config. 4, (b) Config. 5 and (c) Config. 6

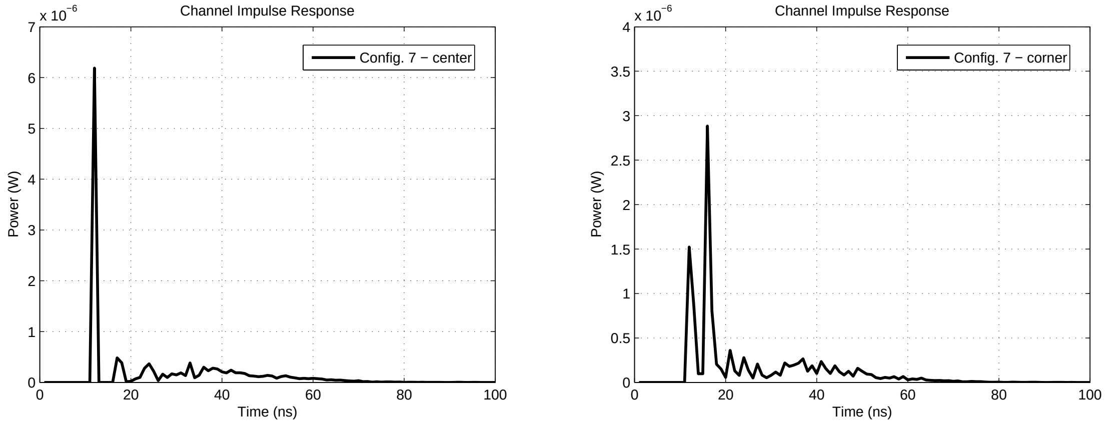

(a)

(b)

Figure 20: CIRs for Config. 7, detector at (a) center and (b) corner of the floor

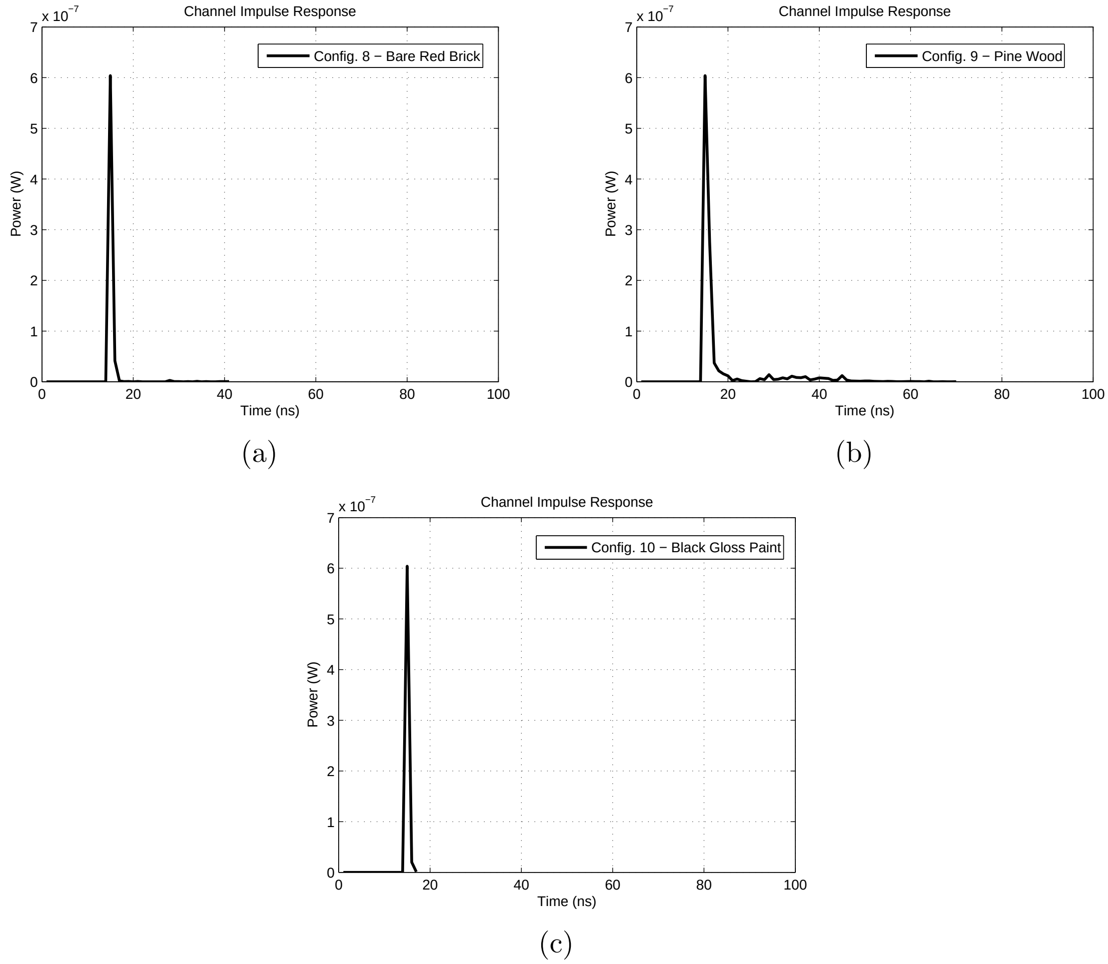

(a) (b) (c)

Figure 21: CIRs for (a) Config. 8, (b) Config. 9 and (c) Config. 10

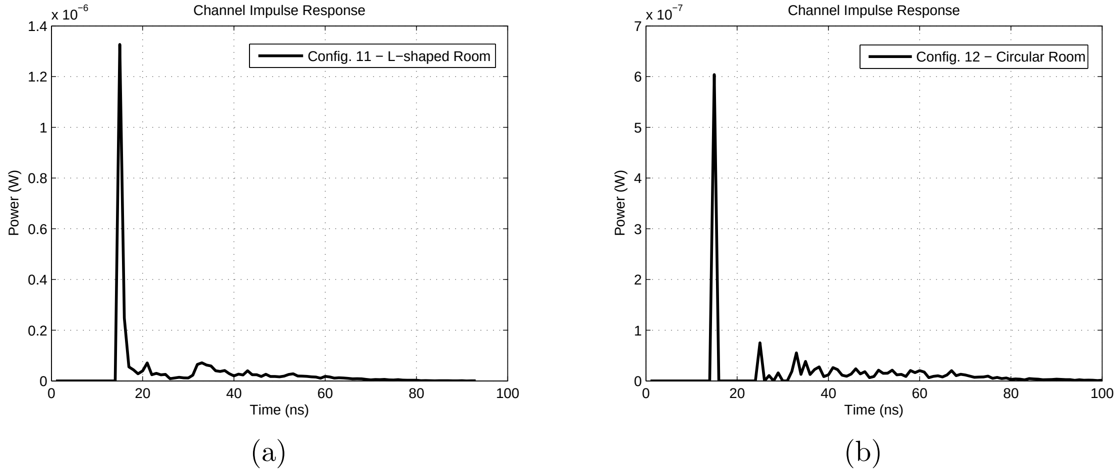

(a) (b)

Figure 22: CIRs for (a) Config. 11, and (b) Config. 12

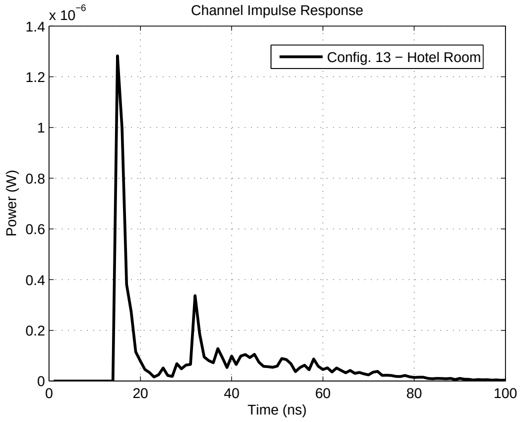

Figure 23: CIR for Config. 13

For the configurations under consideration, the channel parameters are calculated and provided in Table 3.

Table 3: Time dispersion parameters

Config.	H_0	τ_0 (ns)	τ_{RMS} (ns)
1- center	1.80e-05	11.3011	3.0769
1- corner	1.67e-05	13.5313	3.2176
2- center	8.49e-06	16.1786	6.8174
2- corner	7.54e-06	18.6051	8.8889
3- center	5.83e-06	20.1412	10.6192
3- corner	2.51e-06	26.7856	13.6364
4	1.32e-06	30.4723	18.2671
5	7.84e-07	38.0349	25.8093
6	3.14e-07	41.7489	29.6919
7- center	1.77e-05	22.3983	13.06074
7- corner	1.34e-05	22.6181	13.1254
8	6.54e-07	14.8619	0.3152
9	1.12e-06	17.1517	6.0772
10	6.25e-07	15.0083	0.1774
11	3.97e-06	21.3380	11.7242
12	1.47e-06	33.1400	19.9478
13	6.91e-06	30.6492	17.46094

2.4.3 Assessment and Comparison

From the CIR results and Fig. 24, it can be observed that for configurations 1,2 and 3, when the PD is at the center of the room, the amplitude of the received optical power (mainly from LOS path) is greater than the received power when the PD is moved to the corner of the floor. It is also obvious that the LOS path is delayed for the corner detector, since the LOS rays have to travel longer paths to reach the detector.

Comparing the results of configurations 1, 2 and 3, it can be concluded that when the detector is at the middle of the floor, the peak value of CIR does not change for different room dimensions. It is due to the fact that LOS path for these configurations is the same. However, as the dimensions of the room increases, the channel DC gain, H_0, decreases and less power is received at the detector.

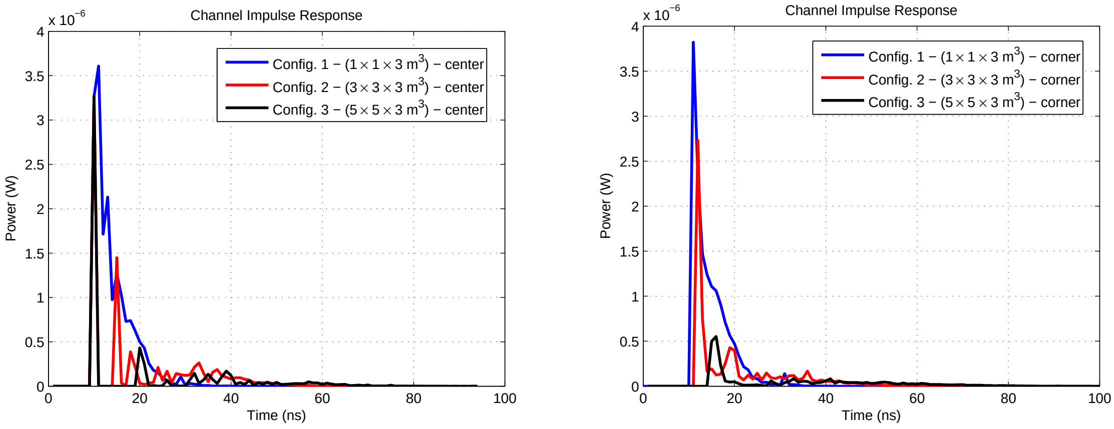

(a) (b)

Figure 24: CIR for Configs. 1, 2 and 3, detector at (a) center and (b) corner of the floor

Comparing the numerical values provided in Table 3 for configurations 3 to 6, it is deduced that as the dimensions of room increases, the channel DC gain decreases and less power is received at the detector. Moreover, since rays have to travel longer paths to reach the detector, the values for τ_0 and τ_{RMS} increase.

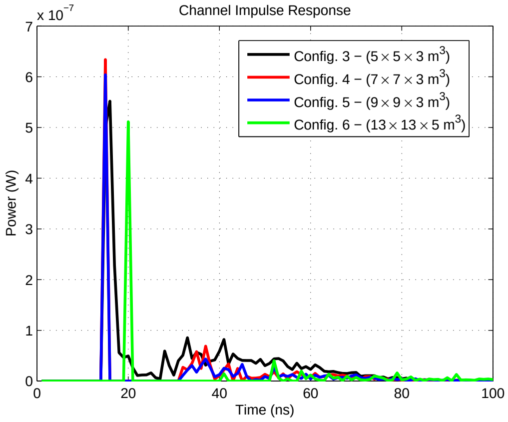

Figure 25: CIR for Configs. 3, 4, 5 and 6

Comparing the CIR results for configurations 3 and 7, it is observed that the number of LED sources and location of them, have considerable effect on the channel parameters. In these two configurations, when detector is located at the center of the floor, the LOS ray is delayed due to having longer distance from the detector and since it is the combination of 4 separate LOS paths, CIR has a greater peak value. Also, channel DC gain and dispersion parameters have been increased.

For the scenario in which detector is at the corner of the room, although H_0 increase, τ_0 and τ_{RMS} do not change considerably. It should also be noted that, in this case, LOS paths do not travel same distance to reach the detector. This makes the CIR to have other noticable peaks as in Fig. 26.

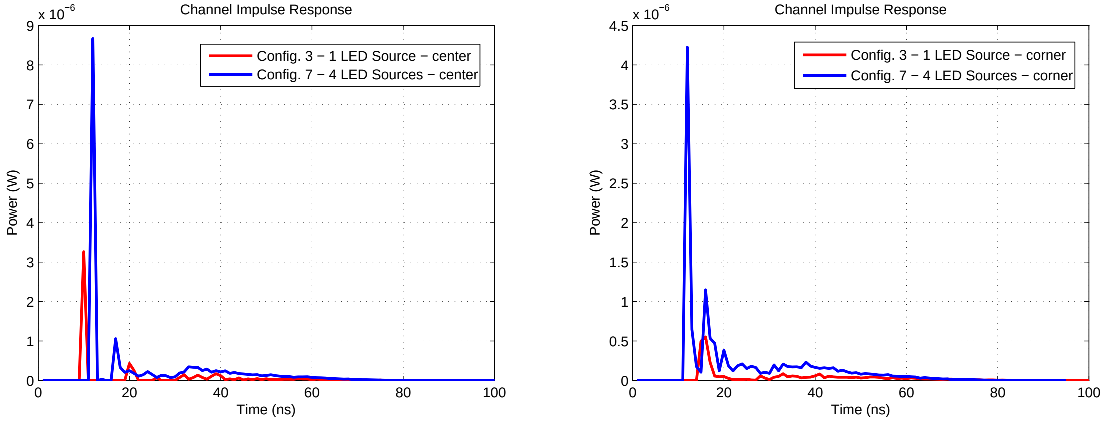

(a) (b)

Figure 26: CIR for Configs. 3 and 7

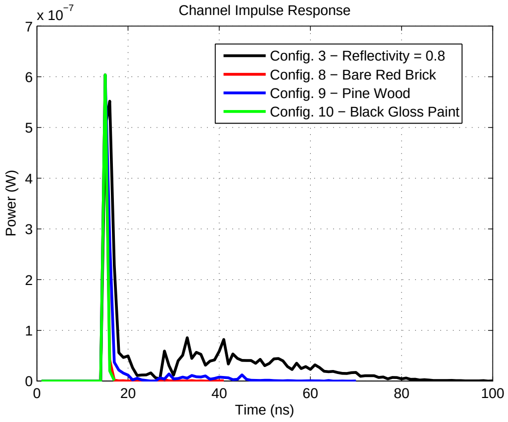

Figure 27: CIR for Configs. 3, 8, 9 and 10

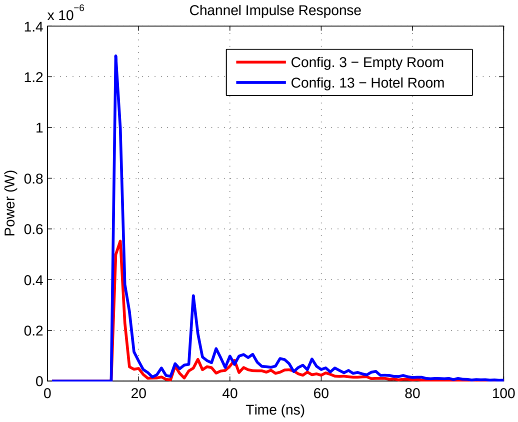

Figure 28: CIR for Configs. 3, 8, 9 and 10

According to CIR results in Fig. 27, it is clearly seen that in contrast to IR communications, in which the received power from reflected paths tends to add to a significant amount regardless of the type of the indoor walls, for the VLC channel, the received power from reflected paths largely depends on building materials [22]. It can also be concluded that the building materials have considerable effect on the values of mean excess delay and RMS delay spread.

From Fig. 22 and Table 3, we can also observe that the channel DC gain, mean excess delay and RMS delay spread are highly dependent on the shapes and dimensions of the room.

The two rooms of configurations 3 and 13 are identical in size and transmitter/receiver placement, yet the CIRs differ greatly, as shown in Fig. 28. Furthermore, τ_0 and τ_{RMS} show a difference of 4 ns. This can be explained by the fact that for the LOS channels with furniture, the transmitter has a higher probability of being near an object which can scatter the initial transmission causing an increase in delay spread and received power. In addition the indirect rays have to travel around more objects to reach a receiver, increasing the RMS delay spread.

CHAPTER III

STATISTICAL CHARACTERIZATION OF VLC CHANNELS

In the previous chapter, we have developed CIRs for VLC channels in various environments. In this chapter, we develop statistical models for characterization of indoor VLC channels through examination of a large set of CIRs. We analyze the collected channel gains and delay spreads to determine general trends and find statistical distributions to fit them.

3.1 Methodology

To begin, an empty $5.0 \times 5.0 \times 3.0$ m^3 cubic room is considered. The source is Cree Xlamp® MC-E Color (RGBW) LED with Lambertian distribution and a viewing angle of 110° and is placed at the center of the ceiling pointing downward. One thousand receivers, which are rectangular detectors with FOV of 90° and area of 1 cm^2, are considered. The reflectivities of the walls are assumed to be 0.8.

Detectors are randomly placed around the source, uniformly distributed over a half-sphere of radius D_{tr} and all of them are assumed to be inside the room. The orientation angles of the detectors are determined by two random variables, the elevation and azimuth. The azimuth is a uniformly distributed random variable between $[0,\ 2\pi]$, and the cosine of the elevation is a uniformly distributed random variable between [0, 1]. These are the necessary conditions to have the angles uniformly distributed over a sphere [32, 38]. These steps are repeated for different values of D_{tr} and a total of 1000 CIRs are collected for each scenario.

We then run the non-sequential ray-tracing for 10^6 rays. Zemax® stores the power and length of all traced rays. Rays received at each detector are separated and the corresponding CIR for that detector is obtained. All the 1000 impulse responses are evaluated and two sets of data are collected, channel DC gain and RMS delay spread. Once all the necessary data is collected, we proceed with analyzing the data to model the statistical behavior of the channel.

3.2 Channel DC Gain

Channel gain is one of the most important features of a VLC channel. It determines the achievable signal-to-noise ratio for fixed transmitter powers and is important regardless of the data rate or modulation scheme employed.

We analyze the data collected from Zemax® and look at the trends in channel DC gain as D_{tr} changes. This section discusses about the histograms of the channel gain data collected from Zemax® for a 5.0×5.0×3.0 m^3 empty cubic room and different values of D_{tr}.

Figure 29 shows the channel gain distributions for each value of D_{tr}. Plotted atop the channel gain histograms are dashed lines corresponding to the mean values. For all distances the shape of the histograms are similar. The data rises fast for small channel gains and tails off for higher channel gains. These shapes will be discussed further and analyzed in section 3.4.

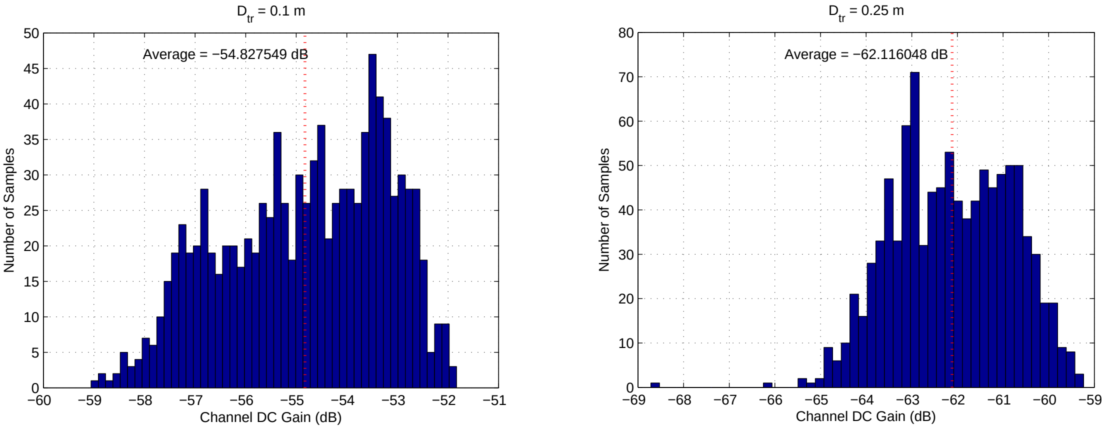

(a) $D_{tr} = 0.1$ m

(b) $D_{tr} = 0.25$ m

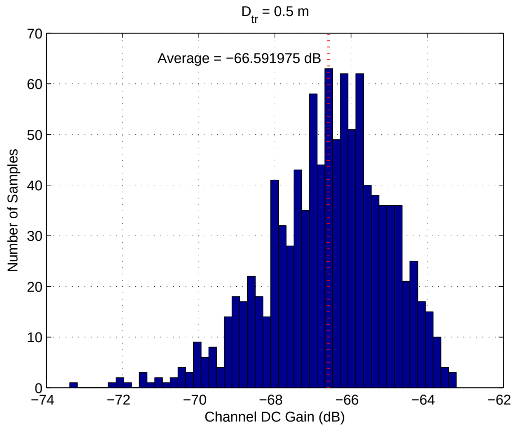

(c) $D_{tr} = 0.5$ m

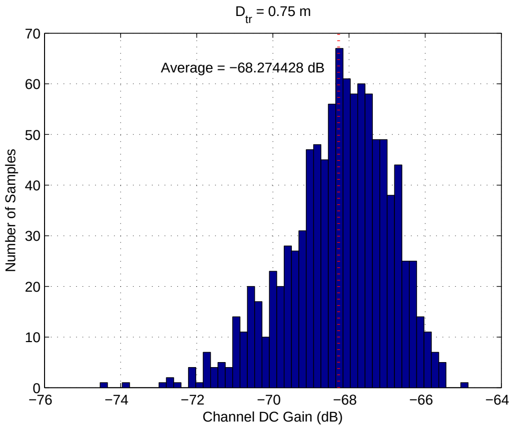

(d) $D_{tr} = 0.75$ m

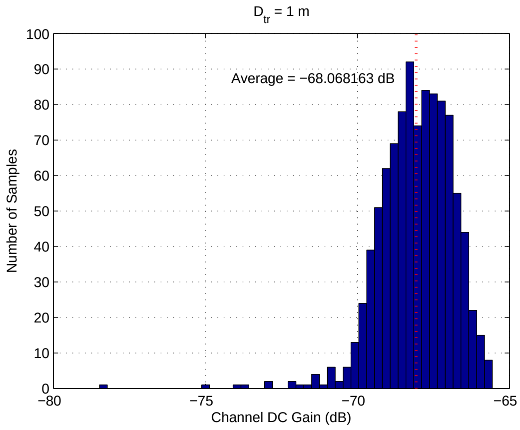

(e) $D_{tr} = 1$ m

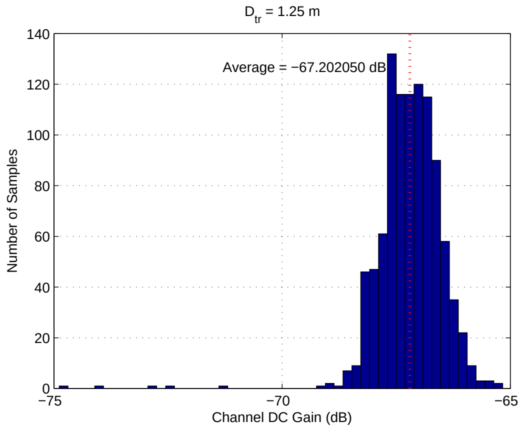

(f) $D_{tr} = 1.25$ m

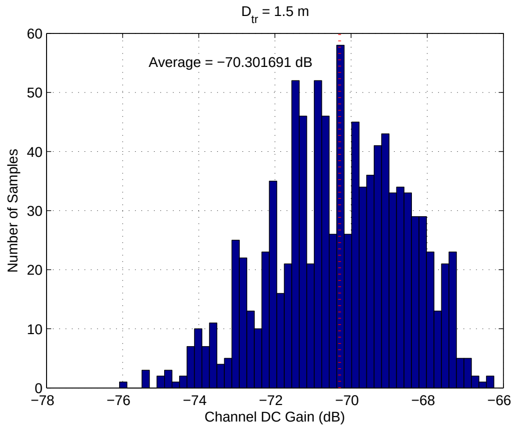

(g) $D_{tr} = 1.5$ m

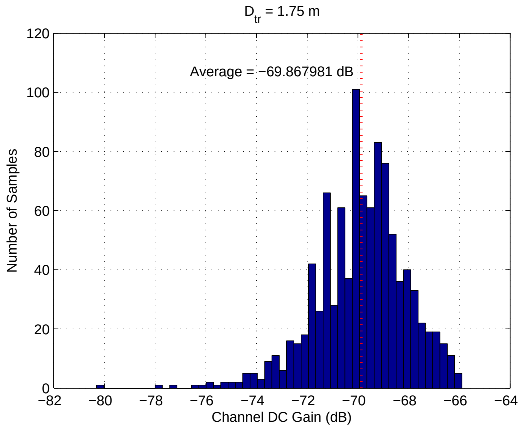

(h) $D_{tr} = 1.75$ m

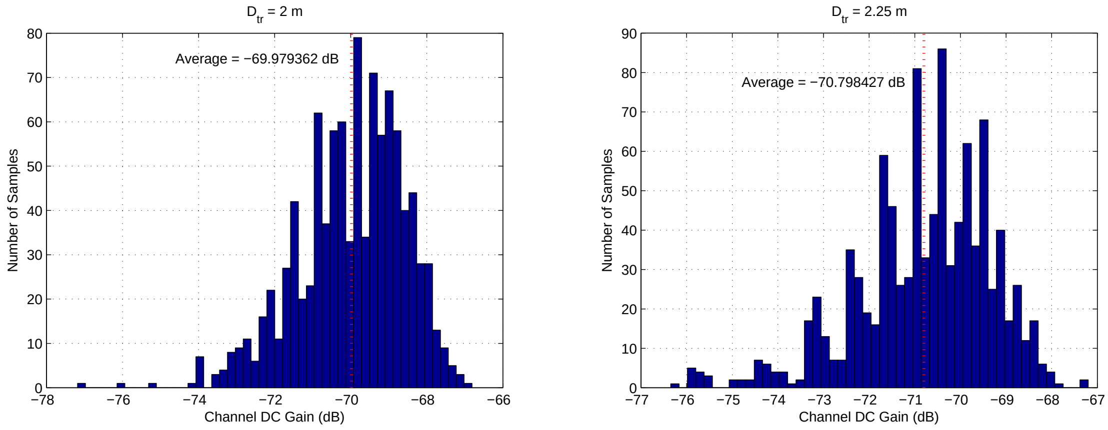

(i) $D_{tr} = 2$ m

(j) $D_{tr} = 2.25$ m

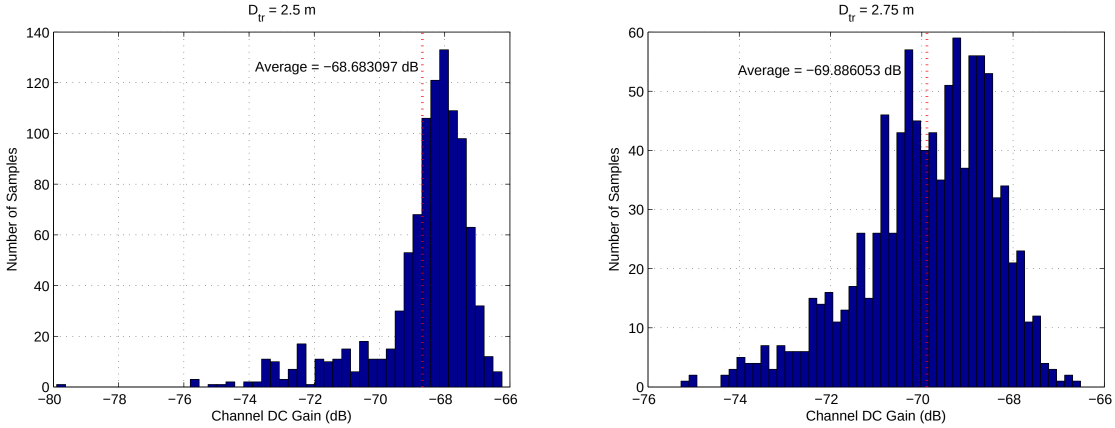

(k) $D_{tr} = 2.5$ m

(l) $D_{tr} = 2.75$ m

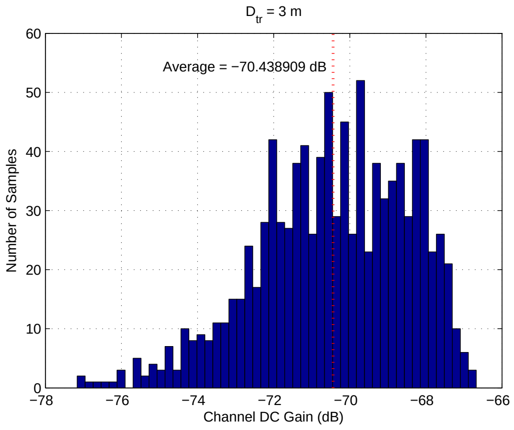

(m) $D_{tr} = 3$ m

Figure 29: Channel gain histograms in a 5×5×3 m^3 room

Now we focus on the trends in the mean of our channel gain data. According to Fig. 30, each point corresponds to the mean of a histogram such as those seen in Fig. 29. At close distances the power received directly from the transmitter is significantly higher than when the transmitter and receiver are further away. The mean value decreases by 12 dB when D_{tr} increases from (a) 0.1 m to (c) 0.5 m. This trend continues until 1.5 m, after that point the mean value shows small changes.

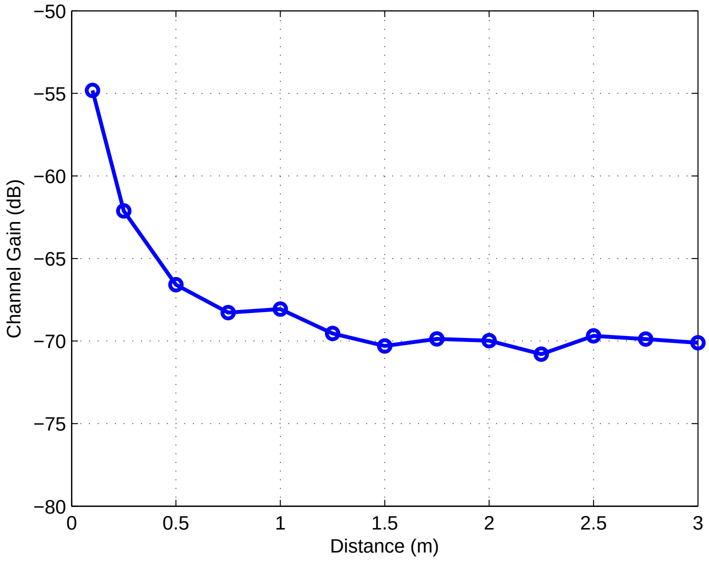

Figure 30: The average channel gain of all data collected using Zemax®

3.3 RMS Delay Spread

It is important not only to look at channel gain but the delay spread of a signal. The delay spread will be increasingly important for higher data rates. This section presents trends in histograms for individual data samples, and trends in the mean of the data. From now on, for simplicity, RMS delay spread will be referred to as delay spread.

Plotted in Fig. 31 are the delay spread histograms for the same room and distances seen in Fig. 29. Dashed lines correspond to the mean values. According to Fig. 31, for small values of D_{tr}, the delay spread is lower because the power received from the

LOS component is so strong that additional components from higher order bounces are virtually null. As distance increases, the initial power received from the LOS path falls off, making any additional multipath components more effective.

The mean delay spread is plotted in Fig. 32. The delay spread depends on the time and impulse response values and for LOS channels, it is dictated mostly by the LOS path. According to Fig. 32, the average delay spread increases very fast for the Dtr values less than 0.75 m, but then starts to level off, and even decreases. These trends can be examined more thoroughly if we extend our experiments to larger room sizes, furnished rooms and consider different materials for reflector surfaces.

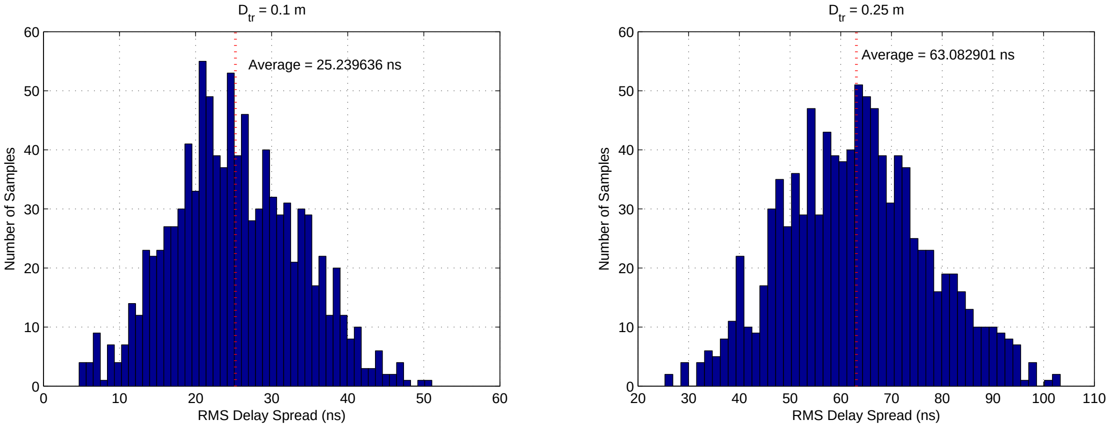

(a) $D_{tr} = 0.1$ m

(b) $D_{tr} = 0.25$ m

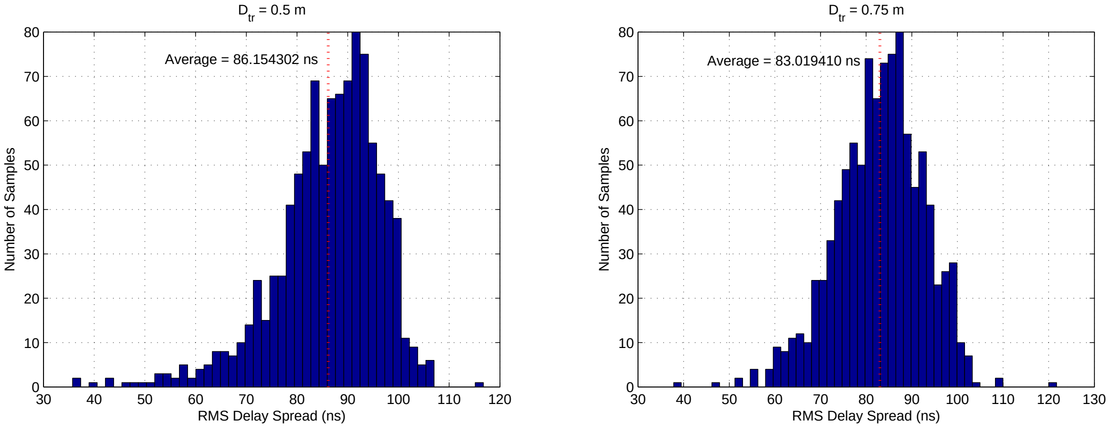

(c) $D_{tr} = 0.5$ m

(d) $D_{tr} = 0.75$ m

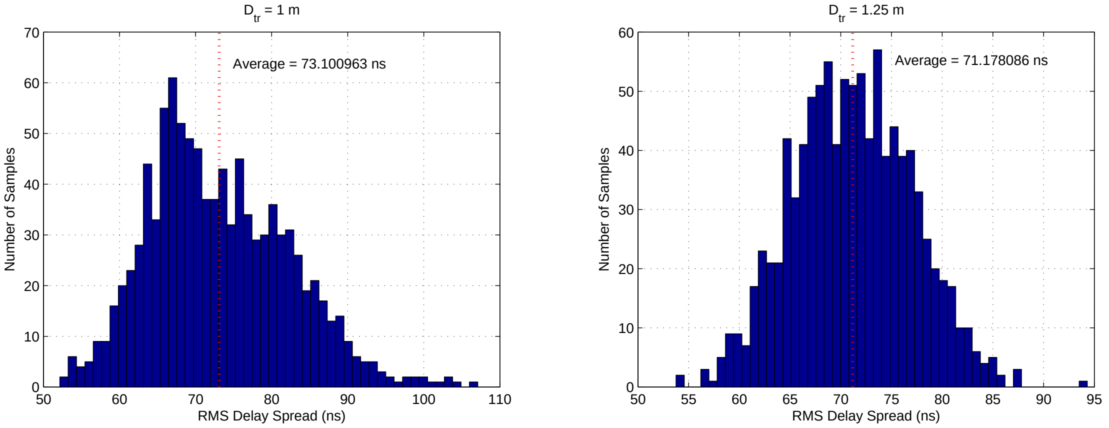

(e) $D_{tr} = 1$ m

(f) $D_{tr} = 1.25$ m

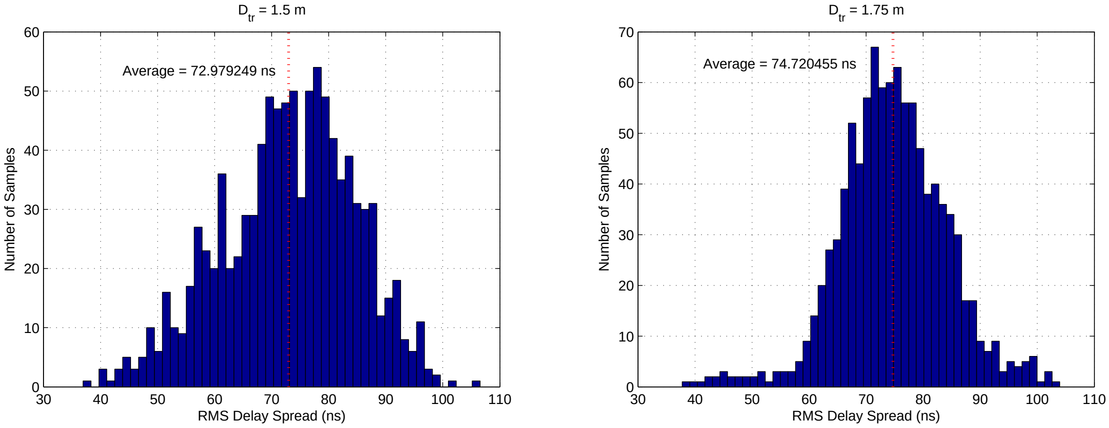

(g) $D_{tr} = 1.5$ m

(h) $D_{tr} = 1.75$ m

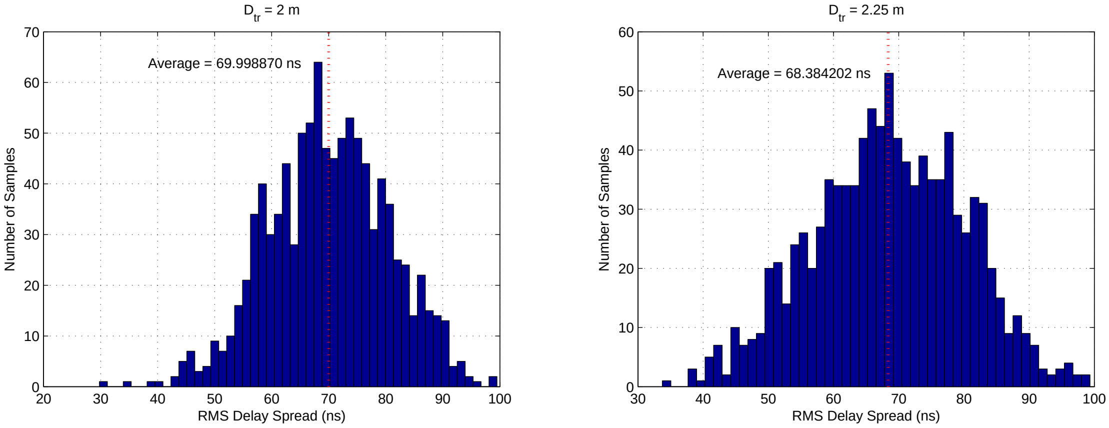

(i) $D_{tr} = 2$ m

(j) $D_{tr} = 2.25$ m

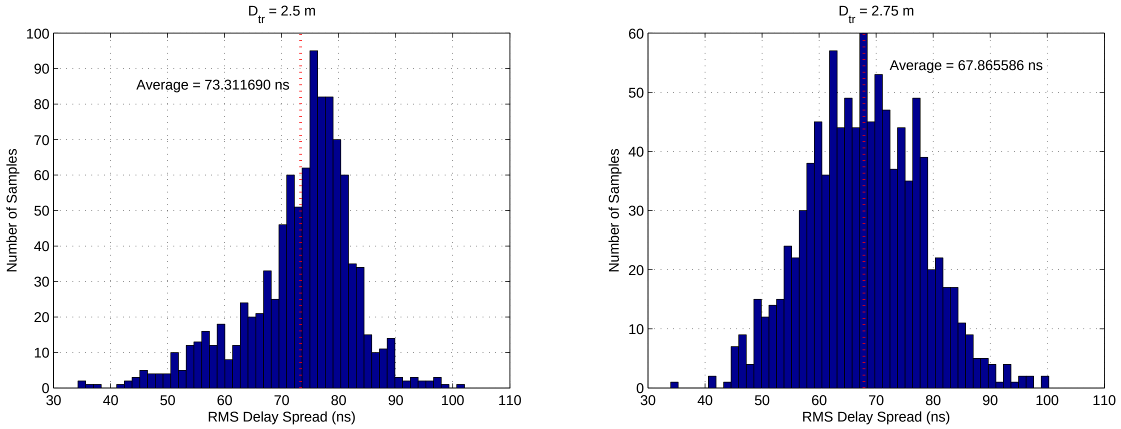

(k) $D_{tr} = 2.5$ m

(l) $D_{tr} = 2.75$ m

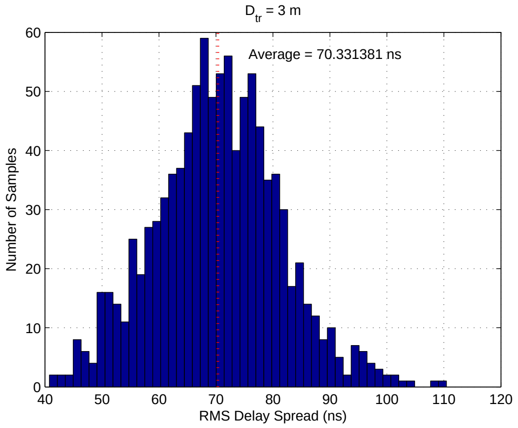

(m) $D_{tr} = 3$ m

Figure 31: RMS delay spread histograms in a 5×5×3 m^3 room

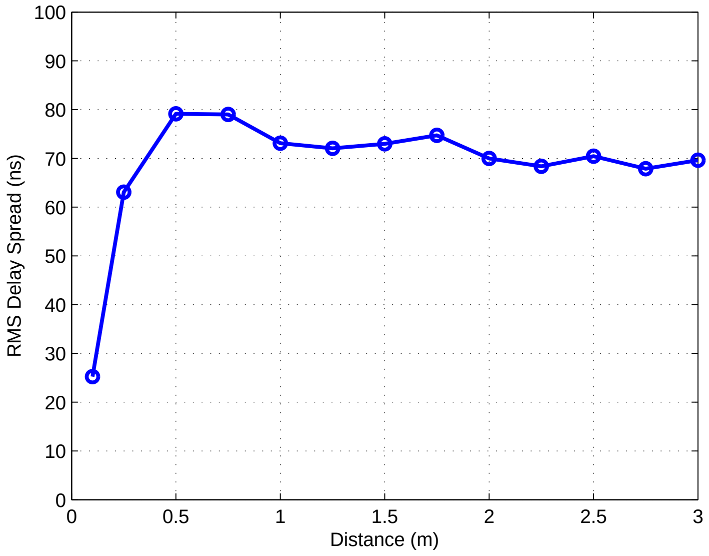

Figure 32: The average RMS delay spread of all data collected using Zemax®

3.4 Distribution of Channel Gain and RMS Delay Spread

The goal of this section is to present statistical models based on the data provided in the previous section. This will address models for channel gain and RMS delay spread. These models will be general and require only knowledge of the distance separating the transmitter and receiver. We first start with fitting different probability distribution functions to the obtained histograms and will see if the quality of the fitting is acceptable or not. To do this, the Chi-Squared (χ^2) test is used, which shows how well the selected distributions fits to collected data [39].

3.4.1 χ^2 Goodness of Fit Test

The χ^2-test is used to test the hypothesis that a function $F(x)$ is the distribution of the sample population $x_1, x_2, ..., x_n$. If the sample population deviates too much from $F(x)$ then we shall reject the hypothesis. The χ^2-test works best when a significant amount of sample data exists such that a histogram can be made. Once this histogram is made the data should be divided so that no bin contains fewer than 5 samples.

We will perform the χ^2-test on all groups of data collected in sections 3.2 and 3.3. For comparison, different distribution functions are considered and evaluated because of their similar shape and characteristics. Each distribution requires one or more parameters to be estimated. According to χ^2 theory [4] there are $K - r - 1$ degrees of freedom, where K is the number of bins and r is the number of unknown parameters.

Once the degrees of freedom is known, a significance level, α, is chosen on the order of 5% to 0.5%. The significance level represents the degree of certainty we have that $F(x)$ is the distribution. The higher α we require, the less deviation is allowed. A table for the χ^2 test contains the expected deviation or critical value based on α and the degrees of freedom. One such table can be seen in [40].

The more degrees of freedom one has, the higher the deviation is allowed. If the calculated deviation is less than the value from the chart, the hypothesis that $F(x)$ could be the distribution for the sample population. The sample deviation is calculated according to

$$\chi^2 = \sum_{j=1}^{K} \frac{(b_j - e_j)^2}{e_j} \tag{22}$$

where b_j is the number of sample values in an interval I_j and

$$e_j = np_j \tag{23}$$

where n is the number of samples in the population and P_j is the probability that the random variable assumes any value in interval I_j.

3.4.2 Channel Gain Distributions

Figure 33 shows seven distributions fitted to the channel gain histogram for case of $D_{tr} = 2$ m. Distributions are ranked according to the χ^2-test results. As can be seen from this figure, there is not much difference between the goodness of fitting for the first three distributions. Lognormal and normal distributions also show similar results. Estimated parameters of all these distributions are summarized in Table 4. Details and results of χ^2-test for each probability distribution function are provided in Table 5-11. According to these results, Beta, Gamma (3P) and Lognormal (3P) distributions can be considered as reasonable distributions to fit the channel gain data if significance level is less than 0.2, and the remaining distributions are rejected by χ^2-test for all significance levels.

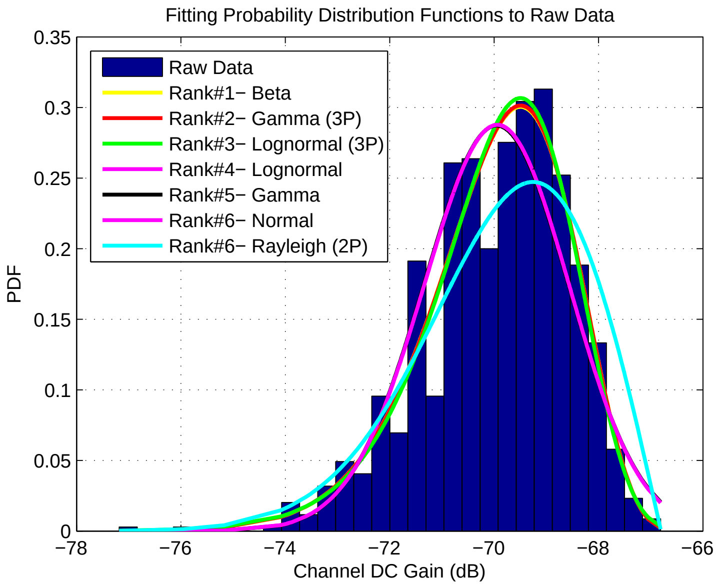

Figure 33: Distribution curves plotted atop histogram of channel gain data for $D_{tr} = 2$ m

Table 4: Estimated parameters of distributions

Rank	**Distribution**	**Parameters**
1	Beta	$\alpha_1 = 7.6659533539448$ $\alpha_2 = 251.528538128031$ a = 66.0502412611958 b = 198.898229358253
2	Gamma (3P*)	$\alpha = 8.21809467031087$ $\beta = 0.487061182664746$ $\gamma = 65.9766473663695$
3	Lognormal (3P)	$\sigma = 0.244712228021445$ $\mu = 1.70027039925595$ $\gamma = 64.3378367695469$
4	Lognormal	$\sigma = 0.019812667065969$ $\mu = 4.24800329301922$
5	Gamma	$\alpha = 2513.14556538295$ $\beta = 0.027845327867307$
6	Normal	$\sigma = 1.39592201991905$ $\mu = 69.9793622463576$
7	Rayleigh (2P)	$\sigma = 2.45324615257952$ $\gamma = 66.8028574551343$

* 3P accounts for a distribution with three parameters.

Table 5: Goodness of fit results for Beta distribution

Deg. of freedom Expected deviation Rank	9 13.5636704299299 1				
α	0.2	0.1	0.05	0.02	0.01
Sample Deviation	12.2421454698471	14.6836565732598	16.9189776046204	19.6790160948545	21.6659943334619
Reject?	Yes	No	No	No	No

Table 6: Goodness of fit results for Gamma (3P) distribution

Deg. of freedom Expected deviation Rank	9 13.9862662146283 2				
α	0.2	0.1	0.05	0.02	0.01
Sample Deviation	12.2421454698471	14.6836565732598	16.9189776046204	19.6790160948545	21.6659943334619
Reject?	Yes	No	No	No	No

Table 7: Goodness of fit results for Lognormal (3P) distribution

Deg. of freedom Expected deviation Rank	9 14.6133066669905 3				
α	0.2	0.1	0.05	0.02	0.01
Sample Deviation	12.2421454698471	14.6836565732598	16.9189776046204	19.6790160948545	21.6659943334619
Reject?	Yes	No	No	No	No

Table 8: Goodness of fit results for Lognormal distribution

Deg. of freedom Expected deviation Rank	9 30.7135015190525 4				
α	0.2	0.1	0.05	0.02	0.01
Sample Deviation	12.2421454698471	14.6836565732598	16.9189776046204	19.6790160948545	21.6659943334619
Reject?	Yes	Yes	Yes	Yes	Yes

Table 9: Goodness of fit results for Gamma distribution

Deg. of freedom Expected deviation Rank	9 33.4584833175603 5				
α	0.2	0.1	0.05	0.02	0.01
Sample Deviation	12.2421454698471	14.6836565732598	16.9189776046204	19.6790160948545	21.6659943334619
Reject?	Yes	Yes	Yes	Yes	Yes

Table 10: Goodness of fit results for Normal distribution

Deg. of freedom Expected deviation Rank	9 34.6750400352363 6				
α	0.2	0.1	0.05	0.02	0.01
Sample Deviation	12.2421454698471	14.6836565732598	16.9189776046204	19.6790160948545	21.6659943334619
Reject?	Yes	Yes	Yes	Yes	Yes

Table 11: Goodness of fit results for Rayleigh (2P) distribution

Deg. of freedom Expected deviation Rank	9 60.5108366969795 7				
α	0.2	0.1	0.05	0.02	0.01
Sample Deviation	12.2421454698471	14.6836565732598	16.9189776046204	19.6790160948545	21.6659943334619
Reject?	Yes	Yes	Yes	Yes	Yes

3.4.3 Delay Spread Distributions

Figure 34 shows seven distributions fitted to the RMS delay spread histogram for case of $D_{tr} = 2$ m. Distributions are ranked according to the χ^2-test results. As can be seen from this figure, the first three distributions (Lognormal (3P), Gamma (3P) and Normal) show similar goodness of fitting. Estimated parameters of all these distributions are summarized in Table 12. Details and results of χ^2-test for each probability distribution function are provided in Table 13-19. According to these results, Lognormal (3P), Gamma (3P), Normal and Beta distributions can be considered as reasonable distributions to fit the delay spread data for any significance level.

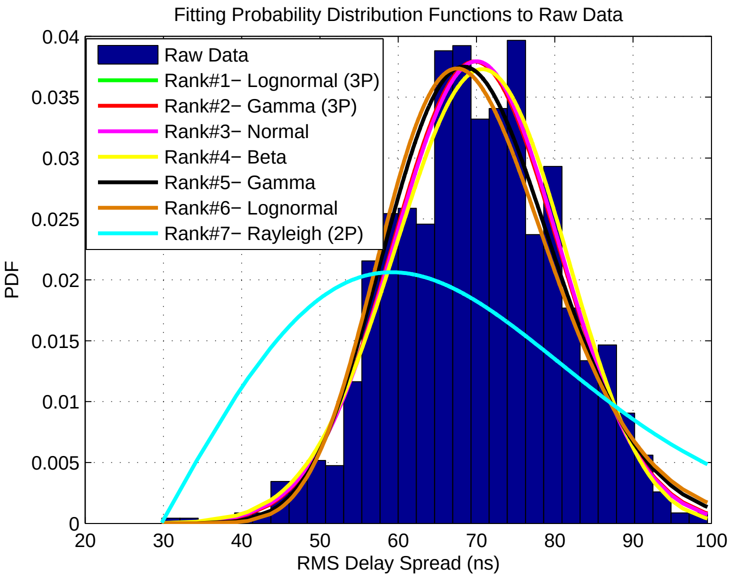

Figure 34: Distribution curves plotted atop histogram of delay spread data for $D_{tr} = 2$ m

Table 12: Estimated parameters of distributions

Rank	**Distribution**	**Parameters**
1	Lognormal (3P)	$\sigma = 0.008878975923262$ $\mu = 7.0747960193264$ $\gamma = -1111.85171367738$
2	Gamma (3P)	$\alpha = 2207.97765662557$ $\beta = 0.224046828333642$ $\gamma = -424.67895474742$
3	Normal	$\sigma = 10.5143454915999$ $\mu = 69.9988703593051$
4	Beta	$\alpha_1 = 23.1729367878888$ $\alpha_2 = 15.4946722496922$ $a = -10.9732438140731$ $b = 124.142827492938$
5	Gamma	$\alpha = 44.32181901608$ $\beta = 1.57933207420728$
6	Lognormal	$\sigma = 0.156213794008141$ $\mu = 4.23665583797242$
7	Rayleigh (2P)	$\sigma = 29.4120040908701$ $\gamma = 29.7534851450862$

Table 13: Goodness of fit results for Lognormal (3P) distribution

Deg. of freedom	9				
Expected deviation	9.24747243078086				
Rank	1				
α	0.2	0.1	0.05	0.02	0.01
Sample Deviation	12.2421454698471	14.6836565732598	16.9189776046204	19.6790160948545	21.6659943334619
Reject?	No	No	No	No	No

Table 14: Goodness of fit results for Gamma (3P) distribution

Deg. of freedom	9				
Expected deviation	9.4736376017553				
Rank	2				
α	0.2	0.1	0.05	0.02	0.01
Sample Deviation	12.2421454698471	14.6836565732598	16.9189776046204	19.6790160948545	21.6659943334619
Reject?	No	No	No	No	No

Table 15: Goodness of fit results for Normal distribution

Deg. of freedom	9				
Expected deviation	9.98477928091592				
Rank	3				
α	0.2	0.1	0.05	0.02	0.01
Sample Deviation	12.2421454698471	14.6836565732598	16.9189776046204	19.6790160948545	21.6659943334619
Reject?	No	No	No	No	No

Table 16: Goodness of fit results for Beta distribution

Deg. of freedom	9				
Expected deviation	10.6027358131699				
Rank	4				
α	0.2	0.1	0.05	0.02	0.01
Sample Deviation	12.2421454698471	14.6836565732598	16.9189776046204	19.6790160948545	21.6659943334619
Reject?	No	No	No	No	No

Table 17: Goodness of fit results for Gamma distribution

Deg. of freedom	9				
Expected deviation	12.5599180962836				
Rank	5				
α	0.2	0.1	0.05	0.02	0.01
Sample Deviation	12.2421454698471	14.6836565732598	16.9189776046204	19.6790160948545	21.6659943334619
Reject?	Yes	No	No	No	No

Table 18: Goodness of fit results for Lognormal distribution

Deg. of freedom	9				
Expected deviation	15.7859398988489				
Rank	6				
α	0.2	0.1	0.05	0.02	0.01
Sample Deviation	12.2421454698471	14.6836565732598	16.9189776046204	19.6790160948545	21.6659943334619
Reject?	Yes	Yes	No	No	No

Table 19: Goodness of fit results for Rayleigh (2P) distribution

Deg. of freedom	8				
Expected deviation	525.768774383149				
Rank	7				
α	0.2	0.1	0.05	0.02	0.01
Sample Deviation	11.0300914303031	13.3615661365117	15.5073130558655	18.1682307648264	20.0902350296632
Reject?	Yes	Yes	Yes	Yes	Yes

CHAPTER IV

PERFORMANCE EVALUATION OF IEEE 802.15.7 STANDARD

The Institute of Electrical and Electronics Engineers (IEEE) has introduced the IEEE Standard 802.15.7 [41] which was approved in June 2011. This standard defines a physical layer (PHY) and medium access control (MAC) layer for VLC and promises data rates sufficient to support audio and video multimedia services. An overview of this standard can be found in tutorial type papers [[42, 43]. A real-time VLC system prototype is further introduced in [44] and some over-the-air measured performance results for the physical layer type I (PHY I) of the IEEE 802.15.7 standard are presented. However, to the best of our knowledge, an extensive comparative performance evaluation of the different PHY types of the IEEE 802.15.7 standard does not yet exist in the literature.

In this chapter, we first provide a detailed description of PHY layers of IEEE 802.15.7 standard. Then we present signal and channel models and implement the IEEE 802.15.7 PHY layers I, II and III in MATLAB and provide Monte Carlo simulation results over a typical indoor VLC channel.

4.1 PHY Layer Specifications

The Physical Layer defines the electrical and physical specifications for devices. In particular, it defines the relationship between a device and a physical medium. One device transmits data to the medium, and another device receives data from medium based on the physical layer. The functions and services of the physical layer are link establishment and termination of a connection to a communications medium.

Based on the IEEE 802.15.7 standard for visible light communications, PHY layer is responsible for the following tasks [41]:

- Activation and deactivation of the VLC transceiver
- Wavelength Quality Indication (WQI) for received frames
- Channel selection
- Data transmission and reception
- Error correction
- Synchronization

4.1.1 General Characteristics

Operating Wavelength Range and Band Plan for VLC

The visible light spectrum defined in this standard covers wavelengths between 380 nm and 780 nm. A compliant device shall operate in one or several visible light wavelength bands as summarized in Table 20 [41].

Table 20: Visible light wavelength band plan

Band (nm)	Center (nm)	Spectral Width (nm)	Code
380–478	429	98	000
478–540	509	62	001
540–588	564	48	010
588–633	611	45	011
633–679	656	46	100
679–726	703	47	101
726–780	753	54	110
Reserved			111

LED manufacturers make LEDs depending on human color perception and not frequency band, so non-linear widths is needed for band plan. The VLC standard provides support for 7 bands in the visible light spectrum. The bands take into account the non-linear color sensitivity of the human eye and the corresponding spectral range of LEDs. The standard also supports use of wide bandwidth optical transmitters (such as white LEDs) that can transmit on multiple bands or have leakage in other bands using the concepts of channel aggregation and guard channels.

4.1.2 Dimming and Flicker Mitigation

The two main challenges for communication using visible light spectrum are flicker mitigation and dimming support. Flicker refers to the fluctuation of the brightness of light. Any potential flicker resulting from modulating the light sources for communication must be mitigated, because flicker can cause noticeable, negative/harmful physiological changes in humans. To avoid flicker, the changes in brightness must fall within the maximum flickering time period (MFTP). The MFTP is defined as the maximum time period over which the light intensity can change without the human eye perceiving it. While there is no widely accepted optimal flicker frequency number, a frequency greater than 200 Hz (MFTP $<$ 5 ms) is generally considered safe. Therefore, the modulation process in VLC must not introduce any noticeable flicker either during the data frame or between data frames.

Dimming support is another important consideration for VLC for power savings and energy efficiency. It is desirable to maintain communication while a user arbitrarily dims the light source. The human eye responds to low light levels by enlarging the pupil, which allows more light to enter the eye. This response results in a difference between perceived and measured levels of light. Hence, communication support needs to be provided when the light source is dimmed over a large range, typically between 0.1100 percent. VLC is being investigated by a number of universities, corporations, and organizations worldwide. However, none of them focus on flicker mitigation and dimming, which has been integrated into IEEE 802.15.7 [42].

4.1.3 Modulation

On-Off Keying

OOK modulation is the simplest modulation scheme for VLC, where the LEDs are turned on or off depending on data bits being 1 or 0. While the modulation is logically OOK, OOK “off” does not necessarily mean the light is completely turned off; rather, the intensity of the light may simply be reduced as long as one can distinguish clearly between the “on” and “off” levels.

Table 21: Definition of data mapping for OOK modulation

Logical value	Physical value	
0	Low	$0 < t < T$
1	High	$0 < t < T$

Variable Pulse Position

The use of modulation techniques such as pulse position modulation (PPM) for dimming support has been proposed for VLC. Variable pulse position modulation (VPPM) changes the duty cycle of each optical symbol to encode bits. The variable term in VPPM represents the change in the duty cycle (pulse width) in response to the requested dimming level.

Table 22: Definition of data mapping for VPPM modulation [41]

Logical value	Physical value d is the VPPM duty cycle ($0.1 < d < 0.9$)	
0	High	$0 < t < dT$
	Low	$dT < t < T$
1	Low	$0 < t < (1 - d)T$
	High	$(1 - d)T < t < T$

VPPM optical symbols are distinguished by the pulse position. As shown in Fig. 35 (a), VPPM is similar to 2-PPM when the duty cycle is 50 percent. The logic 0 and logic 1 symbols are pulse width modulated depending on the dimming duty cycle requirement. As shown in Fig. 35 (b), the pulse width ratio (b/a) of PPM can be adjusted to produce the required duty cycle for supporting dimming by pulse width modulation (PWM). Figure 36 shows an example waveform of how VPPM can attain a 75 percent dimming duty cycle requirement, where both logic 0 and logic 1 have a 75 percent pulse width [42].

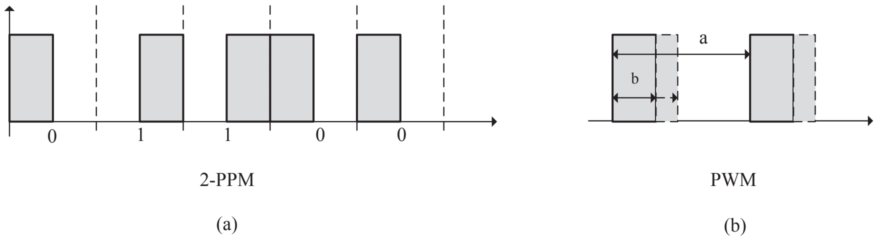

Figure 35: Basic concept of VPPM

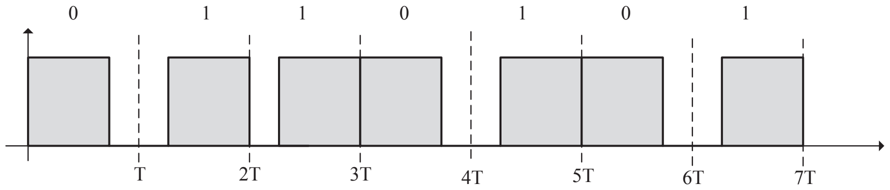

Figure 36: Waveform of VPPM signal with 75 percent pulse width

Color-Shift Keying

White LED lights are generated by using a mixture of different colors in typically two different methods. White LEDs can be generated using blue LEDs with yellow phosphor. However, yellow phosphor slows down the switching response of the white LEDs. Alternately, faster white LEDs that can be more useful for communication can be generated by simultaneously exciting red, green and blue LEDs. The use of such multi-color LEDs forms the principle behind Color Shift Keying (CSK) modulation. Color shift keying modulation is similar to frequency shift keying in that the bit patterns are encoded to color (wavelength) combinations. For example, for 4-CSK (two bits per symbol) the light source is wavelength keyed such that one of four possible wavelengths (colors) is transmitted per bit pair combination.

In order to define various colors for communication, the IEEE 802.15.7 standard breaks the spectrum into 7 color bands, according to the CIE 1931 color space standard [45], in order to provide support for multiple LED color choices for communication. Each of these bands has an assigned color code and is mapped into x and y values on the xy color coordinates. The color codes and xy coordinate values for each band are shown in Table 23.

Table 23: Color bands and xy color coordinates [41]

Band (nm)	Code	Center (nm)	(x, y)
380–478	000	429	(0.169, 0.007)
478–540	001	509	(0.011, 0.733)
540–588	010	564	(0.402, 0.597)
588–633	011	611	(0.669, 0.331)
633–679	100	656	(0.729, 0.271)
679–726	101	703	(0.734, 0.265)
726–780	110	753	(0.741, 0.268)

The CSK signal is generated by using three color light sources out of the seven color bands. The three vertices of the CSK constellation triangle are decided by the center wavelength of the three color bands on xy color coordinates. Certain combinations that cannot make a triangle on the xy color coordinates are excluded, such as (110-101-100) or (100-011-010). Table 23 shows valid color band combinations that can make triangles for CSK constellations [41].

Table 24 shows the xy color coordinates values assuming the optical source is chosen with the spectral peak occurring at the center of each of the seven color bands. It is possible that some of the optical sources would have a spectral peak at a different frequency than the center of the band plan. It is also possible that the spectrum of the optical source would be distributed among over multiple frequency bands. Implementers of CSK systems can select the color band based on the center wave length of the actual optical source.

Table 24: Valid color band combinations for CSK [41]

	Band *i*	**Band *j***	**Band *k***
1	110	010	000
2	110	001	000
3	101	010	000
4	101	001	000
5	100	010	000
6	100	001	000
7	011	010	000
8	011	001	000
9	010	001	000

CSK has the following advantages:

- The final output color (e.g., white) is guaranteed by the color coordinates. CSK channels are determined by mixed colors that are allocated in the color coordinates plane [42].
- The total power of all CSK light sources is constant, although each light source may have a different instantaneous output power. CSK dimming ensures that the average optical power from the light sources is kept constant and maintains the requisite intensity of the center color of the color constellation. Thus, there is no flicker issue associated with CSK due to amplitude variations. CSK dimming employs amplitude dimming and controls the brightness by changing the current driving the light source. However, care needs to be observed during CSK dimming to avoid unexpected color shift in the light source [42].
- CSK supports amplitude changes with digital-to-analog (D/A) converters (higher complexity), thus allowing higher order modulation support to provide higher data rates at a lower optical clock frequency. PHY I and PHY II allow only OOK modulation, thereby limiting their data rate to 1 b/clock [42].

4-CSK constellation design

4-CSK symbol points are defined by the design rule in Fig. 37. In this figure, 4-CSK data mapping is also shown. Two bits are assigned per symbol. Points I, J and K show the center of the three color bands on xy color coordinates. S0 to S3 are four symbol points of 4-CSK. S1, S2 and S3 are three vertices of the triangle IJK. S0 is the centroid of the triangle IJK [41].

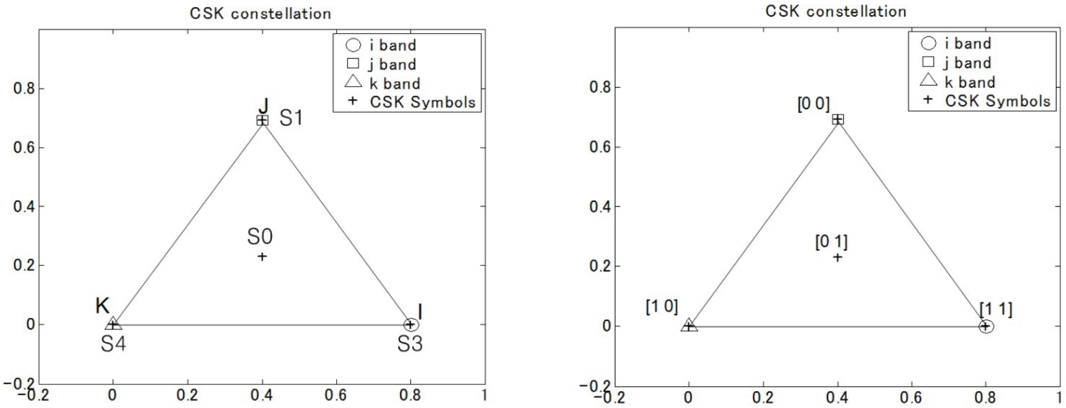

(a) constellation points

(b) data mapping

Figure 37: 4-CSK constellation and data mapping [41]

8-CSK constellation design

8-CSK symbol points are defined by the design rule in Fig. 38. In this figure, 8-CSK data mapping is also shown. Three bits are assigned per symbol. Points I, J and K show the center of the three color bands on xy color coordinates. S0 to S7 are 8 symbol points of 8-CSK. S0, S4 and S7 are three vertices of the triangle IJK. S1 and S2 are points that divide side JK and side JI in the ratio 1:2. Point b and c are midpoints of the line JI and line JK. S6 is a midpoint of the line KI. Point a is the centroid of the triangle b-S6-I. Point d is the centroid of the triangle c-K-S6. S3 is a point that divides line ab in the ratio 1:2. S5 is a point that divides line dc in the ratio 1:2 [41].

16-CSK constellation design

16-CSK symbol points are defined by the design rule in Fig. 39. In this figure, 16-CSK data mapping is also shown. Four bits are assigned per symbol. Points I, J and K

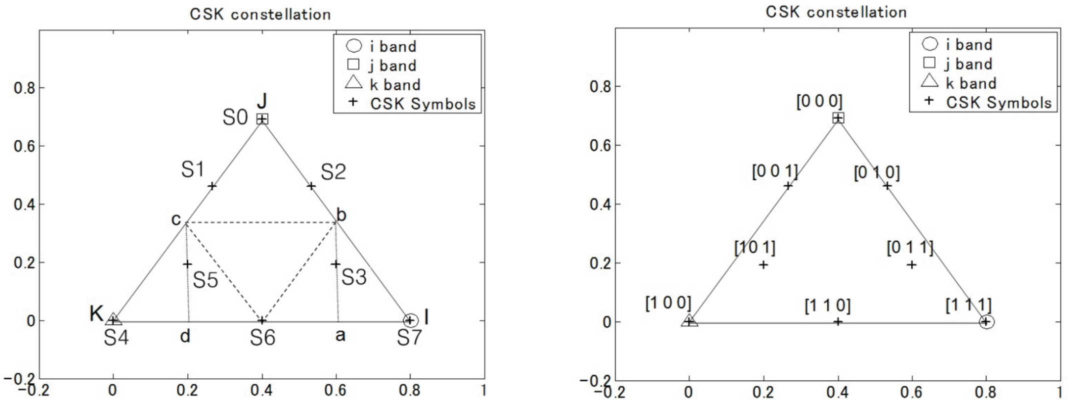

(a) constellation points (b) data mapping

Figure 38: 8-CSK constellation and data mapping [41]

show the center of the three color bands on xy color coordinates. S0 to S15 are 16 symbol points of 16-CSK. S5, S10 and S15 are three vertices of the triangle IJK. S2 and S8 are points that divide side JK in one third. S3 and S12 are points that divide side JI in one third. S11 and S14 are points that divide side KI in one third. S0 is the centroid of the triangle IJK. S1, S4, S6, S7, S9 and S13 are the centroids of each of the smaller triangles [41].

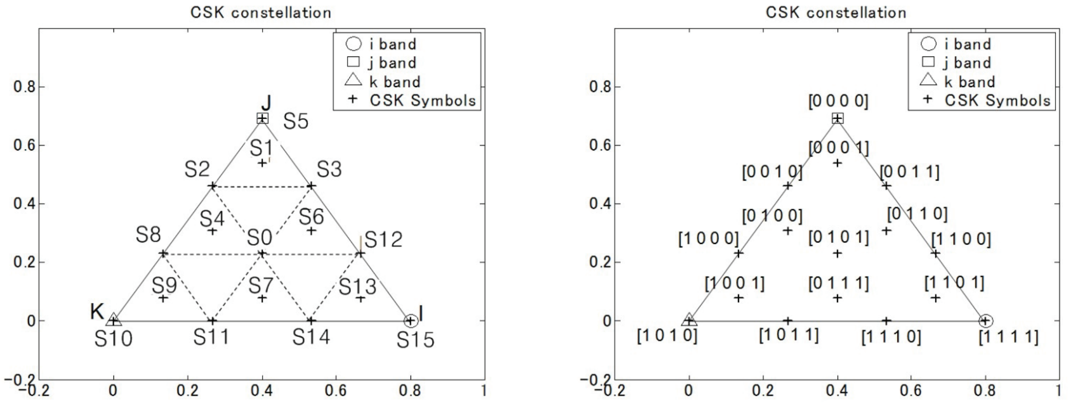

(a) constellation points (b) data mapping

Figure 39: 16-CSK constellation and data mapping [41]

Table 25 shows color band combination and the xy coordinate values when color codes (110, 010, 000) are used.

Table 25: Color band combination example for (110, 010, 000) [41]

Color band combination		**x-y coordinates values of symbols**		
Color codes	Center of band (x,y)	4-CSK [data] – (x_p,y_p)	8-CSK [data] – (x_p,y_p)	16-CSK [data] –(x_p,y_p)
110	(0.730 0.270)	[0 0] - (0.190 0.780)	[0 0 0] - (0.190 0.780)	[0 0 0 0] - (0.190 0.780)
010	(0.190 0.780)	[0 1] - (0.367 0.353)	[0 0 1] - (0.187 0.523)	[0 0 0 1] - (0.249 0.638)
000	(0.180 0.010)	[1 0] - (0.180 0.010)	[0 1 0] - (0.370 0.610)	[0 0 1 0] - (0.187 0.523)
		[1 1] - (0.730 0.270)	[0 1 1] - (0.519 0.383)	[0 0 1 1] - (0.370 0.610)
			[1 0 0] - (0.180 0.010)	[0 1 0 0] - (0.246 0.381)
			[1 0 1] - (0.244 0.253)	[0 1 0 1] - (0.367 0.353)
			[1 1 0] - (0.455 0.140)	[0 1 1 0] - (0.429 0.468)
			[1 1 1] - (0.730 0.270)	[0 1 1 1] - (0.426 0.211)
				[1 0 0 0] - (0.183 0.267)
				[1 0 0 1] - (0.242 0.124)
				[1 0 1 0] - (0.180 0.010)
				[1 0 1 1] - (0.363 0.097)
				[1 1 0 0] - (0.550 0.440)
				[1 1 0 1] - (0.609 0.298)
				[1 1 1 0] - (0.547 0.183)
				[1 1 1 1] - (0.730 0.270)

CSK color mapping

Figure 40 shows the CIE1931 xy color coordinates [45] with the color mapping for 4-CSK. In this case, four color points are defined.

In CSK modulation, binary data (zeros and ones) are transformed into xy values, according to a mapping rule on the xy color coordinates by the color coding block. The points on the xy coordinate are then converted to (R, G, B) values which represent the intensity of the red, green and blue light emitted from the RGB LED respectively. According to Fig. 40, the points (x_i, y_i), (x_j, y_j) and (x_k, y_k) show the xy coordinates of three light sources. The point (x_p, y_p) shows one allocated color point in 4-CSK. The color point (x_p, y_p) can be represented by the normalized intensity of the three light sources P_i, P_j and P_k. The relationship between the coordinates and the intensities

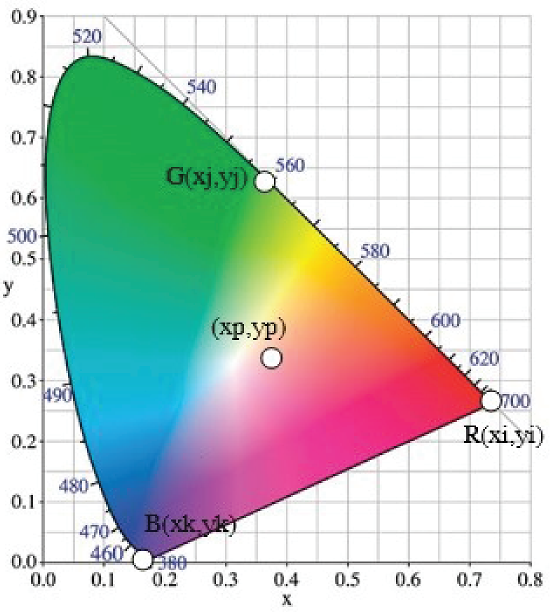

Figure 40: CIE 1931 xy color coordinates

is given by the following set of equations [41]

$$\begin{aligned} x_p &= P_i x_i + P_j x_j + P_k x_k \\ y_p &= P_i y_i + P_j y_j + P_k y_k \\ P_i &+ P_j + P_k = 1 \end{aligned} \tag{24}$$

At the receiver side, xy values are calculated from the received intensities of three colors, and then they are decoded into the received data.

4.1.4 Forward Error Correction Coding

IEEE 802.15.7 supports various forward error correcting (FEC) schemes to work reasonably well in the presence of hard decisions that would be generated by the clock and data recovery (CDR). The channel codes support both long and short data frames for high-data-rate indoor and low-data-rate outdoor applications. For outdoor applications, stronger codes using concatenated Reed-Solomon (RS) and convolutional codes (CC) are developed to overcome the additional path loss due to longer distance and potential interference introduced by optical noise sources such as daylight and fluorescent lighting. RS and CC are preferred over advanced coding schemes such as low density parity check (LDPC) codes in order to support short data frames, hard decision decoding, low complexity, and their ability to interface well with run length limited (RLL) line codes. For indoor applications, where the coding requirements are less stringent for short distances, RS codes are used for FEC since they are better suited to high-data-rate implementations. RS codes also interface well in conjunction with the RLL line codes, where the errors detected from the RLL line code at the receiver could be marked as erasures to the RS decoder, providing performance improvements of around 1 dB [43].

Reed-Solomon Coding

In coding theory, RS codes are non-binary cyclic error-correcting codes which provide a systematic way of building codes that could detect and correct multiple random symbol errors. In RS coding, source symbols are viewed as coefficients of a polynomial over a finite field called Galois Field (GF).

For the PHY I outer FEC, systematic RS codes are used with $GF(2^4)$, generated by the polynomial $x^4 + x + 1$. The generators for the RS(n, k) codes for PHY I are given in Table 26, where α is a primitive element in $GF(2^4)$ [41].

Table 26: Generator polynomials [41]

$(\boldsymbol{n,k})$	$g(x)$
(15,11)	$x^4 + \alpha^{13}x^3 + \alpha^6x^2 + \alpha^3x + \alpha^{10}$
(15,7)	$x^8 + \alpha^{14}x^7 + \alpha^2x^6 + \alpha^4x^5$ $+ \alpha^2x^4 + \alpha^{13}x^3 + \alpha^5x^2 + \alpha^{11}x^1 + \alpha^6$
(15,4)	$x^{11} + \alpha^9x^{10} + \alpha^8x^9 + \alpha^4x^8 + \alpha^9x^7 + \alpha^{13}x^6$ $+ \alpha^4x^5 + \alpha^{12}x^4 + \alpha^4x^3 + \alpha^5x^2 + \alpha^3x + \alpha^6$
(15,2)	$x^{13} + \alpha^3x^{12} + \alpha^8x^{11} + \alpha^9x^{10} + \alpha^2x^9 + \alpha^4x^8 + \alpha^{14}x^7$ $+ \alpha^6x^6 + \alpha^{10}x^5 + \alpha^7x^4 + \alpha^{13}x^3 + \alpha^{11}x^2 + \alpha^5x + \alpha$

For PHY II, a systematic RS code operating on $GF(2^8)$ shall be used to correct errors and increase the system reliability. The RS code is defined over $GF(2^8)$ with a primitive polynomial $x^8 + x^4 + x^3 + x^2 + 1$. The generator for the RS(160, 128) code and the RS(64, 32) code is given by

$$\begin{aligned} g(x) = {} & x^{32} + \alpha^{11}x^{31} + \alpha^{8}x^{30} + \alpha^{109}x^{29} + \alpha^{194}x^{28} + \alpha^{254}x^{27} + \alpha^{173}x^{26} \\ & + \alpha^{11}x^{25} + \alpha^{75}x^{24} + \alpha^{218}x^{23} + \alpha^{148}x^{23} + \alpha^{149}x^{21} + \alpha^{44}x^{20} + \alpha^{0}x^{19} \\ & + \alpha^{137}x^{18} + \alpha^{104}x^{17} + \alpha^{43}x^{16} + \alpha^{137}x^{15} + \alpha^{203}x^{14} + \alpha^{99}x^{13} + \alpha^{176}x^{12} \\ & + \alpha^{59}x^{11} + \alpha^{91}x^{10} + \alpha^{194}x^{9} + \alpha^{84}x^{8} + \alpha^{53}x^{7} + \alpha^{248}x^{6} + \alpha^{107}x^{5} \\ & + \alpha^{80}x^{4} + \alpha^{28}x^{3} + \alpha^{215}x^{2} + \alpha^{251}x + \alpha^{18} \end{aligned} \tag{25}$$

where α is a primitive element in $GF(2^8)$.

The Reed-Solomon code may be shortened for the last block if it does not meet the block size requirements. No zero padding is required for the RS code. A shortened RS code is used for frame sizes not matching code word boundaries via the following operation to minimize padding overhead. Starting with a RS(n, k) code, one can get an RS$(n - s, k - s)$ shortened code as follows [41]:

1. Pad the $k - s$ RS symbols with s zero RS symbols.
2. Encode using RS(n, k) encoder.
3. Delete the padded zeros (do not transmit them).
4. At the decoder, add the zeros, then decode.

Convolutional Coding

Rate-1/3 Code

The inner code is a based on a rate-1/3 mother convolutional code of constraint length seven ($K = 7$) with generator polynomial $g_0 = 1338$; $g_1 = 1718$; $g_2 = 1658$, as shown in Fig. 41. Six tail bits of zeros shall be added at the end of the encoding in order to terminate the convolutional encoder to an all zeros state. The tail bit of zeros shall be applied to both the header and the payload when the inner convolutional code is used [41].

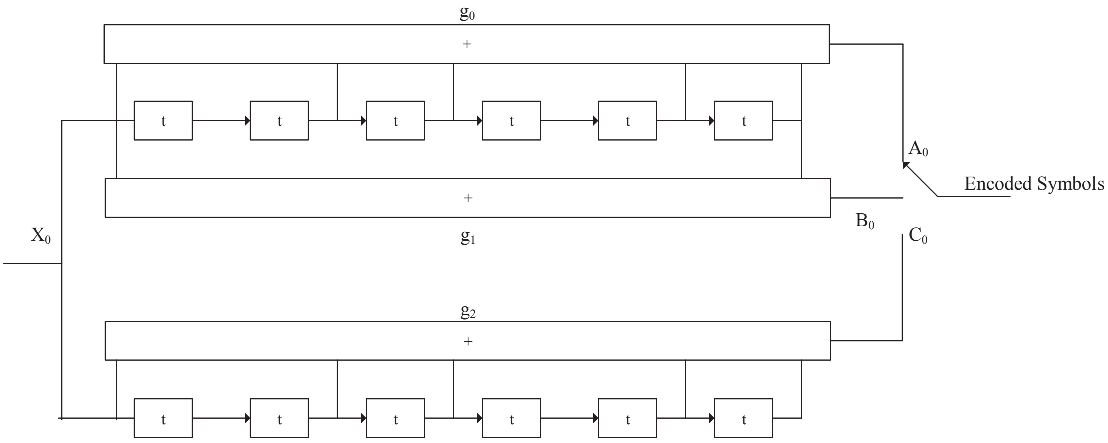

Figure 41: Rate-1/3 mother convolutional code with constraint length 7 [41]

Rate-1/4 Code

The rate-1/4 code is obtained by puncturing the rate-1/3 mother code to a rate-1/2 code, as shown in Fig. 42, and then using a simple repetition code as shown in Fig. 43.

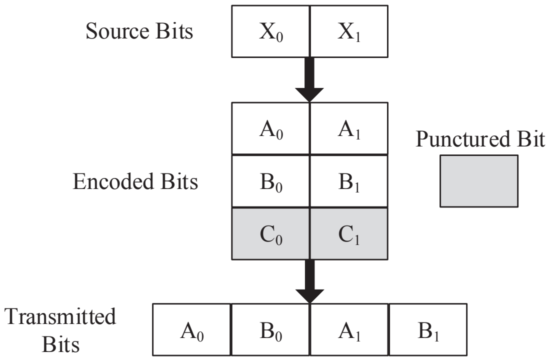

Figure 42: Puncturing pattern to obtain rate-1/2 code [41]

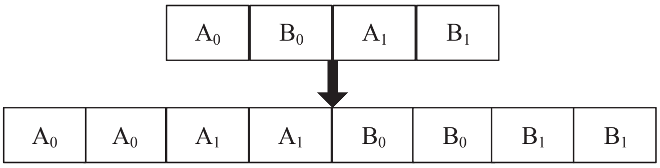

Figure 43: Repetition pattern used to obtain the effective rate-1/4 code [41]

Rate-2/3 Code

The rate-2/3 code is obtained by puncturing the rate-1/3 mother code, as in Fig. 44.

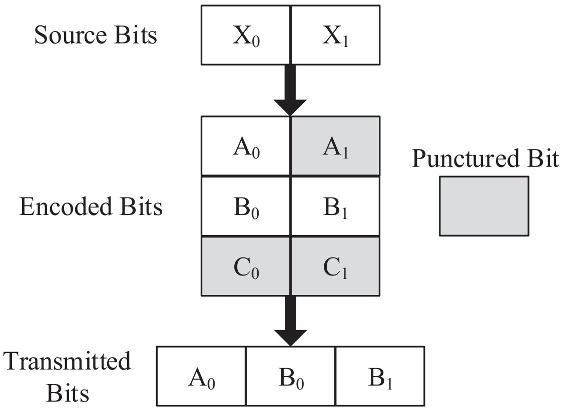

Figure 44: Puncturing pattern to obtain rate-2/3 code [41]

4.1.5 Interleaving

For PHY I, an interleaver between the RS code and the CC code provides an additional 1 dB of performance improvement. A block interleaver is used as an interleaver between the inner convolutional code and the outer RS code as shown in Fig. 45.

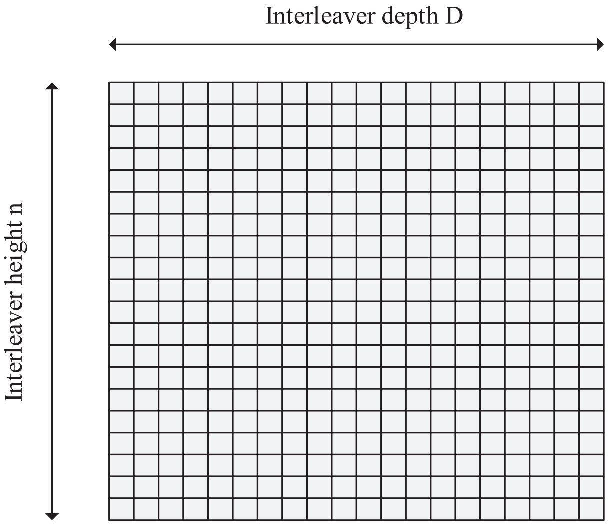

Figure 45: Interleaver for PHY I [41]

The interleaver is of a fixed height n but has a flexible depth D, dependent on the frame size. The flexible depth of the interleaver and the puncturing block after the interleaver is used to minimize padding overhead [41]. Table 27 introduces the parameters used to describe the interleaver.

Table 27: Parameters of interleaver [41]

Parameter	Description
n	RS codeword length
k	Number of information data symbols in a RS codeword
q	Number of elements in the Galois field: GF(q)
L_{frame}	Input frame size in bytes
S_{frame}	Number of symbols at the input of the RS encoder
S	Number of symbols from the output of the shortened RS encoder
S_{block}	The size of the interleaver used
D	The interleaving depth
i	Ordered indices take the values 0, 1, …, S_{block}–1
$l(i)$	Interleaved indices
p	Number of zero RS symbols
t	Ordered indices take the values 0, 1, …, p
$z(t)$	Locations of the bits to be punctured at the output of the interleaver before transmission

The interleaver and the locations to be punctured are described by the equations shown below [41]

$$\begin{aligned}
&S_{frame} = \left\lceil \frac{L_{frame} \times 8}{\log_2(q)} \right\rceil \\
&S = n \times \left\lceil \frac{S_{frame}}{k} \right\rceil - (k - (S_{frame} \bmod k)) \\
&D = \left\lceil \frac{S}{n} \right\rceil \\
&S_{block} = n \times D \\
&p = n - (S \bmod n) \\
&l(i) = (i \bmod D) \times n + \left\lfloor \frac{i}{D} \right\rfloor; \text{ for } i = 0,1,\ldots,(S_{block} - 1) \\
&z(t) = (n - p + 1) \times D + t \times D - 1; \text{ for } t = 0,1,\ldots,p - 1
\end{aligned} \tag{26}$$

The length of the frame is communicated to the receiver in the header so that the receiver can adaptively adjust the interleaver based on the frame sizes. When the data rates corresponding to transmissions using the concatenated codes are used, the header shall also be interleaved according to procedure shown in above equations.

Since the length of the header is fixed, the receiver can deinterleave the header without explicit transmission of the header length.

4.1.6 Line Coding

RLL line codes are used to avoid long runs of 1s and 0s that could potentially cause flicker and clock and data recovery (CDR) detection problems. RLL line codes take in random data symbols at input and guarantee DC balance with equal 1s and 0s at the output for every symbol. Various RLL line codes such as Manchester, 4B6B, and 8B10B are defined in the standard, and provide tradeoffs between coding overhead and ease of implementation.

Manchester Coding

According to IEEE 802.15.7 standard, all OOK PHY I modes shall use Manchester DC balancing encoding. The Manchester code expands each bit into an encoded 2-bit symbol as shown in Table 28 [41].

Table 28: Manchester Encoding

Bit	Manchester Symbol
0	01
1	10

Run Length Limited Coding

4B6B RLL Coding

According to IEEE 802.15.7 standard, all VPPM PHY I and II modes shall use 4B6B encoding. The 4B6B expands 4-bit to 6-bit encoded symbols with DC balance. The counts of 1 and 0 in every VPPM encoded symbol is always equal to 3. Table 29 defines the 4B6B code.

The features of the 4B6B code are as follows [41]

- Always 50% duty cycle during one encoded symbol
- DC balanced run length limiting code

- Error detection capability
- Run length is limited to four
- Allows reasonable clock recovery

Table 29: Mapping input 4B to output 6B [41]

Hex	4B (input)	6B (output)
0	0000	001110
1	0001	001101
2	0010	010011
3	0011	010110
4	0100	010101
5	0101	100011
6	0110	100110
7	0111	100101
8	1000	011001
9	1001	011010
A	1010	011100
B	1011	110001
C	1100	110010
D	1101	101001
E	1110	101010
F	1111	101100

8B10B RLL Coding

According to IEEE 802.15.7 standard, all OOK PHY II modes shall use 8B10B encoding as specified in ANSI/INCITS 373 [46]. The 8B10B line code converts 8-bit to 10-bit. To construct an 8B10B code, we can compose the code from compatible but separate 5B6B and 3B4B codes. The original 8 bits data is separated into two parts: first 3 bits and last 5 bits. The first 3 bits are encoded using 3B4B RLL encoding scheme and the last 5 bits are encoded by 5B6B RLL encoding scheme to the output bits, as shown in Fig. 47.

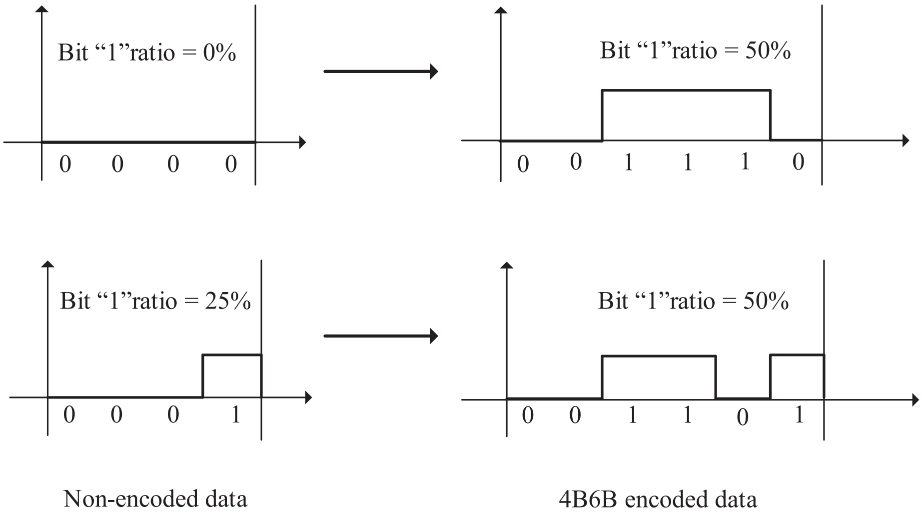

Figure 46: comparison between non-encoded and 4B6B encoded symbols

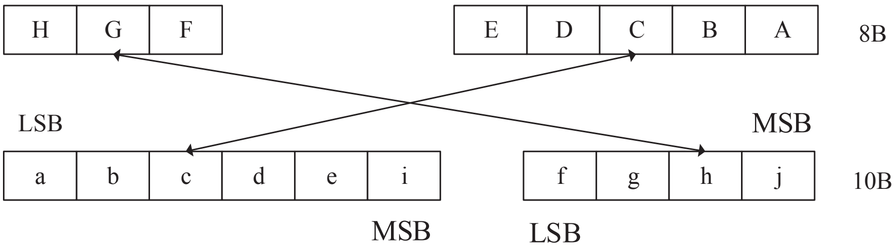

Figure 47: 8B10B encoding structure

More details about 8B10B can be found at [46]. The features of the 4B6B code are as follows [41]:

- DC balanced line code
- Error detection capability
- Run length is limited to five
- Allows reasonable clock recovery

4.1.7 Scrambling

A scrambler shall be used to ensure pseudo-random data for the PHY III [41]. The scrambler shall be applied to the entire PHY service data unit (PSDU). In addition, the scrambler shall be initialized to a seed value dependent on the topology dependent pattern at the beginning of the PSDU. The polynomial generator, $g(D)$, for the pseudo-random binary sequence (PRBS) generator shall be: $g(D) = 1 + D^{14} + D^{15}$, where D is a single bit delay element. Using this generator polynomial, the corresponding PRBS, $x[n]$, is generated as

$$x[n] = x[n-14] \oplus x[n-15], \quad n = 1,2,3,... \tag{27}$$

where "$\oplus$" denotes modulo-2 addition. The following sequence defines the initialization vector, x_{int}, which is specified by the parameter "seed value" in Table 30.

$$x_{int} = x[x_i[-1]\, x_i[-2] ... x_i[-14]\, x_i[-15]] \tag{28}$$

where $x_i[-k]$ represents the binary initial value at the output of the kth delay element. The scrambled data bits, $v[m]$, are defined in Fig. 48 and shall be calculated as

$$v[m] = s[m] \oplus x[m], \quad m = 0,1,2,... \tag{29}$$

where $s[m]$ represents the non-scrambled data bits. The side-stream de-scrambler at the receiver shall be initialized with the same initialization vector, x_{int}, used in the transmitter scrambler. The initialization vector is determined from the topology dependent pattern (TDP).

Table 30: Scrambler seed selection [41]

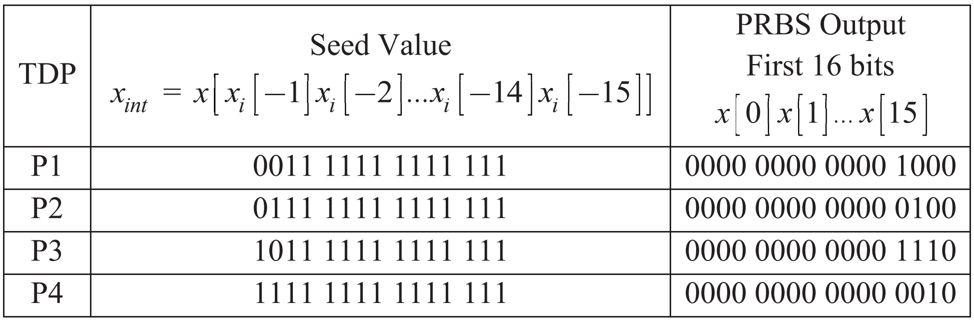

TDP	Seed Value $x_{int} = x[x_i[-1]x_i[-2]...x_i[-14]x_i[-15]]$	PRBS Output First 16 bits $x[0]x[1]...x[15]$
P1	0011 1111 1111 111	0000 0000 0000 1000
P2	0111 1111 1111 111	0000 0000 0000 0100
P3	1011 1111 1111 111	0000 0000 0000 1110
P4	1111 1111 1111 111	0000 0000 0000 0010

The 15-bit initialization vector or seed value shall correspond to the seed identifier as defined in Table 30, corresponding to the TDP pattern. The seed values shall be incremented in a roll-over fashion for each frame sent by the PHY. For example, if

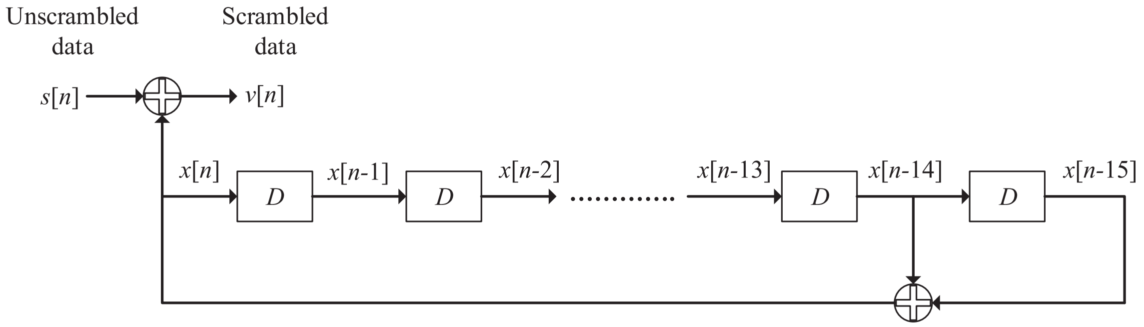

Figure 48: Scrambler block diagram [41]

the seed value used is the seed corresponding to P3 in the first frame, the seed value corresponding to P4 is used in the second frame, seed value corresponding to P1 is used in the third frame and so on. All consecutive frames, including retransmissions, shall be sent with a different initial seed value.

4.2 System Models

The IEEE 802.15.7 standard [41] supports three PHY types, namely PHY I, PHY II and PHY III. PHY I and PHY II are defined for a single light source, and support on-off keying (OOK) and variable pulse-position modulation (VPPM). PHY III is able to support multiple optical sources using the so called color shift keying (CSK) [41] [42]. PHY I is intended for outdoor applications with low data rates in the tens to hundreds of kb/s. To improve reliability in relatively harsh outdoor conditions, it uses concatenated encoding which involves a combination of convolutional code and Reed Solomon (RS) code. PHY II is intended for indoor usage with moderate data rates on the order of tens of Mb/s. PHY III is intended for applications with multiple light sources and detectors and targets to achieve data rates on the order of the tens of Mb/s. An IEEE 802.15.7-compliant device must implement either PHY I or PHY II types. A device implementing the PHY III type shall also implement PHY II mode for coexistence. Details on the optical clock rates, data rates and error correction codes for each PHY type are illustrated in Tables 31, 32 and 33. It is noted from these tables that multiple optical rates are provided for all PHY types in order to support a broad class of LEDs for various applications. The choice of optical rate used for communication is decided by the MAC layer during device discovery [41]. In the following, each PHY type is described.

4.2.1 System Model for PHY I

The block diagram of a VLC system with PHY I type is illustrated in Fig. 49 [41]. The input bits are first fed to an (n, k) Reed Solomon (RS) encoder which encodes k-symbols codewords to messages of having n symbols each. The encoding is based on a generator polynomial in Galois Field GF(2^m) where m denotes the number of bits per symbol. The encoder output is padded with zeros to form an interleaver boundary. The padded zeros are then punctured and fed to a convolutional encoder. Next, through Run Length-Limited (RLL) encoder, data is encoded either with Manchester or 4B6B codes. The former expands each bit into an encoded 2-bit symbol and the later expands 4-bit to 6-bit encoded symbols, both with DC balance. The encoded bits are finally modulated with OOK or VPPM.

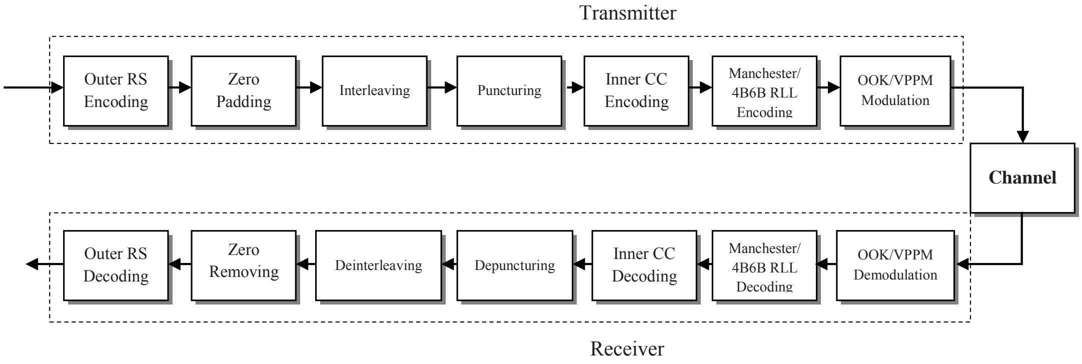

Figure 49: Block diagram of a PHY I-type VLC system

At the receiver side, after demodulating the received signal using a threshold detector, the resulting bits are first fed to the RLL decoder, then the Viterbi decoder. The output symbols of the Viterbi decoder are sent to a deinterleaver and the added zeros are removed. At the final stage, an RS decoder generates the final bit stream.

Different operating modes of PHY I are summarized in Table 31.

Table 31: PHY I operating modes [41]

Operating Mode	**Data Rate**	**Modulation**	**RLL code**	**Optical clock rate**	**FEC**	
					Outer code (RS)	**Inner code (CC)**
PHY I.a	11.67 kb/s	OOK	Manchester	200 kHz	(15,7)	1/4
PHY I.b	24.44 kb/s				(15,11)	1/3
PHY I.c	48.89 kb/s				(15,11)	2/3
PHY I.d	73.3 kb/s				(15,11)	None
PHY I.e	100 kb/s				None	None
PHY I.f	35.56 kb/s	VPPM	4B6B	400 kHz	(15,2)	None
PHY I.g	71.11 kb/s				(15,4)	None
PHY I.h	124.4 kb/s				(15,7)	None
PHY I.i	266.6 kb/s				None	None

4.2.2 System Model for PHY II

The block diagram of a VLC system with PHY II type is provided Fig. 50 [41]. The input bits are first fed to an (n, k) RS encoder. The RS encoded output is then sent to an RLL encoder which uses 4B6B or 8B10B encoding for OOK and VPPM modes, respectively. At the receiver side, after demodulating the received signal, symbols are decoded first by RLL and then by the RS decoder. Different operating modes in PHY II are summarized in Table 32.

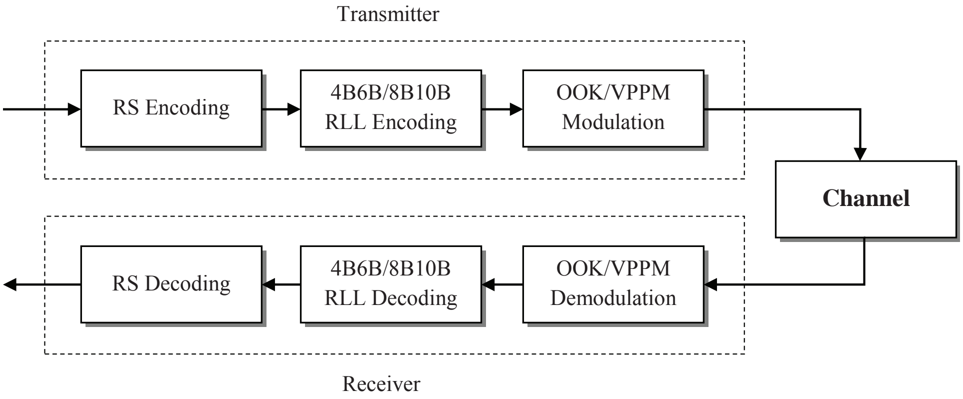

Figure 50: Block diagram of a PHY II-type VLC system

Table 32: PHY II operating modes [41]

Operating Mode	Data rate	Modulation	RLL code	Optical clock rate	FEC
PHY II.a	1.25 (Mb/s)	VPPM	4B6B	3.75 MHz	RS(64,32)
PHY II.b	2 (Mb/s)				RS(160,128)
PHY II.c	2.5 (Mb/s)			7.5 MHz	RS(64,32)
PHY II.d	4 (Mb/s)				RS(160,128)
PHY II.e	5 (Mb/s)				None
PHY II.f	6 (Mb/s)	OOK	8B10B	15 MHz	RS(64,32)
PHY II.g	9.6 (Mb/s)				RS(160,128)
PHY II.h	12 (Mb/s)			30 MHz	RS(64,32)
PHY II.i	19.2 (Mb/s)				RS(160,128)
PHY II.j	24 (Mb/s)			60 MHz	RS(64,32)
PHY II.k	38.4 (Mb/s)				RS(160,128)
PHY II.l	48 (Mb/s)			120 MHz	RS(64,32)
PHY II.m	76.8 (Mb/s)				RS(160,128)
PHY II.n	96 (Mb/s)				None

4.2.3 System Model for PHY III

The block diagram of a VLC system with PHY III type is provided in Fig. 51 [41]. At first, the input bit stream is sent to a scrambler and converted into a random bit stream avoiding long sequences of the same value in the stream. Then it passes through an RS encoder. After scrambling and channel coding, binary data is modulated using CSK.

In CSK modulation, binary data is first parsed into groups of $\log_2^M$ where M is the modulation size. Each modulation symbol is mapped into x and y values. Three of the modulation symbols are the three vertices of the constellation triangle. Other symbols are then placed within this triangle to form 4-CSK, 8-CSK or 16-CSK constellations using different constellation design methods [47, 48].

The points on the xy coordinate are then converted to (R, G, B) values which represent the intensity of the red, green and blue light emitted from the RGB LED respectively. In PHY III, the information is transmitted via these three normalized intensities [41]. At the receiver side, three photo detectors with different wavelength ranges are used to detect the intensity of each color band (intensities of red, blue and green components of the received light signal). The received intensities are then inversely mapped to points in the xy color coordinate. A minimum distance detector can then be used to find the corresponding constellation symbols and the original binary data. Different operating modes in PHY III are summarized in Table 33.

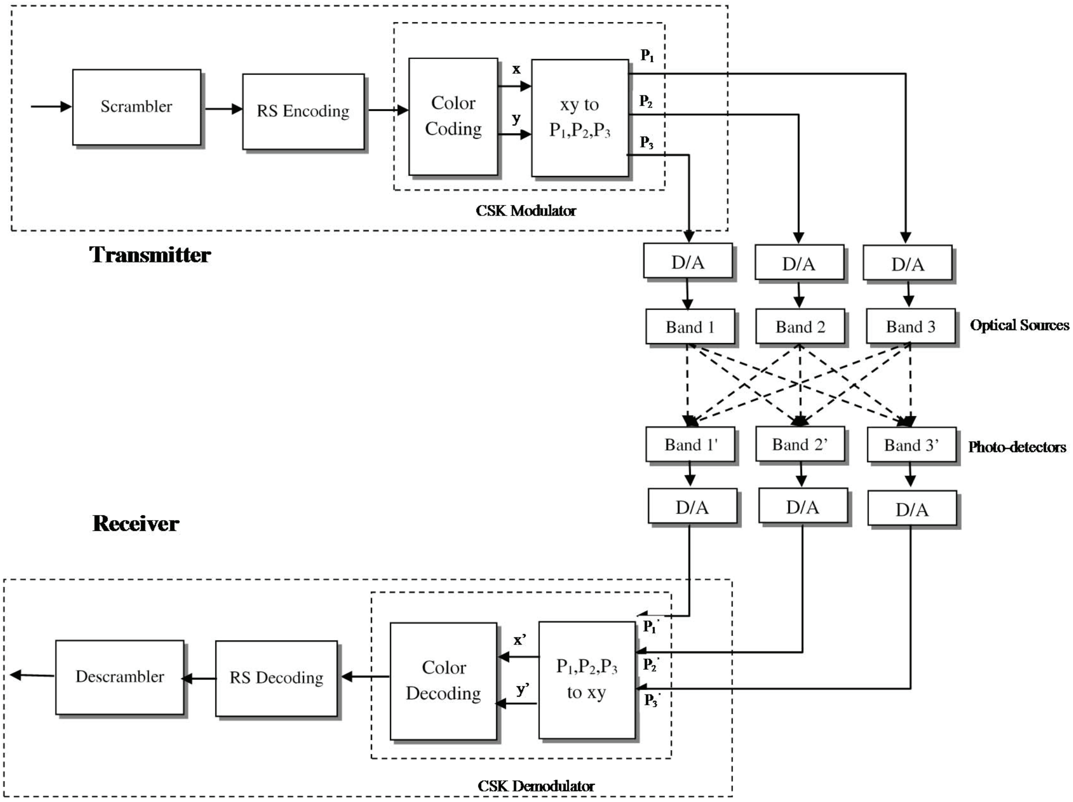

Figure 51: Block diagram of a PHY III-type VLC system

Table 33: PHY III operating modes [41]

Operating Mode	Data rate	Modulation	Optical clock rate	FEC
PHY III.a	12 Mb/s	4-CSK	12 MHz	RS(64,32)
PHY III.b	18 Mb/s	8-CSK		RS(64,32)
PHY III.c	24 Mb/s	4-CSK	24 MHz	RS(64,32)
PHY III.d	36 Mb/s	8-CSK		RS(64,32)
PHY III.e	48 Mb/s	16-CSK		RS(64,32)
PHY III.f	72 Mb/s	8-CSK		None
PHY III.g	96 Mb/s	16-CSK		None

4.3 Signal and Channel Models

The input of VLC receiver in types PHY I and II is given by

$$r(t) = x(t) * h(t) + n(t) \tag{30}$$

where "*" denotes convolution and $n(t)$ is additive white Gaussian noise (AWGN). Here, $h(t)$ is the VLC channel impulse response and $x(t)$ denotes the transmitted signal which can be expressed as

$$x(t) = \sum_{i=0}^{N-1} s(t - iT) \tag{31}$$

In (31), N is the total number of symbols in a transmission frame, T is the time duration for each transmitted symbol which is determined by data rate of the PHY operating mode and $s(t)$ is OOK or VPPM modulated signal. For binary data $b \in \{0, 1\}$, modulation signals are expressed as

$$s_{OOK}\left(t\right) = \begin{cases} 0 & ; b = 0 \\ \sqrt{T}\phi\left(t\right) & ; b = 1 \end{cases} \tag{32}$$

$$s_{VPPM}\left(t\right) = \begin{cases} \sqrt{dT}\phi_1\left(t\right) & ; b = 0 \\ \sqrt{dT}\phi_2\left(t\right) & ; b = 1 \end{cases} \tag{33}$$

where d is the dimming level ($0 \leqslant d \leqslant 1$). In (32) and (33), $\phi\left(t\right)$, $\phi_1\left(t\right)$ and $\phi_2\left(t\right)$ are the associated basis functions given by

$$\phi\left(t\right) = \begin{cases} \frac{1}{\sqrt{T}} & ; 0 \leqslant t \leqslant T \\ 0 & ; otherwise \end{cases} \tag{34}$$

$$\phi_1\left(t\right) = \begin{cases} \frac{1}{\sqrt{dT}} & ; 0 \leqslant t \leqslant dT \\ 0 & ; dT \leqslant t \leqslant T \end{cases} \tag{35}$$

$$\phi_2\left(t\right) = \begin{cases} 0 & ; 0 \leqslant t \leqslant \left(1 - d\right)T \\ \frac{1}{\sqrt{dT}} & ; \left(1 - d\right)T \leqslant t \leqslant T \end{cases} \tag{36}$$

In discrete-time notation, (30) can be rewritten as

$$r\left[k\right]=\sum_{i=0}^{N-1}s\left[i\right]h\left[k-i\right]+n\left[k\right],\quad k=0,1,... \tag{37}$$

where $r[k]$, $h[k]$ and $n[k]$, respectively, represent samples of the received signal, channel impulse response and the additive white Gaussian noise in the kth symbol interval.

The input of VLC receiver in type PHY III is given by [47]

$$\mathbf{r}\left(t\right)=\mathbf{H}\left(t\right)*\mathbf{x}\left(t\right)+\mathbf{n}\left(t\right) \tag{38}$$

where $\mathbf{x}(t)$ and $\mathbf{r}(t)$ are the transmitted and received signal vectors, respectively, and $\mathbf{H}(t)$ is the channel gain matrix. Here, the output of each photodetector is modeled as a linear combination of each of the transmit color bands, corrupted by additive white Gaussian noise. The channel gain matrix, $\mathbf{H}(t)$, can be expressed as

$$\mathbf{H}\left(t\right)=\begin{bmatrix} h_{11}\left(t\right) & h_{12}\left(t\right) & h_{13}\left(t\right)\\ h_{21}\left(t\right) & h_{22}\left(t\right) & h_{23}\left(t\right)\\ h_{31}\left(t\right) & h_{32}\left(t\right) & h_{33}\left(t\right)\end{bmatrix} \tag{39}$$

where $h_{mn}\left(t\right)$ represents the channel impulse response between the transmitter n and the receiver m for $m,n\in\{1,2,3\}$. Therefore, the signal received at the mth photodetector, $r_m\left(t\right)$, is

$$r_m\left(t\right)=\sum_{n=1}^{3}h_{mn}\left(t\right)*\ x_n\left(t\right)+n_m\left(t\right),\quad m=1,2,3 \tag{40}$$

In discrete-time notation, we have

$$r_m\left[k\right]=\sum_{n=1}^{3}\sum_{i=0}^{N-1}h_{mn}\left[k-i\right]s_n\left[i\right]+n_m\left[k\right],\quad m=1,2,3 \tag{41}$$

where the samples of s_n are normalized intensities of the transmitted light from source n.

4.4 Simulation Results

In this section, we use the method discussed in section 2.3 to obtain the CIR of a VLC channel. We consider a cubic room (5.0m×5.0m×3.0m) and assume that a white LED with a viewing angle of 110° is located at the center of the ceiling and a photodetector is located at the corner of the floor pointing upward. The corresponding coordinates for the source and the receiver are (2.5m, 2.5m, 3.0m) and (0.5m, 1.0m, 0.0m). The FOV is 90° and the area of the photodetector is 1 cm^2. For this indoor environment, the discrete version of CIR is presented in Fig. 52.

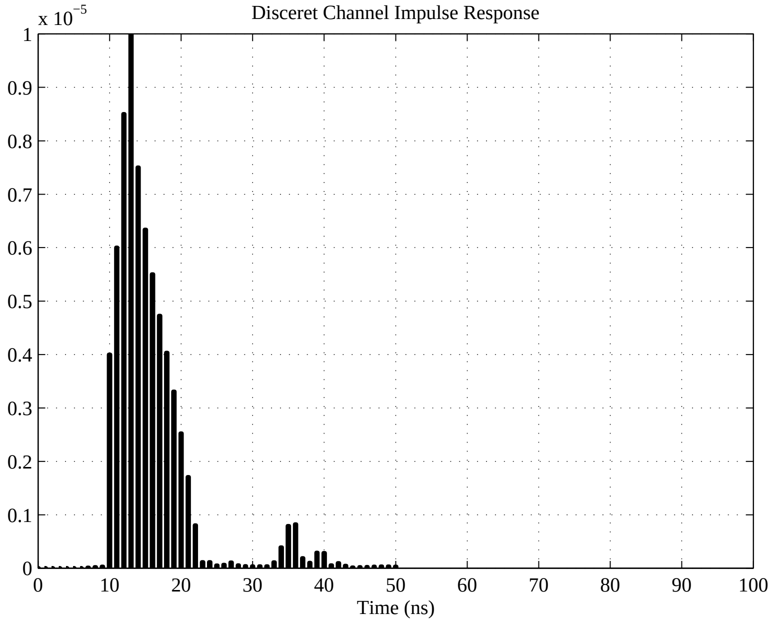

Figure 52: Channel impulse response for an empty room [22]

As observed from Fig. 52, the VLC channel is a multipath channel. Two multipath components are said to be "resolvable", if their delay difference significantly exceeds the inverse signal bandwidth [10,49]. In our simulations, the highest data rate in PHY I and PHY II types, is 96 Mb/s which corresponds to a symbol duration of 10.4 ns. The delay difference in the VLC channel under consideration is 30 ns, therefore for most cases we can safely assume that the multipath components are not resolvable and can be treated as a single channel tap leading to a frequency-flat channel. Therefore,

(37) can be written as

$$r\left[k\right]=s\left[k\right]h\left[k\right]+n\left[k\right],k=0,1,... \tag{42}$$

where the frequency-flat channel coefficient $h\left[k\right]$ is the DC component of the CIR obtained by performing fast Fourier transform (FFT) with sampling frequency of 2 Mb/s. For the indoor environment under consideration, $h\left[k\right]=1.35\times10^{-6}$. Similarly, for type PHY III, we obtain 3×3 channel coefficients which can be expressed as

$$H=\begin{bmatrix}0.1589 & 0.2464 & 0.1422\\ 0.3051 & 0.1163 & 0.2836\\ 0.1450 & 0.3612 & 0.1165\end{bmatrix} \tag{43}$$

4.4.1 Error Rate Performance

In this section, we present Monte Carlo simulation results for the performance of PHY I, PHY II and PHY III types.

PHY I

Figure 53 presents the bit error rate performance of PHY I.

- In Figure 54, BER of PHY I modes with OOK modulation and $f_{clk}=200$ kHz (modes a, b, c, d and e) are compared. At a targeted BER of 10^{-3}, SNR $=2.86$ dB is required for the uncoded system (mode PHY I.e). For a coded system with RS$(15,11)$ and 2/3-rate CC, the required SNR decreases to -0.3739 dB. Comparing the modes b and c, as the convolutional code rate increases, the required SNR for fulfilling the BER of 10^{-3} also increases.
- In Figure 55, BER of PHY I modes with VPPM modulation and $f_{clk}=400$ kHz (modes f, g, h and i) are compared. Comparing these modes, as the RS code rate increases, the required SNR for fulfilling the BER of 10^{-3} also increases. In other words, RS$(15,2)$ provides more performance improvement than RS$(15,4)$.
- It can also be concluded that as defined by the standard, VPPM is more robust than OOK.

PHY II

Figure 56 presents the bit error rate performance of PHY II. Unlike the PHY I which uses concatenation of RS and CC, this type deploys only RS coding.

- In Fig. 57, BER of PHY II modes with VPPM modulation and $f_{clk} = 3.75$ MHz (modes a and b) are compared. Comparing these modes, as the RS code rate increases, the required SNR for fulfilling the BER of 10^{-3} also increases. In other words, $RS(64, 32)$ provides more performance improvement than $RS(160, 128)$.
- In Fig. 58, BER of PHY II modes with VPPM modulation and $f_{clk} = 7.5$ MHz (modes c, d and e) are compared. At a targeted BER of 10^{-3}, SNR $= 3.25$ dB is required for the uncoded PHY II (mode PHY II.e), which is greater than the required SNR when using RS(64,32) in mode c (SNR $= -0.21$ dB) and RS(160,128) in mode d (SNR $=$ 0.96 dB).
- In Fig. 59, BER of PHY II modes with OOK modulation and $f_{clk} = 15$ MHz (modes f and g) are compared.
- In Fig. 60, BER of PHY II modes with OOK modulation and $f_{clk} = 30$ MHz (modes h and i) are compared.
- In Fig. 61, BER of PHY II modes with OOK modulation and $f_{clk} = 60$ MHz (modes j and k) are compared.
- In Fig. 62, BER of PHY II modes with OOK modulation and $f_{clk} = 120$ MHz (modes l, m and n) are compared.
- Similar to the previous case it can be generally stated that VPPM have been designed to operate in worst conditions.

PHY III

Figure 63 presents the bit error rate performance of PHY III.

- This type also deploys only RS coding. For example, with a RS$(64, 32)$ and 8-CSK modulation, an SNR of 32.81 dB is required to obtain BER $= 10^{-3}$.
- In Fig. 64, BER of PHY III modes with $f_{clk} = 12$ MHz (modes a and b) are compared. Comparing these modes, as the modulation size increases, the required SNR for fulfilling the BER of 10^{-3} also increases. In other words, 4-CSK provides more performance improvement than 8-CSK.
- In Fig. 65, BER of PHY III modes with $f_{clk} = 24$ MHz (modes c, d, e, f and g) are compared. At a targeted BER of 10^{-3}, SNR $= 42.38$ dB and SNR $= 43.79$ dB are required for the uncoded PHY III modes f and g, respectively, which are greater than required SNR values for coded system with same modulation (modes d and e, respectively). It is also concluded that, as the alphabet size of the modulation increases, performance decreases.
- In general, it can be observed that modes a and c with 4-CSK modulation are outperforming the modes b and d with 8-CSK modulation in terms of BER. Therefore, the cases with 4-CSK modulation have a better performance in terms of BER but there is a tradeoff between this BER and the data rate.

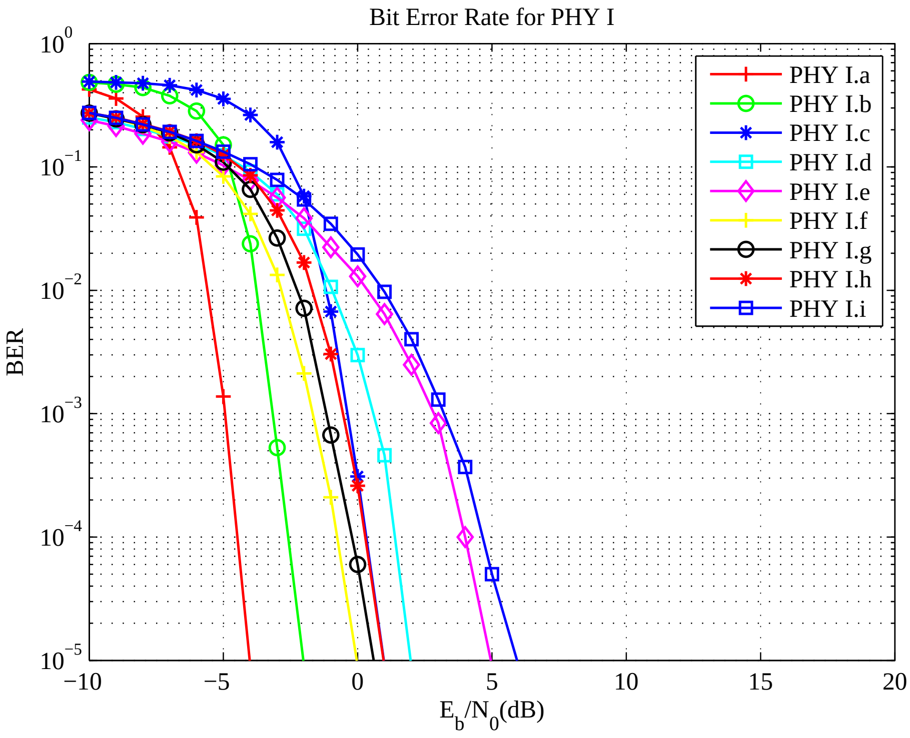

Figure 53: Bit error rate for PHY I

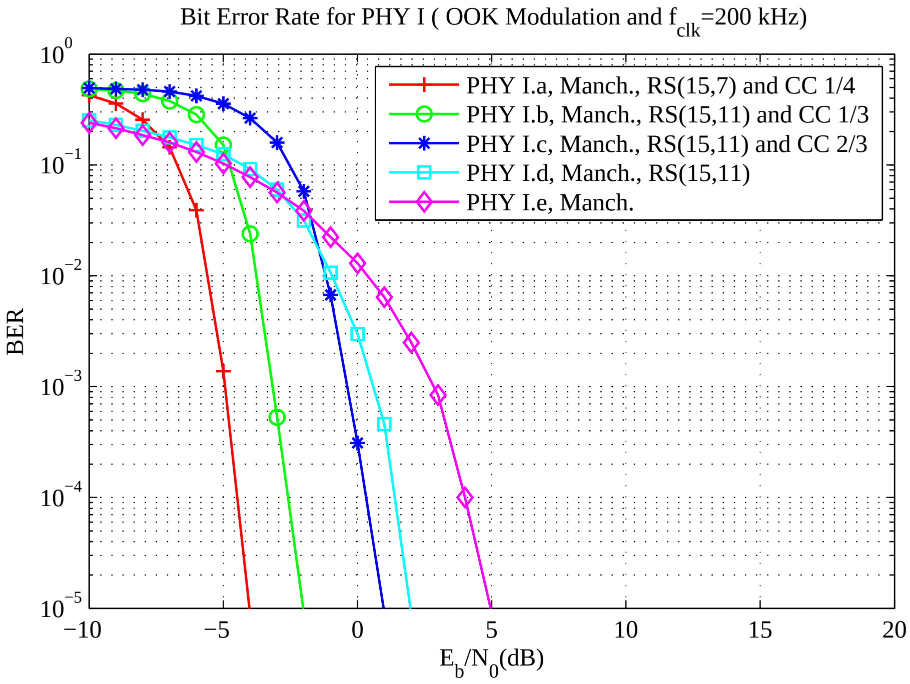

Figure 54: PHY I modes with OOK modulation and $f_{clk} = 200$ kHz

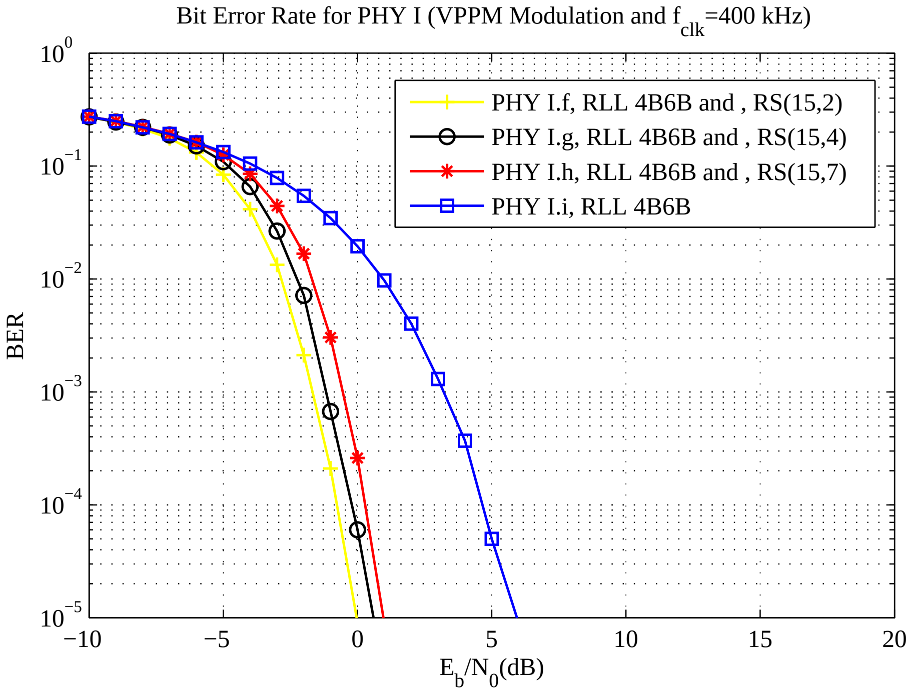

Figure 55: PHY I modes with OOK modulation and $f_{clk} = 400$ kHz

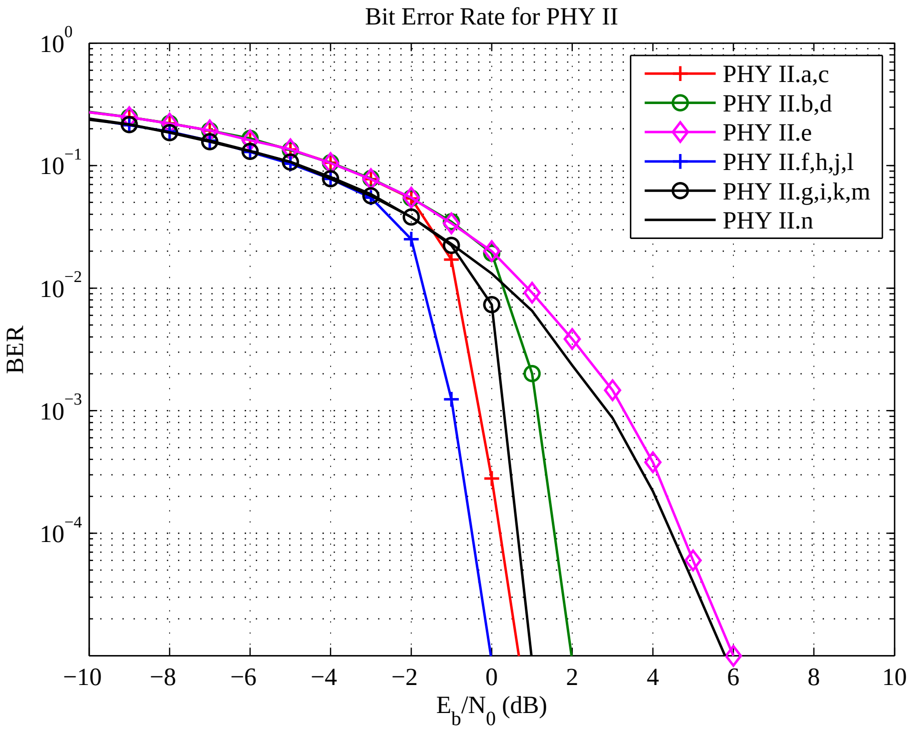

Figure 56: Bit error rate for PHY II

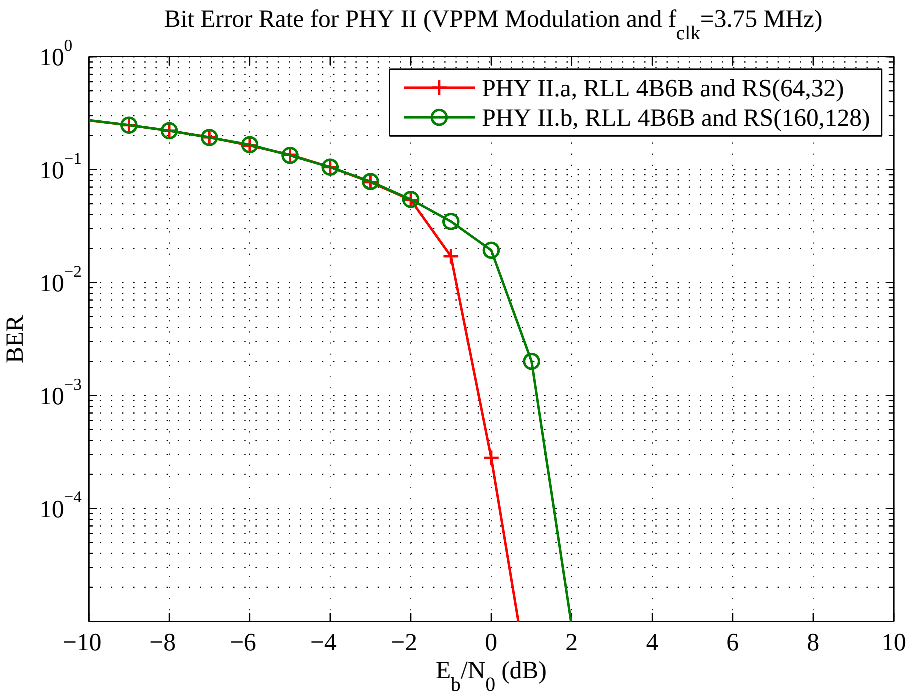

Figure 57: PHY II modes with VPPM modulation and $f_{clk} = 3.75$ MHz

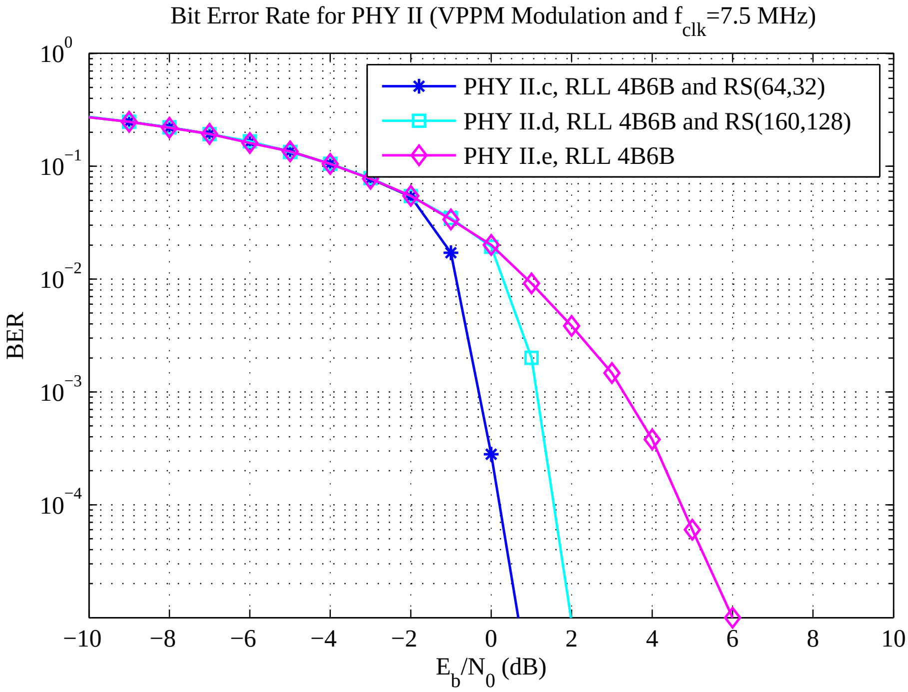

Figure 58: PHY II modes with VPPM modulation and $f_{clk} = 7.5$ MHz

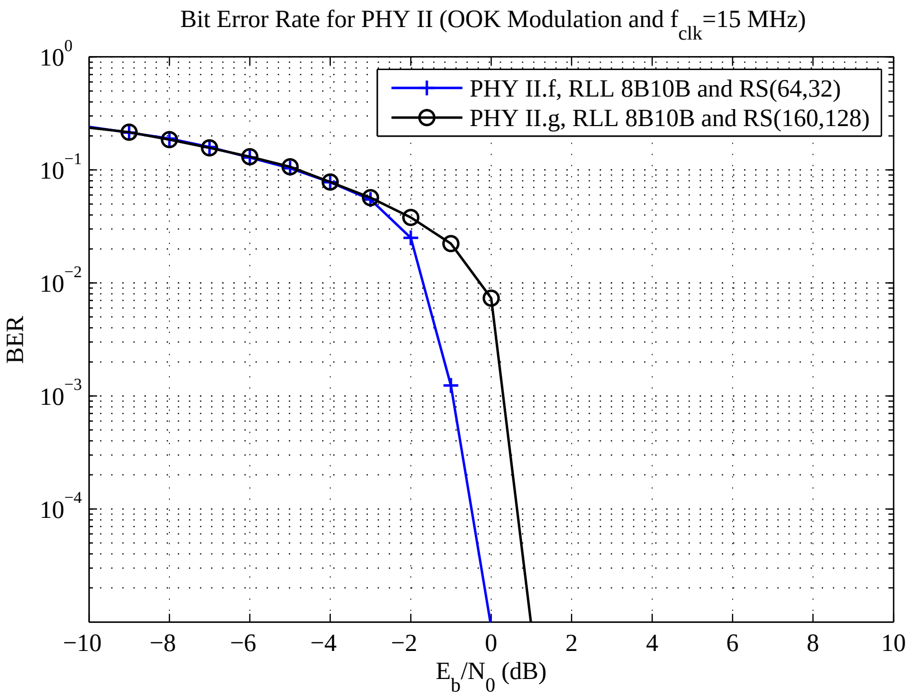

Figure 59: PHY II modes with OOK modulation and $f_{clk} = 15$ MHz

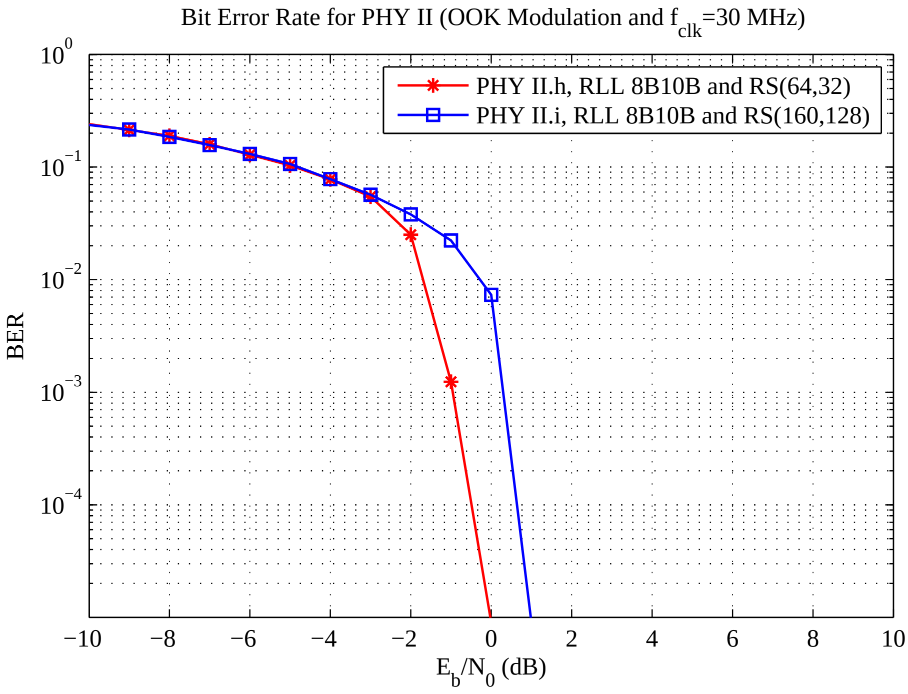

Figure 60: PHY II modes with OOK modulation and $f_{clk} = 30$ MHz

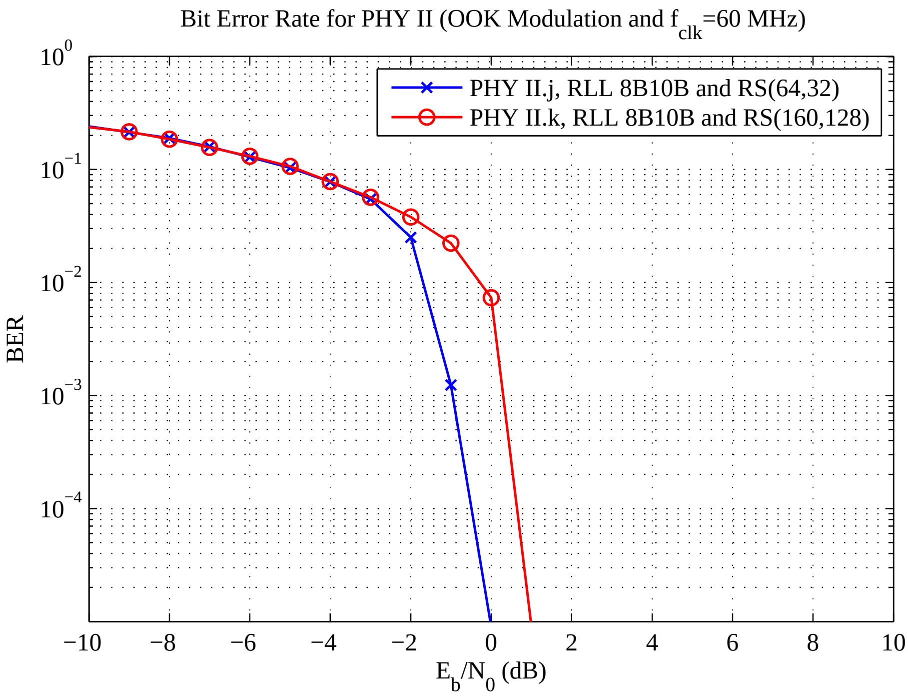

Figure 61: PHY II modes with OOK modulation and $f_{clk} = 60$ MHz

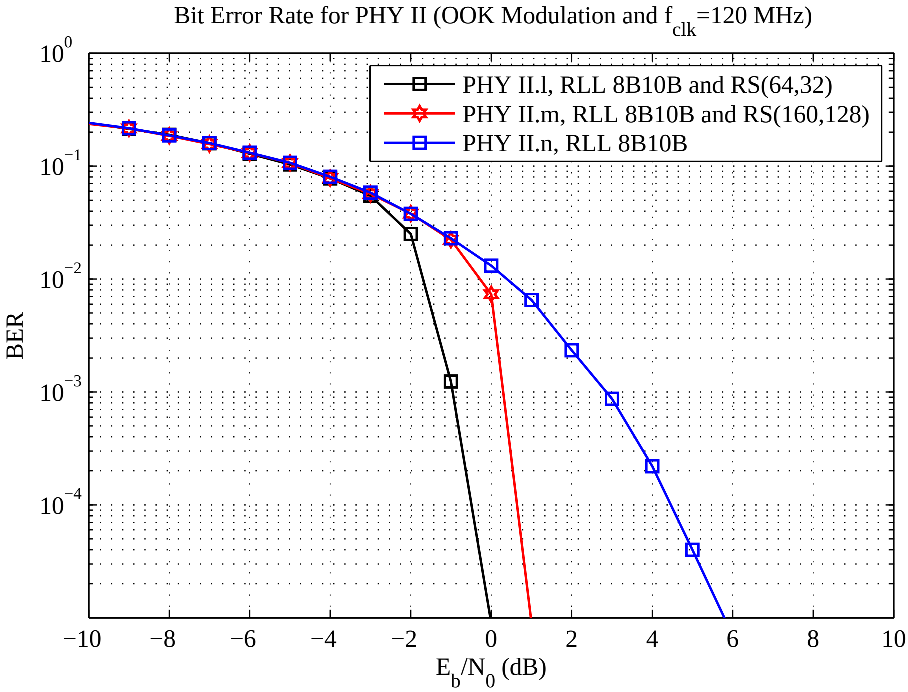

Figure 62: PHY II modes with OOK modulation and $f_{clk} = 120$ MHz

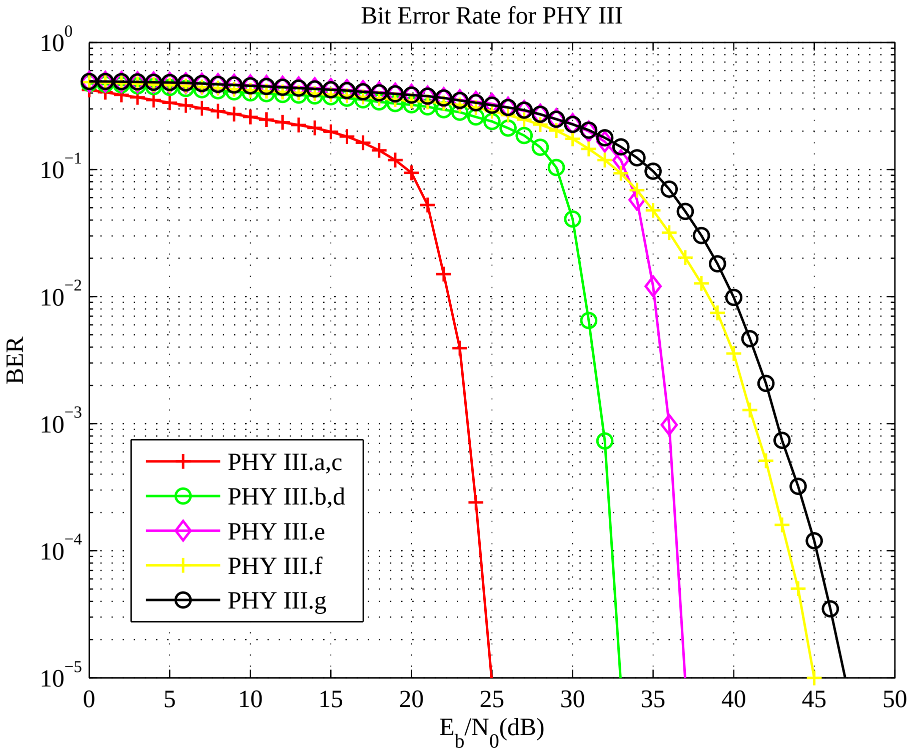

Figure 63: Bit error rate for PHY III

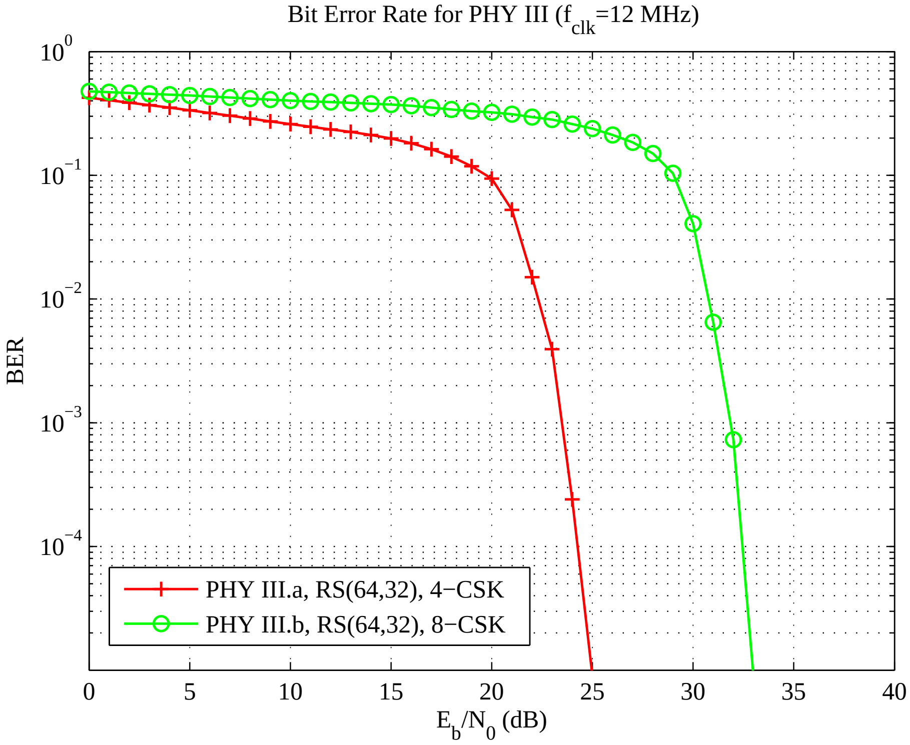

Figure 64: Bit error rate for PHY III ($f_{clk} = 12$ MHz)

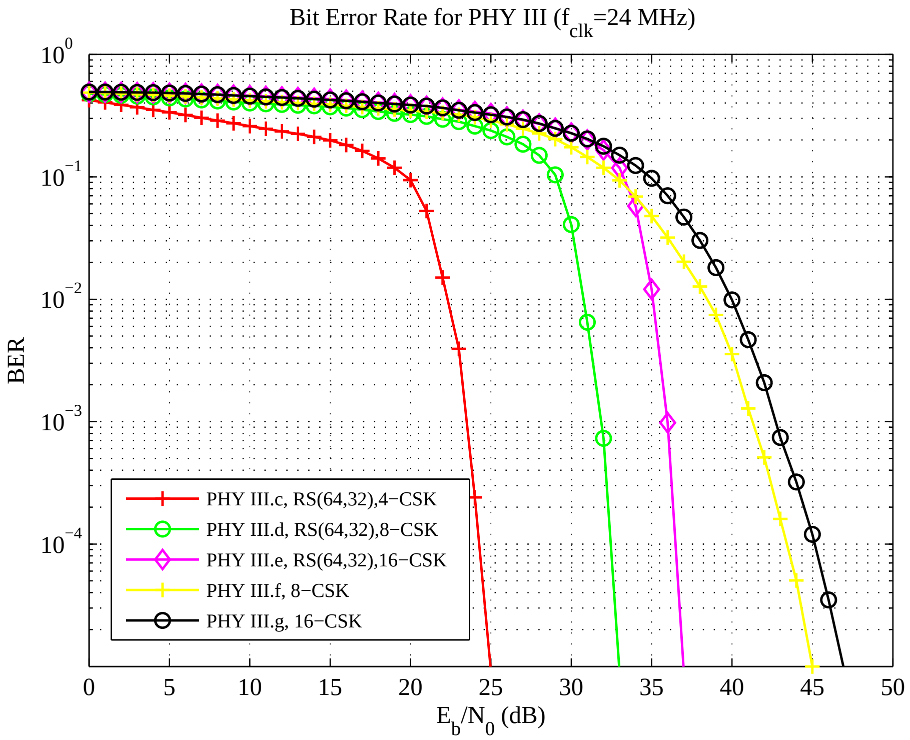

Figure 65: Bit error rate for PHY III ($f_{clk} = 24$ MHz)

CHAPTER V

CONCLUSIONS AND FUTURE WORK

This chapter summarizes the most relevant conclusions of this work. Important findings and simulation results are highlighted and some guidelines for future works that can be followed, are provided.

5.1 Conclusions

In this thesis, we carried out a VLC channel characterization study. Following the conventional approaches used in IR communications, we first proposed a modified ray-tracing method based on Barry's model to calculate CIR of a VLC channel. The CIR results based on this method are comprehensive, because the method is able to take into account the wavelength dependent nature of a VLC channel (e.g. power distribution of transmitters and spectral reflectance of materials) as well as environments with irregular shapes or even furnished rooms. However, it is difficult to implement this method in MATLAB, since it requires very high simulation times and/or the deployment of super computers, unless some assumptions are made which reduce the complexity of the scenario.

In an effort to improve the computational efficiency, we proposed another method which takes advantage of non-sequential ray-tracing capabilities of a commercial optical software named Zemax®. Although the main purpose of such software is optical and illumination system design, we smartly exploited the ray tracing features of this software which allows an accurate description of the interaction of rays emitted from the lighting source within a specified confined space (i.e., room, office etc). This method provides a considerable computational speed-up and enhances the accuracy of the results with its ability of calculating higher order reflections. Using this method, we obtained CIRs for a number of configurations involving different room sizes, number of LEDs, receiver/transmitter locations, wall materials and rooms with furniture.

We further quantified fundamental channel characteristics, specifically channel DC gain and RMS delay spread. In order to address statistical models for channel gain and RMS delay spread, we examined a large set of CIRs and analyzed the collected data. Different statistical distribution functions were tested and fitted to channel gains and delay spread histograms.

Finally, we developed a full-fledged simulation platform in MATLAB that implements all PHY types and modes of the IEEE Standard 802.15.7 for short range wireless optical communication using visible light. Using the developed simulation platform and channel models, we conducted a comprehensive performance evaluation of PHY layer of 802.15.7-based VLC systems and quantified bit error rate performance. Our results provide insight into different PHY types/modes and give guidelines on the suitability of each operation mode for the intended application based on the available SNR.

5.2 Future Work

VLC is a new emerging technology and has huge applications. The area needs to be explored to take full advantage of its unprecedented bandwidth and ubiquitous availability. There is still room for improvement in the channel modeling methods presented in this thesis and the mentioned results are only the first and primary observations.

The work in this thesis, encountered many challenges. Some of them are tackled and solved, some of them partially addressed and some of them are left for further investigation. The most important among them to be addressed in the future are:

- Studying the impulse response of the VLC channel bounce by bounce, to highlight the effects of higher-order reflections on the channel characteristics.

- Estimating the frequency response of VLC channels, including phase responses and delay responses.
- Obtaining a closed form expression for the CIR which can estimate the general behavior of the VLC channel.
- Analyzing a wide range of scenarios and collecting a large set of data, to propose specific distribution functions for statistical modeling of channel DC gain and RMS delay spread.

Bibliography

[1] T. Komine and M. Nakagawa, "Fundamental analysis for visible-light communication system using LED lights," *IEEE Transactions on Consumer Electronics*, vol. 50, no. 1, pp. 100–107, 2004.

[2] G. Ntogari, T. Kamalakis, J. Walewski, and T. Sphicopoulos, "Combining illumination dimming based on pulse-width modulation with visible light communications based on discrete multitone," *Journal of Optical Communications and Networking*, vol. 3, no. 1, pp. 56–65, 2011.

[3] S. Arnon, J. Barry, G. Karagiannidis, R. Schober, and M. Uysal, eds., *Advanced optical wireless communication systems.* Cambridge University Press, 1st ed., 2012.

[4] D. O'Brien and *et al.*, "Indoor visible light communications: challenges and prospects," *Proceedings of SPIE*, vol. 7091, 2008.

[5] M. Kavehrad, "Sustainable energy-efficient wireless applications using light," *IEEE Communications Magazine*, vol. 48, no. 12, pp. 66–73, 2010.

[6] J. K. Kim and E. F. Schubert, "Transcending the replacement paradigm of solid-state lighting," *Optics Express*, vol. 16, no. 26, pp. 21835–21842, 2008.

[7] K. Cui, *Physical Layer Characteristics and Techniques for Visible Light Communications.* PhD dissertation, University of California Riverside, CA, USA, 2012.

[8] M. Noshad and M. Brandt-Pearce, "Can visible light communications provide gb/s service?," *IEEE Communication Magazine*, 2013.

[9] Z. Ghassemlooy, W. Popoola, and S. Rajbhandari, *Optical wireless communications: system and channel modelling with MATLAB.* 1st ed., 2012.

[10] J. M. Kahn and J. R. Barry, "Wireless infrared communications," *Proceedings of the IEEE*, vol. 85, no. 2, pp. 265–298, 1997.

[11] R. Ramirez-Iniguez, S. M. Idrus, and Z. Sun, *Optical Wireless Communications: IR for Wireless Connectivity.* CRC Press, 2008.

[12] S. Hranilovic, *Wireless Optical Communication Systems.* Springer, 2005.

[13] K. Asadzadeh, *Efficient OFDM Signaling Schemes For Visible Light Communication Systems.* M.Sc. dissertation, Hamilton, Canada, 2011.

[14] F. R. Gfeller and U. Bapst, "Wireless in-house data communication via diffuse infrared radiation," *Proceedings of the IEEE*, vol. 67, no. 11, pp. 1474–1486, 1979.

[15] J. R. Barry and *et al.*, "Simulation of multipath impulse response for indoor wireless optical channels," *IEEE Journal on Selected Areas in Communications*, vol. 11, no. 3, pp. 367–379, 1993.

[16] R. Perez-Jimenez, J. Berges, and M. J. Betancor, "Statistical model for the impulse response on infrared indoor diffuse channels," *Electronics Letters*, vol. 33, no. 15, pp. 1298–1300, 1997.

[17] F. J. Lopez-Hernandez, R. Perez-Jimenez, and A. Santamaria, "Monte Carlo calculation of impulse response on diffuse IR wireless indoor channels," *Electronics Letters*, vol. 34, no. 12, pp. 1260–1262, 1998.

[18] F. Lopez-Hernandez, R. Perez-Jimenez, and A. Santamaria, "Modified Monte Carlo scheme for high-efficiency simulation of the impulse response on diffuse IR wireless indoor channels," *Electronics Letters*, vol. 34, no. 19, pp. 1819–1820, 1998.

[19] J. B. Carruthers and J. M. Kahn, "Modeling of nondirected wireless infrared channels," *IEEE Transactions on Communications*, vol. 45, no. 10, pp. 1260–1268, 1997.

[20] N. Hayasaka and T. Ito, "Channel modeling of nondirected wireless infrared indoor diffuse link," *Electronics and Communications in Japan (Part I: Communications)*, vol. 90, no. 6, pp. 9–19, 2007.

[21] S. Rodriguez and *et al.*, "Reflection model for calculation of the impulse response on IR-wireless indoor channels using ray-tracing algorithm," *Microwave and Optical Technology Letters*, vol. 32, no. 4, pp. 296–300, 2002.

[22] K. Lee, H. Park, and J. R. Barry, "Indoor channel characteristics for visible light communications," *IEEE Communications Letters*, vol. 15, no. 2, pp. 217–219, 2011.

[23] W. O. Popoola, E. Poves, and H. Haas, "Error performance of generalised space shift keying for indoor visible light communications," *IEEE Transactions on Communications*, vol. 61, no. 5, pp. 1968–1976, 2013.

[24] I. Stefan and H. Haas, "Analysis of optimal placement of LED arrays for visible light communication," in *IEEE 77th Vehicular Technology Conference (VTC Spring)*, pp. 1–5, IEEE, 2013.

[25] J. Armstrong, Y. A. Sekercioglu, and A. Neild, "Visible light positioning: a roadmap for international standardization," *IEEE Communications Magazine*, vol. 51, no. 12, pp. 68–73, 2013.

[26] L. Grobe and *et al.*, "High-speed visible light communication systems," *IEEE Communications Magazine*, vol. 51, no. 12, pp. 60–66, 2013.

[27] J. R. Barry, *Wireless Infrared Communications*, vol. 280. Kluwer Academic, 1994.

[28] F. Lopez-Hernandez and M. Betancor, "DUSTIN: algorithm for calculation of impulse response on IR wireless indoor channels," *Electronics Letters*, vol. 33, no. 21, pp. 1804–1806, 1997.

[29] K. Smitha, A. Sivabalan, and J. John, "Estimation of channel impulse response using modified ceiling bounce model in non-directed indoor optical wireless systems," *Wireless Personal Communications*, vol. 45, no. 1, pp. 1–10, 2008.

[30] J. B. Carruthers and P. Kannan, "Iterative site-based modeling for wireless infrared channels," *IEEE Transactions on Antennas and Propagation*, vol. 50, no. 5, pp. 759–765, 2002.

[31] Radiant Zemax LLC. [Online]. Available: `http://www.radiantzemax.com/zemax`.

[32] J. B. Carruthers, S. M. Carroll, and P. Kannan, "Propagation modelling for indoor optical wireless communications using fast multi-receiver channel estimation," in *IEEE Proceedings Optoelectronics*, vol. 150, pp. 473–481, 2003.

[33] S. Rodriguez and *et al.*, "Simulation of impulse response for indoor visible light communications using 3D CAD models," *EURASIP Journal on Wireless Communications and Networking*, vol. 2013, no. 1, pp. 1–10, 2013.

[34] CREE LEDs. [Online]. Available: `http://www.cree.com`.

[35] C. R. Lomba, R. T. Valadas, and A. d. O. Duarte, "Experimental characterisation and modelling of the reflection of infrared signals on indoor surfaces," in *Proceedings of IEEE Optoelectronics*, vol. 145, pp. 191–197, 1998.

[36] ASTER Spectral Library-Version 2.0. [Online]. Available: `http://speclib.jpl.nasa.gov`.

[37] GrabCAD Models. [Online]. Available: `https://grabcad.com`.

[38] J. B. Carruthers and S. Carroll, "Statistical impulse response models for indoor optical wireless channels," *International Journal of Communication Systems*, vol. 18, no. 3, pp. 267–284, 2005.

[39] B. M. Ayyub and R. H. McCuen, *Probability, statistics, and reliability for engineers and scientists.* CRC press, 3rd ed., 2011.

[40] E. Kreyszig, *Advanced Engineering Mathematics.* John Wiley & Sons, 10th ed., 2007.

[41] 802.15.7, "IEEE Standard for Local and Metropolitan Area Networks, Part 15.7: Short-Range Wireless Optical Communication Using Visible Light," Sep. 2011.

[42] S. Rajagopal, R. D. Roberts, and S. K. Lim, “IEEE 802.15.7 visible light communication: Modulation schemes and dimming support,” *IEEE Communications Magazine*, vol. 50, no. 3, pp. 72–82, Mar. 2012.

[43] R. D. Roberts, S. Rajagopal, and S. K. Lim, “IEEE 802.15. 7 physical layer summary,” in *IEEE Globecom Workshops (GC Wkshps)*, pp. 772–776, 2011.

[44] J. Baranda, P. Henarejos, and C. G. Gavrincea, “An sdr implementation of a visible light communication system based on the ieee 802.15. 7 standard,” in *IEEE 20th International Conference on Telecommunications (ICT)*, pp. 1–5, 2013.

[45] CIE, *Commission Internationale de l’Eclairage Proceedings, 1931.* Cambridge University Press, 1932.

[46] A. Widmer, *The ANSI Fibre Channel Transmission Code.* IBM: Newyork, USA, Rep. RC 18855, 1993.

[47] E. Monteiro and S. Hranilovic, “Constellation design for color-shift keying using interior point methods,” in *IEEE Globcom Workshops (GC Wkshps)*, pp. 1224–1228, IEEE, 2012.

[48] R. J. Drost and B. M. Sadler, “Constellation design for color-shift keying using billiards algorithms,” in *IEEE Globcom Workshops (GC Wkshps)*, pp. 980–984, Dec. 2010.

[49] H. Nguyen and *et. al*, “A MATLAB-based simulation program for indoor visible light communication system,” in *IEEE 7th International Symposium on Communication Systems Networks and Digital Signal Processing (CSNDSP)*, pp. 537–541, Jul. 2010.